KINETIC MODEL OF DNA REPLICATION AND THE LOOPING OF SEMIFLEXIBLE POLYMERS

by

Suckjoon JUN

BSc., Busan National University, Busan, Korea, 1997

MSc., Iowa State University, Ames, IA, USA, 1999

THESIS SUBMITTED IN PARTIAL FULFILLMENT

OF THE REQUIREMENTS FOR THE DEGREE OF

DOCTOR OF PHILOSOPHY

IN THE DEPARTMENT

OF

PHYSICS

SIMON FRASER UNIVERSITY

July 2004

APPROVAL

Name: **Suckjoon JUN**

Degree: **Doctor of Philosophy**

Title of Thesis: **Kinetic Model of DNA Replication and the Looping of Semiflexible Polymers**

Examining Committee:

Chair: **Dr. Barbara Frisken**
Professor of Physics

Dr. John Bechhoefer
Senior Supervisor
Professor of Physics

Dr. Dipankar Sen
Supervisor
Professor of Molecular Biology and Biochemistry

Dr. Michael Wortis
Supervisor
Professor Emeritus of Physics

Dr. Peter J. Unrau
Internal Examiner
Assistant Professor of
Molecular Biology and Biochemistry

Dr. Martin Zuckermann
Supervisor
Adjunct Professor of Physics

Dr. William M. Gelbart
External Examiner
Professor of Chemistry and Biochemistry
University of California, Los Angeles

Date Approved: July 15, 2004

SIMON FRASER UNIVERSITY

Partial Copyright Licence

Abstract

Biological systems are a rich source of new problems in physics, and solving them requires ideas from various fields. In this thesis, we focus on the specific biological phenomenon of DNA replication, which is tightly regulated by spatio-temporal "programs" during the cell cycle.

Inspired by a formal analogy between DNA replication and one-dimensional nucleation-and-growth processes, we extend the 1D Kolmogorov-Johnson-Mehl-Avrami (KJMA) model to arbitrary nucleation rates $I(t)$. We then use the KJMA model to extract kinetic parameters from data taken from molecular combing experiments. The analysis developed here can help biologists to understand and compare temporal programs of DNA replication of different organisms from a unified scheme.

After developing the kinetic model, we show how underlying physical properties of chromatin, in particular its intrinsic stiffness, can explain various long-standing experimental observations. These include synchrony and correlations in the initiation of replication origins, as well as determination of the origin spacings in the absence of sequence requirements in early embryos.

Γιά σένα

Acknowledgments

Before one hears his vocation, he is a man; IFF my soul has any decencies, it is the unconditional love from my parents, my little brother, and my late grandparents that I am indebted for. It always has been. And it always shall be.

I grew up in a culture where one's teachers are regarded as his extended parents. If I would be considered as a good and honest scientist one day, it must be that I was once a student of John Bechhoefer. Through him, I have started to learn how to read, write, speak, and think. Back in 2000, it must not have been easy for John to take me as his student, but I would choose him as a thesis advisor – my intellectual father – again.

I am fortunate to have had several other mentors and friends during my "vagabond" career in graduate school: I am deeply grateful to Aaron Bensimon for his constant encouragement and having faith in my research, who called me his friend despite the gap in our ages, experiences, and intellects. I also would like to thank John Herrick for helping me learn biology and also showing me there are different kinds of lives out there. And from Bae-Yeun Ha, I have learned not only the beauty of physics and physics itself, but also kindness and patience that any man should have. I owe these people more than words can say.

Coming from physics, learning biology was a series of surprises, frustrations, and joys. During this course of discovering "my ignorance, my desires, my willingness," interactions with the following biologists have been particularly and truly inspiring: Geneviève Almouzni, Benoit Arcangiolo, Ellen Fanning, Joel Huberman, and Philippe Pasero. Equally memorable, my meeting with Mark Goulian, Stan Leibler, and Peter Unrau made me realize why I do what I do.

Looking back, I realize it has been a great privilege to study biophysics at Simon Fraser. Just being surrounded by and interacting with the following professors made me feel I belong to a special group of people: John, Dave Boal, Barbara Frisken, Mike Plischke, Dipankar Sen, Jenifer Thewalt, Michael Wortis, and Martin Zuckermann; and (former) graduate students and post-docs: Bae-Yeun,

Michale Dugale, Martin Howard, Gerald Lim, Anirban Sain, Vahid Shahrezaei, and Dan Vernon.

In the last four years, in addition to my long-term collaborators Aaron, John, and Bae-Yeun, I have enjoyed collaborations and discussions with the following people: Ken Sekimoto on the KJMA model; Jeff Chen, Binny Cherayil, Arti Dua, Mohammed Kohandel, Christophe Koudella, Alexei Podtelezhnikov, Dipankar Sen, and Michael Wortis on loop formation of semiflexible polymers; Pu Chen, Yooseong Hong, Hideo Immamura, and Christophe Koudella on self-assembly of charged peptides; Tom Chou on various statistical mechanics and biophysics problems; Julian J. Blow, Bernie Dunker, Olivier Hyrien, Nick Rhind, and the biologists mentioned above on DNA replication. During this period, I have travelled many places and, particularly, would like to thank Ellen (Vanderbilt University, Nashville), Bae-Yeun and Pu (Univ. of Waterloo, Waterloo), and Bela Mulder (AMOLF, Amsterdam) for their hospitalities during my visit.

While working on this thesis, the following people have kindly helped me: Ron Berezney and Kishore Malyavantham with the replication foci image; Gary Felsenfeld and Mark Groudine with the illustration of higher-order structure of chromatin from their Nature article; Jeni Koumoutsakis and her mother with Greek.

I have always thought that I have very few friends. How wrong I was, because I have this many friends to thank for their invaluable friendships: my Korean connections – Yonghyun from my childhood, Kyungchor (we discussed from Hilbert to Wittgenstein), Yunhee, and the "mathmanias" Eunjin, Hyejoeng, Hyojin, Hyunjeong, Jina, Songhee, Woonjung, Youngsoon from university; the Iranian connections – Babak, Kamran, Simin, Vahid; people from the Bechhoefer lab – Bram-Marnie-Nadav, Haiyang, Phil, Yuekan, and visitors to our lab Mélanie, Peter, Russ, Sébastien; the "panini" connection – Bruna and Columba; the ladies in the physics department – Candida, Dagni, Helen, Sue; my special friend from the Boulder summer school Ginestra; my cinephile friends Chan and Stan; (thanks, Stan, for always being there when I am lost, and, Heather, I will remember our short walk in the "wheatfield" for a long time); friends from SFU – Cecilia, Gerald, Karl, Karn, Matt, Patricia, Philippe; from Waterloo – Andy, Hideo, Yooseong; from Iowa State University – Bassam, Dave, Julie; and the staffs at Early Music Vancouver and Pacific Cinémathèque.

I also would like to thank my former teachers, especially, Profs. Seyoung Jeong and Hyuk-Kyu Pak at Busan National University in Korea, and Marshall Luban and Constantin Stassis at Iowa State University in Ames, IA.

I cannot finish my acknowledgments without mentioning my experiences in Aaron's lab at Institut Pasteur and life in Paris back in 2001. My nostalgia for the people, the life, and even the stupid

mistakes I made in those six months is as strong as for my entire childhood: Aaron and his family for embracing me; Catherine, Chiara, Fabrice, Hélène and Nicolas, Katya, Reiner, and Sandrine for their friendships and help for my survival; Benoit, Bianca, John for countless number of beers and discussions from philosophy to films at Pouchla and other cafes.

And finally, I would like to acknowledge my infinite source of inspirations, J. S. Bach.

EPILOGUE: Knowing the influences on shaping my humble being by all these people, how could I not think of words of my hero François Jacob?

> *And then, how not to see that all these selves of my past life have played the greatest role, and the greater the earlier they came, in the development of the secret image that from the deepest part of me guides my tastes, desires, decision. Starting in the younger years, imagination seizes on the people and things it encounters. It grinds them down, transforms them, abstracts a feature or a sign with which to shape our ideal representation of the world. A schema that becomes our system of reference, our code to decipher oncoming reality. Thus, I carry within a kind of inner statue, a statue sculpted since childhood, that gives my life a continuity and is the most intimate part of me, the hardest kernel of my character. I have been shaping this statue all my life. I have been constantly retouching, polishing, refining it. Here, the chisel and the gouge are made of encounters and interactions; of discordant rhythms; of stray pages from one chapter that slip into another in the almanac of the emotions; terrors induced by what is all sweetness; a need for infinity erupting in bursts of music; a delight surging up at the sight of a stern gaze; an exaltation born from an association of words; all the sensations and constraints, marks left by some people and by others, by the reality of life and by the dream. Thus, I harbor not just one ideal person with whom I continually compare myself. I carry a whole train of moral figures, with utterly contradictory qualities, who in my imagination are always ready to act as my fellow players in situations and dialogues imprinted in my head since childhood or adolescence. For every role in this repertory of the possible, for all the activities that surround me and involve me directly, I thus hold actors ready to respond to cues in comedies and tragedies inscribed in me long ago. Not a gesture, not a word, but has been imposed by the statue within.*[1]

[1] François Jacob, *The Statue Within*, Basic Books, New York, 1988.

Contents

List of Tables

List of Figures

Chapter 1

Introduction

... then biology was bubbling with activity, changing its ways of thinking, discovering in microorganisms a new and simple material, and drawing closer to physics and chemistry. A rare moment....

François Jacob, *Nobel Lecture*, December 11, 1965

1.1 Physics and biology united[1]: a brief overview

Can physics deliver another biological revolution? This provocative question was the title of the editorial in the January 14, 1999, issue of the journal *Nature* [1]. When we read the history of science, we learn that many major advances happened only when the field was ready – a state usually preceded by technological developments and followed by a "paradigm shift" [2]. In that respect, one may consider the empirical data that is being obtained at an ever-increasing rate in recent years as a prelude to another revolution in biology. But why should people who are trained in physical sciences be excited by what is happening in biology?

In fact, there have always been physicists who have crossed the boundaries: In the early 20th century, Max Delbrück proposed a model for the molecular origin of mutations [3], which was popularized in the classic book *What is Life?* by another distinguished physicist, Erwin Schrödinger [4]. (Although many of the detailed ideas in the book proved to be wrong, it inspired a generation of biologists.) As another example, half of the credit for the discovery of the famous double-helix structure

[1]The original title was *Physics and biology united (...!)*. For those who are curious about "...," it was inspired by the Chilean song *¡El Pueblo Unido Jamás Será Vencido!*

of *deoxyribonucleic acid* (DNA) is shared by the physicist Francis Crick [5]. And, Walter Gilbert, a particle physicist by training, received a Nobel prize for contributions to DNA sequencing [6].

On the other hand, some physicists have seen biological systems as a rich source of new problems in physics. The energy landscape theory of biomolecules and protein folding [7], membrane mechanics [8], neural networks [9], and electrostatics problems inspired by DNA [10] are just a small sample from a long list of examples in the last few decades.

The recent interdisciplinary work by scientists in physics, biology, computer science, and other areas has a different nature from that of the "old schools" mentioned above. In particular, systems biology, or "modular biology"[2] as it is sometimes called, is a field where one needs not only to manage data but also new ways of thinking about the data. Here, data and experiments are the keywords that distinguish the current research activities and their outcomes from the pioneering but less-successful attempts several decades ago.

Indeed, starting in the 1960s, Michael Savageau and co-workers built a powerful framework (which became known as Biochemical Systems Theory, or BST) for a general analysis of interacting biochemical processes [12–14]. However, it was only much later, at the end of the 1990s, that scientists were finally able to tackle important questions in systems biology, using the powerful methods of genetic engineering and other techniques that had begun to produce large amounts of data [15–19]. Without such data, the theoretical work of Savageau and others was "premature" and destined to have little influence.[3]

To make an analogy, the current situation in biology resembles the exciting events that occurred about four centuries ago in physics, when, by collecting significantly better data, Brahe led Kepler to conclude that planetary orbits were ellipses and not circles (with or without epicycles) [21]. Kepler's elliptical model said nothing about the physical origins of ellipses, but his kinematic modeling was an essential starting point for Newton's work on dynamics 50 years later [22].

Although our goals here are much more modest, the theme of this thesis – DNA replication – certainly has similar ingredients: The recent development of "molecular combing" [23] and other techniques [24, 25] now makes it possible to extract large amounts of data from the replication process and, thus, to have detailed and reliable statistics. In other words, in light of systems biology,

[2]"Cell biology is in transition from a science that was preoccupied with assigning functions to individual protein or genes, to one that is now trying to cope with the complex sets of molecules that interact to form functional modules." [11]

[3]There is a well-documented literature about "premature" scientific ideas that were neglected because it was not clear how to connect the new ideas to empirical data. See, for example, Ref. [20].

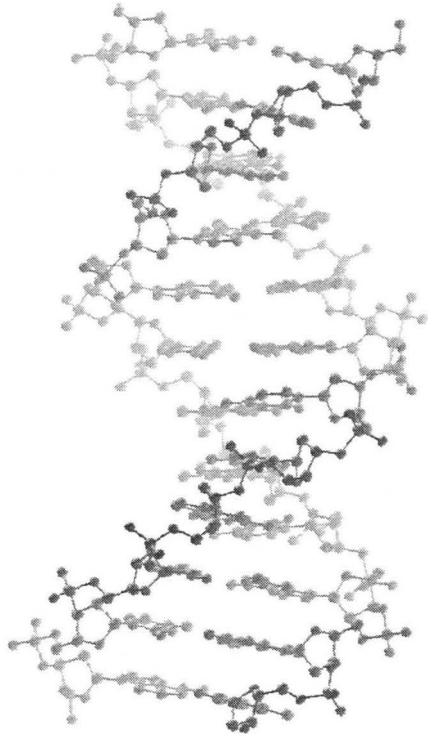

Figure 1.1: Double-helix structure of DNA (B-form). Rendered using VMD (Visual Molecular Dynamics) [26].

the field of DNA replication is becoming mature and ready for quantitative modeling – a modeling that makes experimentally testable predictions, thus helping researchers to understand their data at a deeper level.

In this thesis, we shall show that recent experiments on DNA replication in *Xenopus* early embryos can be modeled via a kinetic description that plays the same role as Kepler's description of elliptical orbits. This model then suggests a particular biological mechanism of relevance to DNA replication, where physical properties of chromatin loops naturally explain several seemingly unrelated kinetic parameters. Perhaps more importantly, we are now able to predict how changes in certain physical parameters (in this case, the intrinsic stiffness or persistence length of chromatin) will affect the kinetics of DNA replication.

1.2 Getting started: a brief history of DNA replication

At the end of their historic 1953 paper on the double-helix structure of DNA (Fig. 1.1), Watson and Crick noted, "It has not escaped our notice that the specific pairing we have postulated immediately

suggests a possible copying mechanism for the genetic material." [5]

A month later, in their second paper, Watson and Crick published their hypothesis for the replication of DNA: "semiconservative replication" [27]. Their basic idea was that, if the order of the bases on one of the pairs of chains is given, then the exact order of the bases on the other one is determined by a specific pairing of complementary bases [adenosine (A) with thymine (T), cystine (C) with guanine (G)]. One can then think of the double-stranded DNA molecule as a pair of templates for replication, each of which is complementary to the other. In other words, each single strand acts as a template for the formation of a complementary DNA strand, so that each daughter DNA molecule has the same sequence as the original one. Semiconservative replication was confirmed in 1958 by an elegant experiment by Meselson and Stahl [28].

How does a cell actually replicate DNA? If Watson and Crick were right, there should be an enzyme that makes DNA copies from a DNA template. In 1956, Arthur Kornberg and colleagues demonstrated the existence of such an enzyme: DNA polymerase I (pol I) of *E. coli* bacteria, a model prokaryote [29]. Indeed, the current paradigm of DNA replication traces back to Kornberg's pioneering discovery and his method of enzymology (see below, as well as Ref. [30]).

Schematically, to be able to replicate, a cell has to unfold and unwind its DNA. (As we shall explain shortly, DNA is packed into a compact structure called chromatin.) It also has to separate the two strands from each other. The cell has a complex machinery to perform these tasks [Fig. 1.2(a)]. When it is time to replicate, special initiator proteins attach to the DNA at regions called replication origins. The initiator proteins pry the two strands apart, and a small gap is created at the replication origin. Once the strands are separated, another group of proteins that carries out the DNA replication attaches and goes to work.

This group of proteins includes helicase, which serves as an "unzipper" by breaking the bonds between the two DNA strands. This unzipping takes place in both directions from the replication origins, creating a replication bubble (or "eye").[4] The replication is therefore said to be bidirectional. Once the two strands are separated, a small piece of RNA, called an RNA primer, is attached to the DNA by an enzyme called DNA primase. These primers are the beginnings of all new DNA chains, since DNA polymerases cannot start from scratch. It is a self-correcting enzyme and copies the DNA template with remarkable fidelity.[5]

[4]The terms "replication bubble" or "eye" come from the appearance of DNA in early electron-microscopy work. (See Fig. 1.5, below.)

[5]As an example of this fidelity, consider a naive estimate for the base-pairing error rate that uses the free-energy

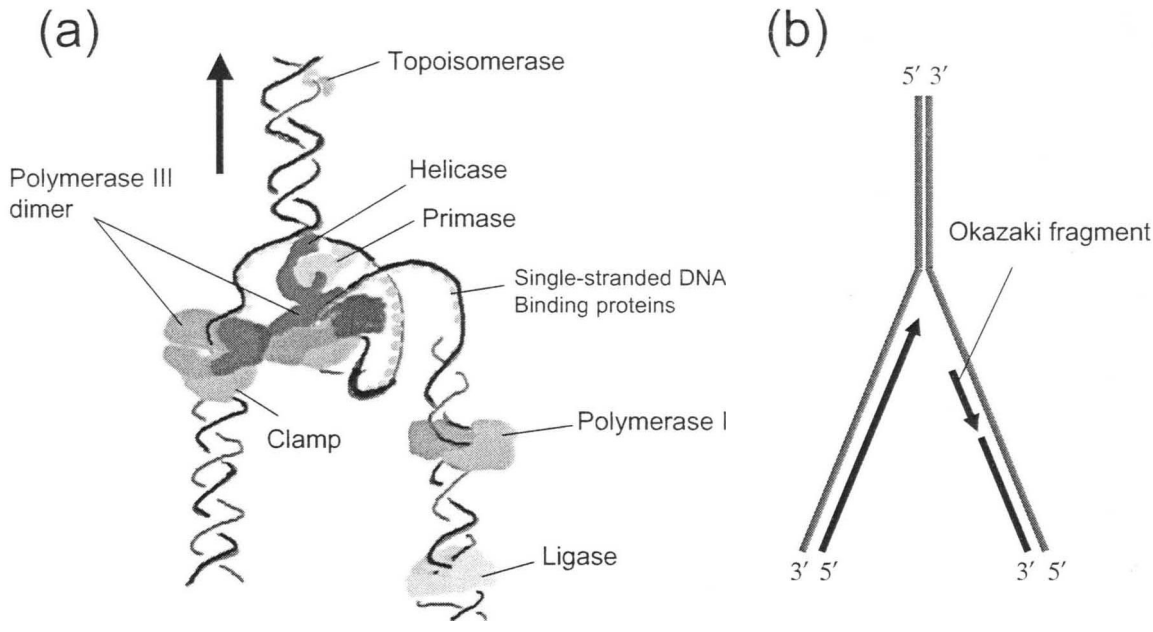

Figure 1.2: Schematic model of replication fork. (a) Various enzymes and proteins that function at or near a DNA replication fork (see text for details). The fork is moving upward. (b) Okazaki fragment.

The DNA polymerase can read in only one direction (3′ to 5′). This gives rise to some trouble, since the two strands of the DNA are antiparallel. On the upper strand, which runs from 3′ to 5′, nucleotide polymerisation can take place continuously without any problems. This strand is called the "leading" strand. But how does the polymerase copy the other strand then when it runs in the opposite direction, from 5′ to 3′? On this "lagging" strand the polymerase produces short DNA fragments, called Okazaki fragments, by using a backstitching technique [Fig. 1.2(b)]. These lagging strand fragments are primed by short RNA primers and are subsequently erased by pol I and replaced by DNA with help of DNA ligase (Fig. 1.2). Meanwhile, as the fork progresses, DNA becomes more and more twisted because of its double-helix structure, and it is topoisomerase that "untwists" DNA.

As one can imagine, DNA replication is crucial to life and, thus, highly regulated, both tem-

difference between correct and incorrect base pairs. Since incorrect base pairs have an enthalpy (bonding + stacking) several $\sim k_BT$ greater than the correct base pairs [31], one can use the Boltzmann distribution to estimate an error rate of $\exp(\Delta E/k_BT) \sim 10^{-2} - 10^{-4}$. In fact, the observed error rate is 10^{-10} and is the result of an elaborate active "proofreading" and correction scheme [32].

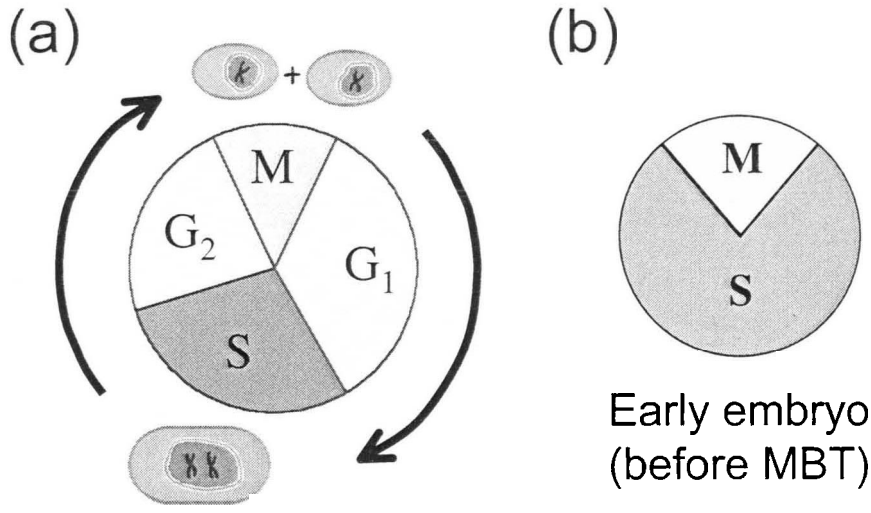

Figure 1.3: Eukaryotic cell cycle. (a) The two critical events of the cell cycle are S and M, which are DNA replication (synthesis) and mitosis (nuclear and cell division), respectively. There are also gap phases between the two. Normally, replication origins are replications are determined ("licensed") in G_1 before the cell enters S phase. G_1, S, and G_2 are collectively referred to as "interphase." (b) An embryonic cell cycle lacks the Gap phases.

porally and spatially. But, when and where does initiation actually occur? How many replications origins are there along the genome?

The answers to many of these questions are well-understood for prokaryotes, which usually have circular DNA and a single unique origin [30]. For example, *E. coli* has a specific site called oriC (245 bp long) where a complex of DnaA proteins bind and starts replication. The replication bubble then grows bidirectionally (at a rate $\approx$ 1000 bp/sec) and terminates at another site called terC. The whole 4.7 million basepairs (bp) are completely duplicated in less than 40 minutes. What about eukaryotes? The answer is similar but much more complex. First, eukaryotic cells go through a series of stages, called a cell cycle [Fig. 1.3(a)], and DNA is only replicated during one of those stages called S phase (not surprisingly, "S" stands for synthesis) [Fig. 1.3(a)]. Second, eukaryotic genomes are usually much longer than prokaryotic ones. The human genome, for example, consists of 23 (pairs of) chromosomes with a total length of 3×10^9 bp. Here, "chromosomes" refers to the threadlike "packages" of genes in the cell nucleus (Fig. 1.4). In contrast to prokaryotic systems, the replication fork velocities are of order 10 bp/sec. Because the S phase can be as short as 20 minutes, replication must take place simultaneously at many different sites along the DNA. Indeed, with fork

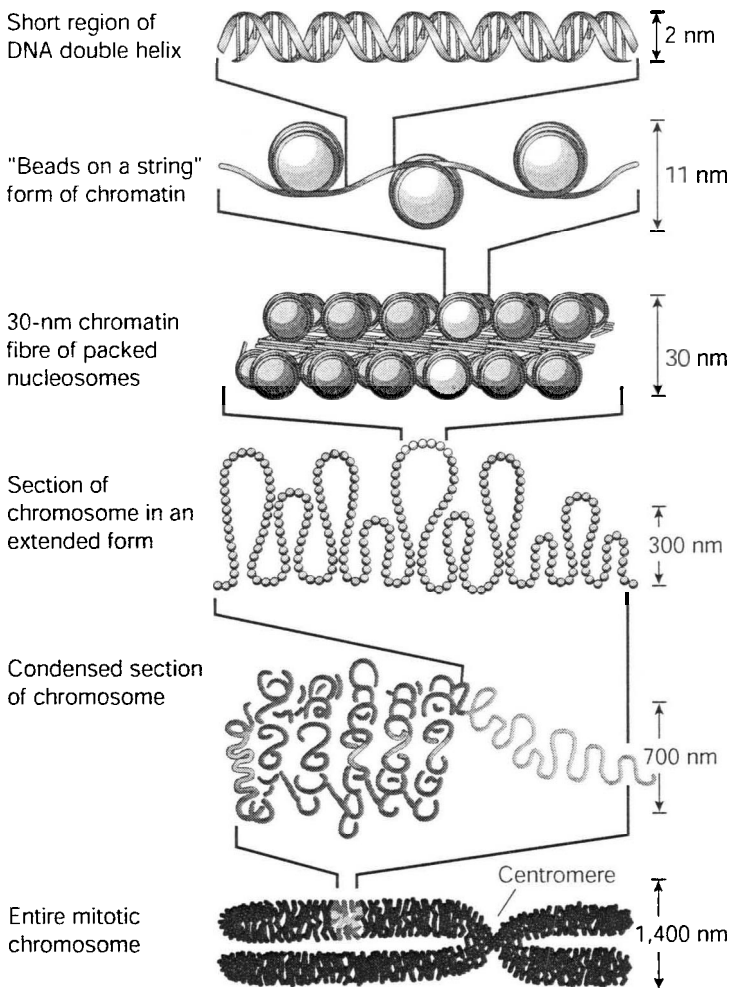

Figure 1.4: Higher-order structure of chromatin. Courtesy of Gary Felsenfeld and Mark Groudine. Reprinted by permission from Nature [vol. **421**, pp. 448-453] copyright (2003) Macmillan Publishers Ltd.

velocities 100 times slower and with 1000 times the DNA to replicate, the eukaryotic genome can have as many as 10^5 origins of replication (Fig. 1.5), often with different growth rates.

Because of these complexities, there are still many basic questions waiting to be answered. For example, what regulates the spatio-temporal distributions of replication bubbles during the course of S phase? What ensures that DNA is replicated once and only once during S phase? Are there specific sequences of DNA that are responsible for initiation in eukaryotes? Does a higher-order structure of chromatin and/or other structures inside the cell nucleus play a role in DNA replication?

As a more specific example, we briefly summarize the process of DNA replication in one of the best-studied eukaryotic systems, the famous South African clawed toad *Xenopus laevis*. (For detailed reviews, see Refs. [34, 35].)

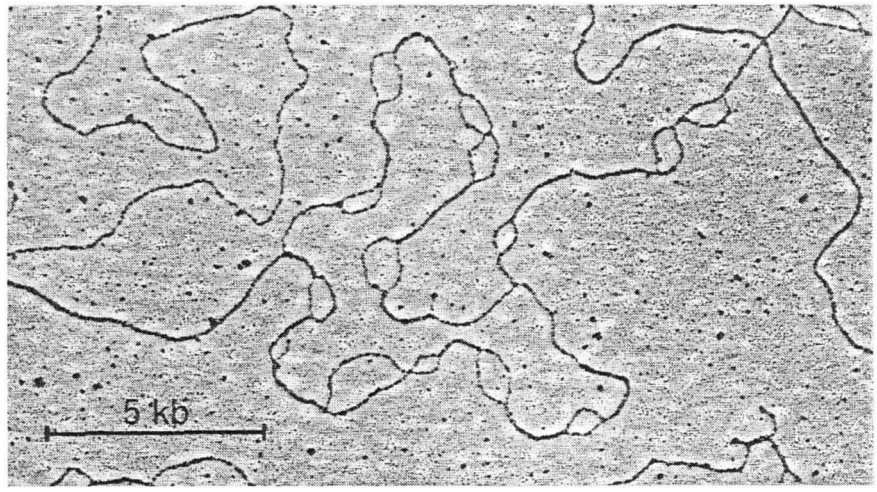

Figure 1.5: Electron micrograph showing multiple replication bubbles of *Drosophila melanogaster* DNA. From Fig. 2 in Ref. [33] by Kriegstein and Hogness, with permission. Copyright© *Proceedings of the National Academy of Sciences USA.*

The fertilized *Xenopus* egg undergoes 12 synchronous rounds of cell division in about 8 hours. During this period, the large egg ($\approx$ 1 mm) subdivides into 4096 ($= 2^{12}$) smaller cells without growing in size. After the first 12 cycles of cleavage, the cell-division rate slows down abruptly, and transcription (protein synthesis) of the embryo's genome begins. This change is known as the mid-blastula transition (MBT). Since its large eggs are easy to manipulate and see and since its cell cycle is rapid and simple,[6] the early-embryo *Xenopus* is a good model for studying cell-cycle regulation.

An interesting (and important) fact about *Xenopus* early embryos is that, unlike *E. coli* or another simple eukaryote, budding yeast, there is no specific sequence requirement for initiating DNA replication [36]. Moreover, these early embryos lack an efficient S/M checkpoint that makes cells delay entry into mitosis in the presence of unreplicated DNA [37]. Nevertheless, the *Xenopus* diploid genome (> 6 billion basepairs!) is completely replicated within the 10-20 minutes of S phase. Apparently, there is a strict control mechanism, independent of sequence, that regulates the density of origins and time of activation to prevent the "random-completion problem," where any large fluctuations in the spacing between origins would lead to (fatal) fluctuations in the duration of S phase. One of the goals of this thesis is to study the spatio-temporal program of DNA replication in this

[6]Each cycle consists of only two stages: Mitosis (cell-division) and S phase; see Fig. 1.3(b). Also, note that during S phase in early embryos, no proteins are synthesized [32].

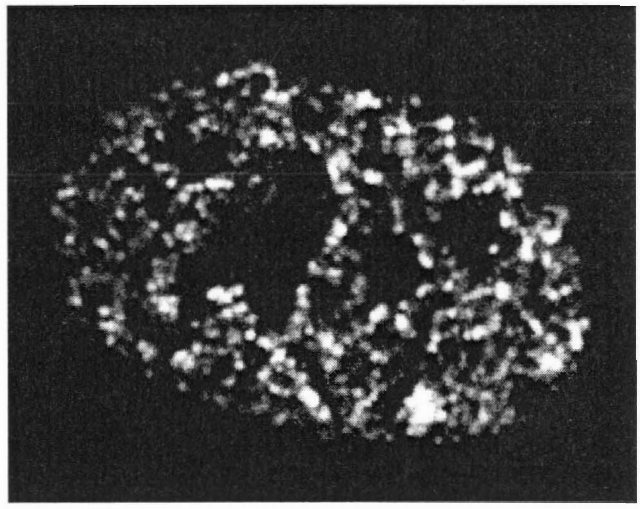

(a) Replication foci

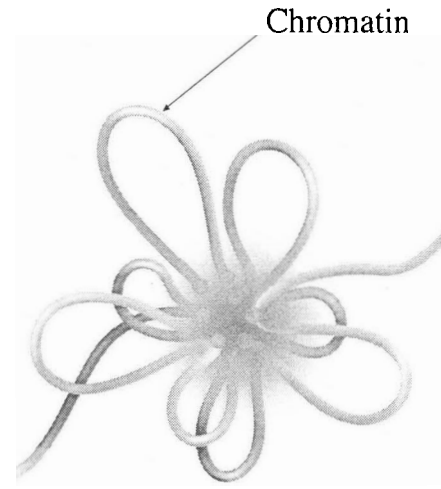

(b) Chromatin loops

Figure 1.6: Replication foci and chromatin loops. (a) An image of early S-phase-labeled (BrdU) replication sites of HeLa cell nucleus (taken with an Olympus epifluorescent microscope). The diameter of the nucleus in this image is approximately $10\mu m$. 20 μ molar BrdU was incorporated for 7 minutes for pulse labeling. Courtesy of Ronald Berezney and Kishore Malyavantham (State University of New York at Buffalo). (b) Chromatin loops at focus ("replication factory").

system.

Finally, many textbook models (e.g., Fig. 1.2) for replication often display polymerases that track like locomotives along their DNA templates. However, this idea stems not from any solid experimental evidence but from a perception of relative size and from somewhat misleading early electron micrographs (such as Fig. 1.5). Although one's intuition is that the smallest object should move, recent evidence supports an alternate model in which DNA polymerases are immobilized by attachment to a larger structure, where they reel in their *looped* templates and extrude newly made nucleic acids [38]. These polymerases do not act independently; they are concentrated in discrete "factories," where they work together on many different templates. Indeed, although the resolution is limited, pictures of stable replication foci (where nascent DNA is concentrated), such as shown in Fig. 1.6(a), strongly support the factory model. In the latter part of this thesis, we will explore how the distribution of replication bubbles (Fig. 1.5) can be regulated by chromatin loops at replication factories.

1.3 About this thesis

The main goal of this thesis is to develop and present various tools in theoretical physics that can be used to identity the spatio-temporal program of DNA replication from data. We then apply our methods to recent experiments on a model system, *Xenopus* egg extracts, which support all the nuclear events of the early embryonic cell-division cycle.

Our starting point is the electron micrograph of multiple eyes in Fig. 1.5, which we interpret as a "snapshot" of a one-dimensional system undergoing nucleation-and-growth processes with an unknown nucleation rate $I(t)$. This mapping of the description of DNA replication onto the description of (one-dimensional) crystal-growth kinetics gives us access to a well-developed set of theories.[7] Thus, in Ch. 2, we introduce the classic Kolmogorov-Johnson-Mehl-Avrami model of nucleation and growth [39–43] and extend it to the case of an arbitrary nucleation function $I(t)$. In Ch. 3, we study the reverse, i.e., we discuss how to extract $I(t)$ from a set of many snapshots analogous to Fig. 1.5. In Ch. 4, we apply the kinetic model to data recently obtained by Herrick *et al.* [44]. We then discuss the extracted $I(t)$ as a temporal program of replication in *Xenopus* early embryos.

In the next two chapters, we shift our focus to understanding the biological mechanisms that underlie the replication program. This leads us to consider the replication-factory model. (Fig. 1.6) Since one of the possible implications of the factory model is that chromatin fibers should attach to immobilized factories via looping, the loop sizes should correspond to the origin spacings. As we shall show later, the loop-formation probability depends on the intrinsic stiffness (or "persistence length") of polymers, and there is a specific length where loops can form most efficiently. In Ch. 5, we incorporate these results into the kinetic model to explain the spatial distribution of replication bubbles in the experimental data. Two crucial assumptions here are that, first, the loop-formation time is much shorter than the typical time-scale of DNA replication such as the duration of S phase. Second, we assume that the sizes of loops formed represent those with largest statistical weight, as calculated via an equilibrium distribution of loop-sizes. In Ch. 6, we tackle a simplified version of the problem, namely, loop-formation dynamics of a single chain with two "sticky" ends. We obtain a simple analytical expression to estimate the closing time τ_c, and, indeed, a typical τ_c for chromatin is

[7] We emphasize that one should not interpret Fig. 1.5 as the actual geometry of DNA in a cell nucleus during replication. Even so, the one-dimensional topology of alternating replicated and non-replicated domains is still correct, and our model will be based on this topology.

several orders of magnitude smaller than the duration of S phase. In addition, in certain (biologically relevant) limits, the loop-formation rate of polymers is set by the equilibrium distributions of loop sizes, thus justifying the results in Ch. 5.

The results in Ch. 4 and 5 can be considered to provide a mechanism that ensures complete, faithful, and timely reproduction of the genome without any sequence dependence of replication origins in *Xenopus* early embryos.

Parts of this thesis are based on previously published our work: Ch. 4 on Ref. [59], Ch. 5 on Ref. [71], and Ch. 6 on Ref. [155].

Chapter 2

The Generalized Kolmogorov-Johnson-Mehl-Avrami Model

2.1 Introduction

Consider a tray of water that at time $t = 0$ is put into a freezer. A short while later, the water is all frozen. One may thus ask, "What fraction $f(t)$ of water is frozen at time $t \geq 0$?" In the 1930s, several scientists independently derived a stochastic model that could predict the form of $f(t)$, which experimentally is a sigmoidal curve. The "Kolmogorov-Johnson-Mehl-Avrami" (KJMA) model [39–43] has since been widely used by metallurgists and other materials scientists to analyze phase transition kinetics [45]. In addition, the model has been applied to a wide range of other problems, from crystallization kinetics of lipids [46], polymers [47], the analysis of depositions in surface science [48], to ecological systems [49], and even to cosmology [50]. For further examples, applications, and the history of the theory, see the reviews by Evans [51], Fanfoni and Tomellini [48], and Ramos *et al.* [52].

In the KJMA model, freezing kinetics result from three simultaneous processes: 1) nucleation of solid domains ("islands"); 2) growth of existing islands; and 3) coalescence, which occurs when two expanding islands merge. In the simplest form of KJMA, islands nucleate anywhere in the liquid areas ("holes"), with equal probability for all spatial locations ("homogeneous nucleation"). Once

an island has been nucleated, it grows out as a sphere at constant velocity v. (The assumption of constant v is usually a good one as long as temperature is held constant, but real shapes are far from spherical. In water, for example, the islands are snowflakes; in general, the shape is a mixture of dendritic and faceted forms. The effect of island shape – not relevant to the one-dimensional version of KJMA studied here – is discussed extensively in [45].) When two islands impinge, growth ceases at the point of contact, while continuing elsewhere. KJMA used elementary methods, reviewed below, to calculate quantities such as the solid fraction $f(t)$. Later researchers have revisited and refined KJMA's methods to take into account various effects, such as finite system size and inhomogeneities in growth and nucleation rates [53–55].

Although most of the applications of the KJMA model have been to the study of phase transformations in three-dimensional systems, similar ideas have been applied to a wide range of one-dimensional problems, such as Rényi's car-parking problem [56] and the coarsening of long parallel droplets [57]. In this thesis, we shall apply the KJMA model to DNA replication in higher organisms. We start by observing that the duplication of eukaryotic genomes shares a number of common features [58] that can be mapped onto the basic assumptions of the KJMA model [59]:

1. DNA replication starts at a large number of sites known as "origins of replication." The DNA domain replicated from each origin is referred to, informally, as an "eye" or a "replication bubble" because of its appearance in electron microscopy. (Fig. 1.5.)

2. The position of each potential origin that is "competent" to initiate DNA replication is determined before the beginning of the synthesis part of the cell cycle ("S phase"), when several proteins including the origin recognition complex (ORC) bind to DNA, forming a pre-replication complex (pre-RC).

3. During S phase, a particular potential origin may or may not be activated. Each origin is activated not more than once during the cell-division cycle.

4. DNA synthesis propagates at replication forks bidirectionally, with propagation speed or fork velocity v, from each activated origin. Experimentally, v is approximately constant throughout S phase.

5. DNA synthesis stops when two newly replicated regions of DNA meet.

From Fig. 2.1, it is apparent that processes 3–5 have a formal analogy with nucleation and growth in one dimension (see also Fig. 1.5). We identify (1) nucleation of islands as activation (initiation)

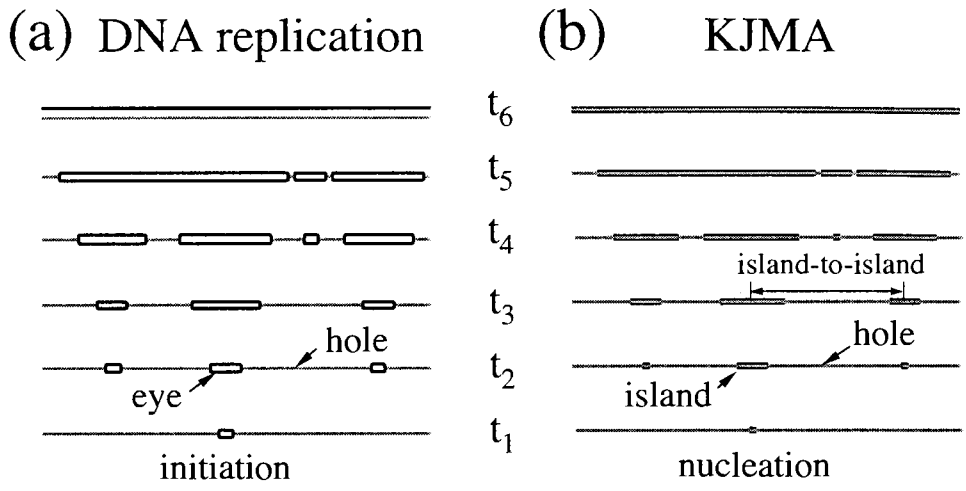

Figure 2.1: Mapping DNA replication onto the one-dimensional KJMA model.

of replication origins; (2) growth of the eyes as growth of the islands; and (3) coalescence of two expanding eyes as the merging of growing islands. Of course, while DNA is topologically one dimensional, it is embedded in a three-dimensional space.

In an ideal world, one could monitor the replication process continuously and compile domain statistics in real time. In the real world, the three billion DNA basepairs (bp) of a typical higher eukaryote, which replicate in as many as $\sim 10^5$ sites simultaneously, are packed in a cell nucleus of radius $\sim 1\ \mu m$, making a direct, real-time monitoring impossible [32]. In Ch. 4, we analyze an experiment that used two-color fluorescent labeling of DNA bases to study replication kinetics indirectly (Fig. 2.2).[1] Schematically, one begins (in a test tube) by labeling the bases used in replicating the DNA with, say, a red dye. At some time during the replication process (e.g., t_1 in Fig. 2.1), one floods the test tube with green-labeled bases and allows the replication cycle to go to completion. One then stretches the DNA onto a glass slide ("molecular combing" [23]), a process that unfortunately also breaks the DNA strands into finite segments. Under a microscope, regions that replicated before adding the dye are red, while those labeled afterwards are predominantly green. Typical two-color epifluorescence images of the combed DNA are shown in Fig. 2.3. The red-and-green regions correspond to eyes and holes in Fig. 2.1, forming a kind of snapshot of the replication state of the DNA fragment at the time the second dye was added. Each time point in Fig. 2.1 would

[1]The experimental details are described elsewhere [44], but the approach is similar to DNA fiber autoradiography developed by Huberman and Riggs, a method that has been in use for the last 30 years [60, 61].

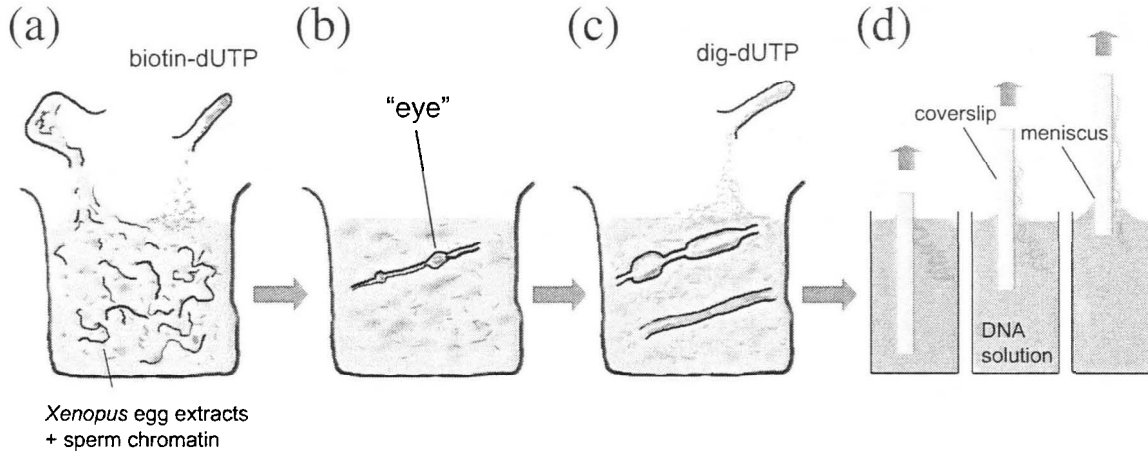

Figure 2.2: Schematic description of the double-labeling experiment. (a) Before replication starts, one adds "red dye" (biotin-dUTP) into the solution of *Xenopus* egg extracts and sperm chromatin. (b) "Eyes" then grow while more replication origins fire. (c) At chosen time points, one adds "green dye" (dig-dUTP) and waits until the DNA is completely replicated. (d) One then stretches the replicated DNA molecules in solution onto a glass surface ("molecular combing"). For more details, see text and Ref. [44].

thus correspond to a separate experiment.

The purpose of the present two chapters, then, is as follows: Here, in Ch. 2, we discuss the KJMA model and how to generalize it for biological application. In particular, we consider the problem of arbitrarily varying origin initiation rate (equivalent to arbitrarily varying nucleation rate in freezing processes). Then, in Ch. 3, we discuss a number of subtle but generic issues that arise in the application of the KJMA model to DNA replication. The most important of these is that the method of analysis runs backward from the usual one. Normally, one starts from a known nucleation rate (determined by temperature, mostly) and tries to deduce properties of the crystallization kinetics. In the biological experiments, the reverse is required: from measurements of statistics associated with replication, one wants to deduce the initiation rate $I(t)$. This problem, along with others relating to inevitable experimental limitations, merits separate consideration.

In the mid-1980s, Sekimoto showed that the analysis of the KJMA model could be pushed much further if growth occurs in only one spatial dimension [62–64]. Sekimoto used methods from non-equilibrium statistical physics to describe the detailed statistics of domain sizes and spacings, as defined in Fig. 2.1. In particular, he studied the time evolution of domain statistics by solving

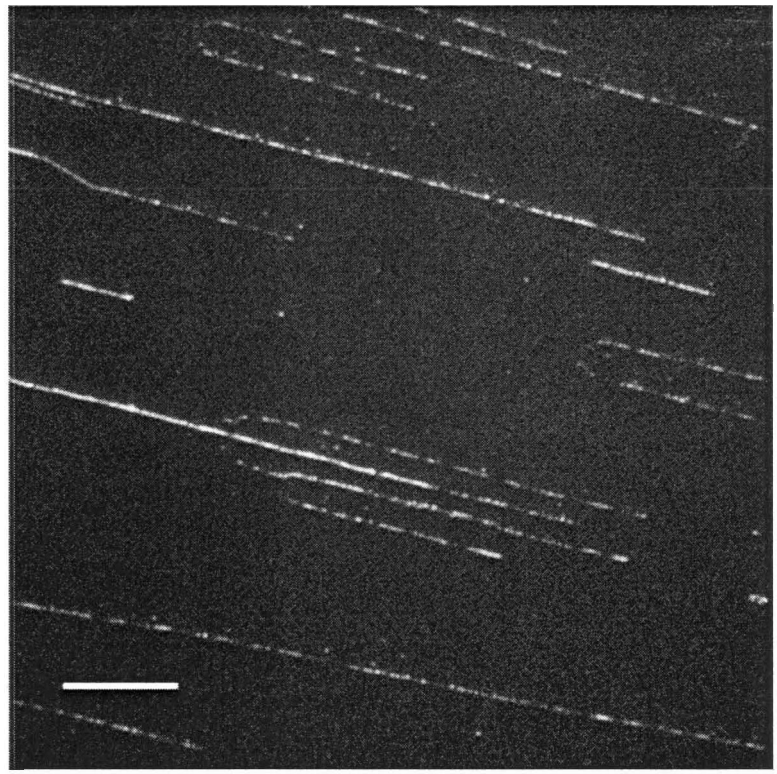

Figure 2.3: A fluorescence micrograph (bar = 20 μm). Early replicating sequences labeled with biotin-dUTP are visualized using red fluorescing antibodies (Texas Red). Later replicating sequences are in addition labeled with dig-dUTP and visualized using green (FITC) fluorescing antibodies. Courtesy of Aaron Bensimon and John Herrick.

Fokker-Planck-type equations for island and hole distributions, assuming that the nucleation rate $I(t)$ is constant. His approach has since been revisited by others (e.g., [65]).

Below, we review Sekimoto's approach and extend it to the case of an arbitrary nucleation rate $I(t)$. As mentioned above, this case is relevant to the kinetics of DNA replication in eukaryotes. We also present an algorithm to simulate 1D nucleation-and-growth processes that is much faster than more-standard lattice methods [66].

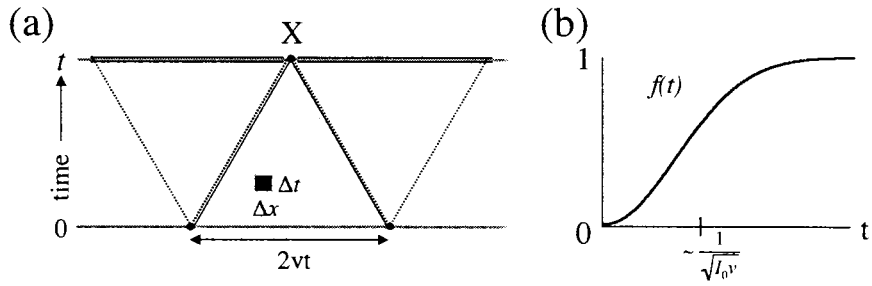

Figure 2.4: Kolmogorov's method for constant nucleation rate $I(t) = I_0$. (a) Spacetime diagram. In the small square box, the probability of nucleation is $I_0 \cdot \Delta x \cdot \Delta t$, where I_0 is the nucleation rate. In order for the point X to remain uncovered by islands, there should be no nucleation in the shaded triangle in spacetime. (b) Kinetic curve for constant nucleation rate I_0: $f(t) = 1 - \exp(-I_0 v t^2)$.

2.2 Theory

2.2.1 Island fraction $f(t)$

We begin with the calculation of $f(t)$, the fraction of islands at time t in a one-dimensional system. We write as $f(t) = 1 - S(t)$, where $S(t)$ is the fraction of the system uncovered by islands (i.e., the hole fraction). In other words, $S(t)$ is the probability for an arbitrary point X at time t to remain uncovered. If we view the evolution via a two-dimensional spacetime diagram [Fig. 2.4(a)], we can calculate S by noting that

$$\begin{aligned} S(t) &= \lim_{\Delta x, \Delta t \to 0} \prod_{x,t \in \triangle} (1 - I_0 \Delta x \Delta t) \\ &= \exp\left(- \iint_{x,t \in \triangle} I_0 dx dt \right) \\ &= \exp(-I_0 v t^2). \end{aligned} \tag{2.1}$$

Therefore,

$$f(t) = 1 - e^{-I_0 v t^2}, \tag{2.2}$$

which has a sigmoidal shape, as mentioned above [see Fig. 2.4(b)].

We note that Kolmogorov's method can be straightforwardly applied to any spatial dimension D for arbitrary time- and space-dependent nucleation rates $I(\vec{x}, t)$. Similar "time-cone" methods can yield $f(t)$ in the presence of complications such as finite system sizes [53–55]. Unfortunately, this

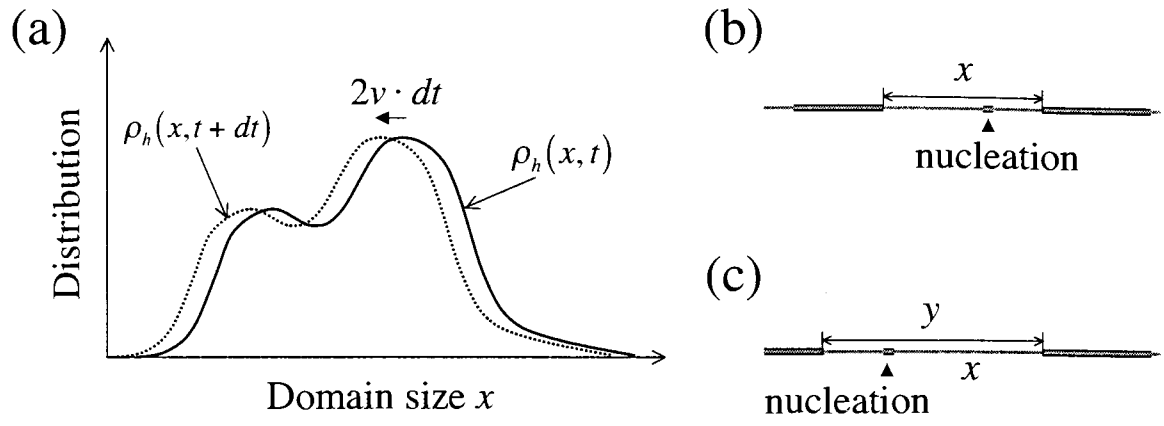

Figure 2.5: Illustration for evolution of $\rho_h(x,t)$. (a) Drift. (b) Annihilation due to nucleation. (c) Creation due to nucleation.

simple method cannot be used to calculate the distributions defined in Fig. 2.1, except that it can help solve the time-evolution equation for the hole-size distribution (see below).

2.2.2 Hole-size distribution $\rho_h(x,t)$

We define $\rho_h(x,t)$ as the homogeneous density of holes of size x at time t. For a spatially inhomogeneous system, $\rho_h(x,X,t)$ would be the density of holes of size x at the genome location X at time t. As mentioned in the text, we consider spatially homogeneous systems only. (For a spatially homogeneous nucleation function $I(t)$, the density ρ_h will also be spatially homogeneous.) The hole size x should not be confused with the genome spatial coordinate X. The time evolution $\rho_h(x,t)$ then has the following structure:

$$\frac{\partial \rho_h(x,t)}{\partial t} = [drift] + [annihilation] + [creation]. \tag{2.3}$$

In Fig. 2.5, we illustrate each term that describes the evolution of $\rho_h(x,t)$: First, in the absence of new nucleation or coalescence, each hole size decreases by $2v \cdot dt$ during the time interval dt. In other words, the size distribution $\rho_h(x,t)$ just drifts at a rate $2v$ without changing its shape [Fig. 2.5(a)]. Note that the change in $\rho(x,t)$ has the same sign for both $x \rightarrow x + dx$ and $t \rightarrow dt$. Second, any nucleation on a hole of size x between t and $t + dt$ makes the hole disappear [Fig. 2.5(b)]. The annihilation rate equals the the density of holes of size x times the number of new nucleations at t, namely, $-\rho_h(x,t)\, x\, I(t)$. Third, holes can be created by nucleation in a larger hole of size $y > x$

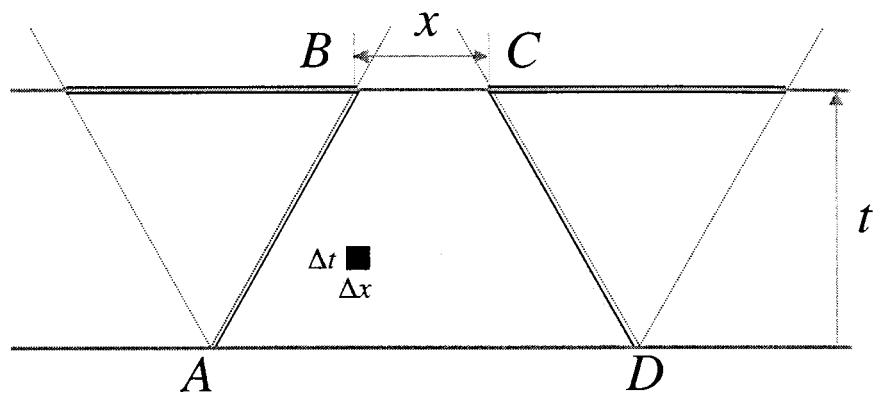

Figure 2.6: Spacetime diagram. The hole-size distribution $\rho_h(x,t)$ is proportional to the probability $p_0(x,t)$ for no nucleation event occurs in the shaded parallelogram $ABCD$ (see text).

[Fig. 2.5(c)].

Based on the arguments above, we obtain

$$\frac{\partial \rho_h(x,t)}{\partial t} = 2v\frac{\partial \rho_h(x,t)}{\partial x} - I(t)\, x\, \rho_h(x,t) + 2I(t)\int_x^\infty \rho_h(y,t)dy, \tag{2.4}$$

where the factor 2 in the last (creation) term comes from the left- and right-symmetry of the nucleation process.

Eq. 2.4 was solved by Sekimoto for $I(t)$=const., while Ben-Naim *et al.* derived a formal solution for arbitrary $I(t)$ [67]. Below, we show that the solution of Ben-Naim *et al.* can also be obtained directly by applying Kolmogorov's argument.

In Fig. 2.6, we see a hole of size x flanked by two islands. In order for such holes to exist at time t, there should be no nucleation within the parallelogram $ABCD$ in the spacetime diagram. Similar to the calculation of the hole fraction $S(t)$, we obtain the "no nucleation" probability in the parallelogram as

$$\begin{aligned} p_0(t) &= \lim_{\Delta x,\Delta t\to 0} \prod_{x,t\in ABCD} [1 - I(t)\Delta x\Delta t] \\ &= S(t)e^{-g(t)\cdot x}. \end{aligned} \tag{2.5}$$

where $g(t) = \int_0^t I(t')dt'$. The domain density $n(t)$ and the hole fraction $S(t)$ are related by defini-

tion as follows:

$$n(t) = \int_0^\infty \rho_h(x,t)dx \tag{2.6}$$

$$S(t) = \int_0^\infty x\,\rho_h(x,t)dx. \tag{2.7}$$

Since the hole-size distribution $\rho_h(x,t)$ is proportional to $p_0(x,t)$, we can write $\rho_h(x,t) = c(t) \cdot p_0(x,t)$. By integrating this equation and using Eq. 2.6, we obtain $c(t) = n(t) \cdot g(t)/S(t)$. Putting this back into Eq. 2.4, we obtain an equation for $n(t)$:

$$\frac{1}{n(t)}\frac{\partial n(t)}{\partial t} = -2v \cdot g(t) + \frac{I(t)}{g(t)}. \tag{2.8}$$

This is a first-order linear equation and can be solved exactly. Using the boundary condition $n(0) = 1$, we solve Eqs. 2.8 and 2.4 to find

$$n(t) = g(t) \cdot e^{-2v\int_0^t g(t')dt'}; \tag{2.9}$$

$$\rho_h(x,t) = g(t)^2 \cdot e^{-g(t)x - 2v\int_0^t g(t')dt'}. \tag{2.10}$$

These are just exponential functions of x, with decay constants that monotonically decrease as a function of time.

2.2.3 Island distribution $\rho_i(x,t)$

In analogy to Eq. 2.4 and following [63], a time-evolution equation can be obtained for the island-size distribution $\rho_i(x,t)$. In this case, the drift term is the same as in Eq. 2.4, except that the sign changes because islands always grow. On the other hand, new nucleations contribute to $\rho_i(x,t)$ only with sizeless ($x = 0$) islands with a rate $-\delta(x) \cdot \int_0^\infty I(t)\,x\,\rho_h(x,t)\,dx = -I(t)\,S(t)\,\delta(x)$ (see Eq. 2.6). Finally, coalescence of two islands can both annihilate and create islands of size x: for annihilation, either of the islands should have a size x; for creation, the sum of the sizes of the two islands should be x. The resulting equation can be written as

$$\frac{\partial \rho_i(x,t)}{\partial t} = -2v\frac{\partial \rho_i(x,t)}{\partial x} + I(t)\,S(t)\,\delta(x) + a(t)\Big[\int_0^x \rho_i(x-y,t)\rho_i(y,t)dy - 2n(t)\rho_i(x,t)\Big], \tag{2.11}$$

where $a(t)$ is a prefactor that should be determined. We recall that, in one-dimension, both holes and islands have the same domain density $n(t) = \int_0^\infty \rho(x,t)dx$. This means that $a(t)$ can be determined

by applying $\int_0^\infty dx$ to Eqs. 2.4 and 2.12 and comparing the two, as follows:

$$\begin{aligned}\frac{\partial n(t)}{\partial t} &= -2v\rho_h(0,t) - I(t)\,S(t) + 0 \\ \frac{\partial n(t)}{\partial t} &= 0 - I(t)\,S(t) + a(t)\cdot[n(t)^2 - 2\,n(t)^2].\end{aligned}$$

Thus, $a(t) = 2v\,\rho(0,t)/n(t)^2$ and we obtain

$$\begin{aligned}\frac{\partial \rho_i(x,t)}{\partial t} &= -2v\,\frac{\partial \rho_i(x,t)}{\partial x} + I(t)\,S(t)\,\delta(x) \\ &\quad +2v\,\frac{\rho_h(0,t)}{n(t)^2}\left[\int_0^x \rho_i(x-y,t)\rho_i(y,t)dy - 2n(t)\rho_i(x,t)\right].\end{aligned} \tag{2.12}$$

Unfortunately, we cannot solve Eq. 2.12 using the simple arguments that worked for $\rho_h(x,t)$. The main difference is that a hole is created by *nucleation* only, while an island of nonzero size is created by growth and/or the *coalescence* of two or more islands. Thus, $\rho_i(x,t)$ is given by an infinite sum of probabilities for an island to contain one seed, two seeds, three seeds, and so on. Nevertheless, we can still obtain the asymptotic behavior of $\rho_i(x,t)$ for arbitrary $I(t)$ by Laplace transforming the above evolution equation, as in [63].

Applying $\int_0^\infty dx e^{-sx}$ to Eq. 2.12, we find

$$\frac{\partial \tilde{\rho}_i(s,t)}{\partial t} = -2v\,[s + 2g(t)]\,\tilde{\rho}_i(s,t) + 2v\,e^{2v\int_0^t g(t')dt'}\cdot\tilde{\rho}_i(s,t)^2 + I(t)\,S(t), \tag{2.13}$$

where $\tilde{\rho}_i(s,t) \equiv \int_0^\infty e^{-sx}\rho_i(x,t)dx$, with initial conditions $\tilde{\rho}_i(s,0) = 0$. We can further simplify Eq. 2.13 by defining $\tilde{G}_i(s,t) = \exp\left[2v\int_0^t g(t')dt'\right]\cdot\tilde{\rho}_i(s,t)$, which then obeys

$$\frac{\partial \tilde{G}_i(s,t)}{\partial t} = -2v\,[s + g(t)]\,\tilde{G}_i(s,t) + 2v\,\tilde{G}_i(s,t)^2 + I(t). \tag{2.14}$$

If we write $\tilde{G}_i(s,t)$ as

$$\tilde{G}_i(s,t) = s + g(t) + \tilde{X}(s,t), \tag{2.15}$$

we find that $\tilde{X}(s,t)$ obeys the (nonlinear) Bernoulli equation [68]:

$$\frac{\partial \tilde{X}(s,t)}{\partial t} = [s + g(t)]\,\tilde{X}(s,t) + \tilde{X}(s,t)^2. \tag{2.16}$$

Solving Eq. 2.16 and substituting back into Eq. 2.15, we find the Laplace transform $\tilde{\rho}_i(s,t)$:

$$\begin{aligned}\tilde{\rho}_i(s,t) &= e^{-2v\int_0^t g(t')dt'}\,\tilde{G}_i(s,t) \\ &= e^{-2v\int_0^t g(t')dt'}\left\{s + g(t) - \frac{s\cdot\exp[2v(st + \int_0^t g(t')dt')]}{1 + 2v\cdot s\int_0^t \exp[2v(st' + \int_0^{t'} g(t'')dt'')]dt'}\right\}.\end{aligned} \tag{2.17}$$

We cannot perform the inverse Laplace transform of the above equation, even for the simple case of $I(t)$=const. [i.e., $g(t) \sim t$] [63, 65]. However, from the form of denominator in Eq. 2.17, we observe that $\tilde{\rho}_i(s,t)$ has a single simple pole along the negative real-axis at $|s = s^*(t)| \ll 1$ for $t \gg 1$, regardless of the form that $g(t)$ may have. Since the inverse Laplace transform can be written formally as the Bromwich integral in the complex plane (i.e., as the sum of residues of the integrand [69]), a standard strategy for obtaining an asymptotic approximation to $\rho_i(x,t)$ for $x \gg 1$ is to expand $\tilde{\rho}_i(s,t)$ around $s^*(t)$ ($|s^*(t)| \ll 1$) to lowest order. Following Sekimoto's approach, we define $K(s,t)$ to be the denominator in Eq. 2.17, which becomes

$$\tilde{\rho}_i(s,t) = e^{-\int_0^t g(t')dt'}\left[s + g(t) - \frac{1}{2v}\frac{\partial K(s,t)}{\partial t}\frac{1}{K(s,t)}\right],$$

Around $s = s^*(t)$, Eq. 2.17 can be approximated as

$$\begin{aligned}\tilde{\rho}_i(s,t) &\simeq \frac{e^{-\int_0^t g(t')dt'}}{-2v}\frac{\partial K(s^*(t),t)}{\partial t}\frac{1}{\frac{\partial K(s^*(t),t)}{\partial s}[s - s^*(t)]} \\ &= +\frac{e^{-\int_0^t g(t')dt'}}{2v}\frac{ds^*(t)}{dt}\frac{1}{s - s^*(t)}. \end{aligned} \tag{2.18}$$

From Eq. 2.18, we arrive at the following asymptotic expression for $\rho_i(x,t)$:

$$\rho_i(x,t) \simeq \frac{e^{-\int_0^t g(t')dt'}}{2v}\frac{ds^*(t)}{dt}e^{-|s^*(t)|\cdot x}, \tag{2.19}$$

for $x, t \gg 1$. Now, both the prefactor and the exponent [the pole $s^*(t)$] can be obtained very easily by simple numerical methods. On the other hand, an approximate expression for $s^*(t)$ itself can be found by first expanding $K(s,t)$ in powers of st and then solving iteratively using Newton's method [70]. (See Fig. 2.7) The result is

$$s^*(t) \simeq -\frac{1}{J_0}\left(1 + \frac{J_1}{J_0^2} + \frac{4J_1^2 - J_0 J_2}{2J_0^4}\right), \tag{2.20}$$

where

$$J_n \equiv \int_0^t e^{\int_0^\tau g(t')dt'}\tau^n d\tau.$$

As we shall show below, Eq. 2.19 describes the behavior of $\rho_i(x,t)$ accurately for $x \gtrsim 2vt$.

2.2.4 Island-to-island distribution $\rho_{i2i}(x,t)$

While most studies of 1D nucleation-growth have focused on $\rho_h(x,t)$ and $\rho_i(x,t)$ exclusively, the distribution of the distances between the centers of two adjacent islands [the island-to-island distribution $\rho_{i2i}(x,t)$] has important applications. For instance, whether homogeneous nucleation is a

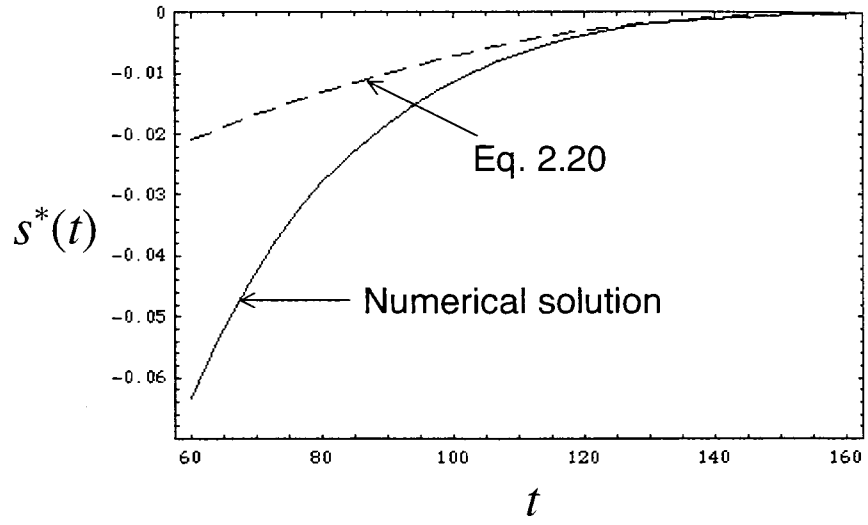

Figure 2.7: Plot of $s^*(t)$. The solid line is a direct numerical solution of $K(s,t) = 0$ and the dashed line is Eq. 2.20.

valid assumption cannot be known *a priori*. Indeed, in the recent DNA replication experiment that motivated this work, the "nucleation" sites for DNA replication along the genome were found to be not distributed randomly, a result that has important biological implications for cell-cycle regulation [71].

In the 1D KJMA model, Sekimoto has shown that a constant nucleation function I_0 cannot produce correlations between domain sizes [63, 64]. We speculate that the same holds true for any local nucleation function $I(x,t)$, a conclusion that is also supported by computer simulation[2] [71]. Assuming a local nucleation function, we can write the formal expression for $\rho_{i2i}(x,t)$ directly in terms of $\rho_i(x,t)$ and $\rho_h(x,t)$:

$$\rho_{i2i}(x,t) = c \int_{\{i_1,h,i_2\}\in S} \rho_i(i_1,t)\rho_h(h,t)\rho_i(i_2,t)dS, \tag{2.21}$$

where S designates the constraint plane shown in Fig. 5.3 [S : $(i_1 + i_2)/2{+}h{=}x$]. The normalization coefficient c can be obtained easily from the relation, $\int_0^\infty \rho_{i2i}(x,t)dx = \int_0^\infty \rho_i(x,t)dx = \int_0^\infty \rho_h(x,t)dx = n(t)$. From Eq. 2.21 and Fig. 5.3, it is easy to see that $\int_0^\infty \rho_{i2i}(x,t)dx = c[n(t)]^3$, and, therefore, $c = [n(t)]^{-2}$.

[2]Even for a 1D nucleation-and-growth system, spatial correlations can exist. For a theoretical study of deviations from the KJMA, see, for example, [72]. Blow *et al.* [24] and Jun *et al.* [71] present experimental evidence for size correlations of domain statistics in biological systems.

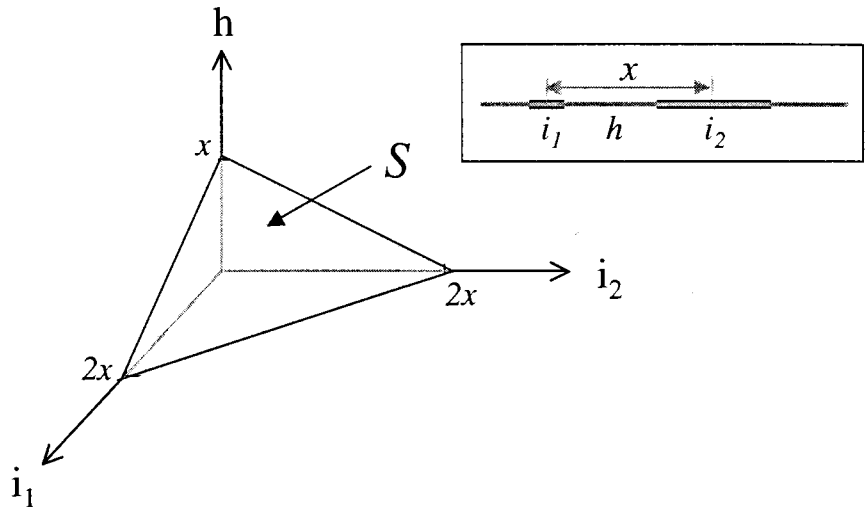

Figure 2.8: Constraint plane $S : (i_1 + i_2)/2 + h = x$.

Since the full solution for $\rho_i(x,t)$ is not known, we cannot integrate Eq. 2.21. However, we can still obtain an asymptotic expression for $\rho_{i2i}(x,t)$ using Eqs. 2.9 and 2.19. For $x \gg 1$, taking into account the constraint S, we find

$$\rho_{i2i}(x,t) \sim \int_{\{i_1,h,i_2\}\in S} e^{-|s^*(t)|\cdot i_1 - g(t)\cdot h - |s^*(t)|\cdot i_2} dS \tag{2.22a}$$

$$\sim e^{-g(t)x} + e^{-2|s^*(t)|x}\big[-1 + g(t)x - 2|s^*(t)|x\big]. \tag{2.22b}$$

As we shall show later, Eq. 2.22b is an excellent approximation for all x and t. Note that the first term on the right-hand side has the same asymptotic behavior as the hole-size distribution $\rho_h(x,t)$, while the exponential factor in the second term comes from the product of island-size distributions $\sim e^{-|s^*(t)|\cdot i_1}$ and $\sim e^{-|s^*(t)|\cdot i_2}$. The asymptotic behavior of $\rho_{i2i}(x,t)$ is dominated by $\rho_h(x,t)$ for $f < 0.5$ and by $\rho_i(x,t)$ for $f > 0.5$ (see below). But, at all times, we emphasize that $\rho_{i2i}(x,t)$ is asymptotically exponential for large x. From the mathematical point of view, both $\rho_i(x,t)$ and $\rho_h(x,t)$ have exponential tails at large x, and the integral of the product of exponential functions again produces an exponential.

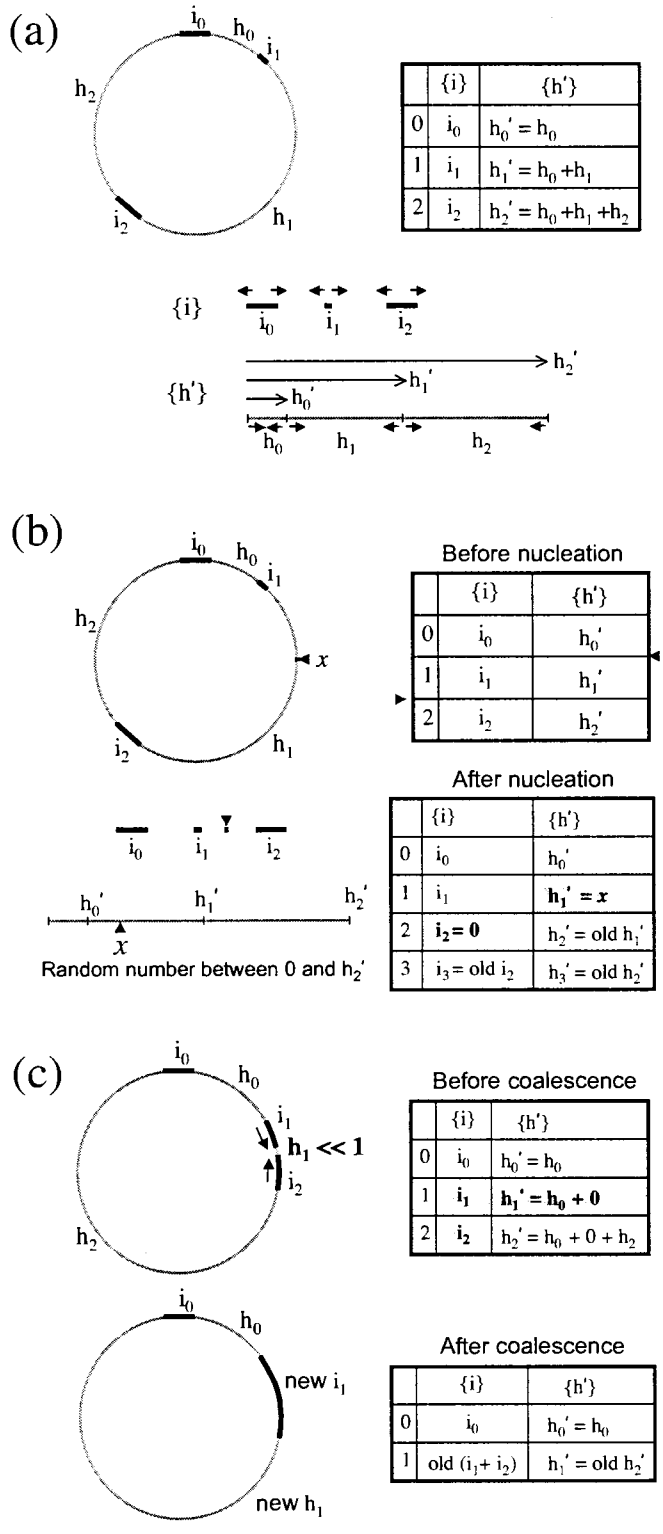

	{i}	{h'}
0	i_0	$h_0' = h_0$
1	i_1	$h_1' = h_0 + h_1$
2	i_2	$h_2' = h_0 + h_1 + h_2$

Before nucleation

	{i}	{h'}
0	i_0	h_0'
1	i_1	h_1'
2	i_2	h_2'

After nucleation

	{i}	{h'}
0	i_0	h_0'
1	i_1	$\mathbf{h_1' = x}$
2	$\mathbf{i_2 = 0}$	h_2' = old h_1'
3	i_3 = old i_2	h_3' = old h_2'

Before coalescence

	{i}	{h'}
0	i_0	$h_0' = h_0$
1	$\mathbf{i_1}$	$\mathbf{h_1' = h_0 + 0}$
2	$\mathbf{i_2}$	$h_2' = h_0 + 0 + h_2$

After coalescence

	{i}	{h'}
0	i_0	$h_0' = h_0$
1	old $(i_1 + i_2)$	h_1' = old h_2'

Figure 2.9: Schematic description of the double-list algorithm. (a) Basic set-up for lists $\{i\}$ and $\{h'\}$. Note that $\{h'\}$ records cumulative lengths. (b) Nucleation. (c) Coalescence due to growth.

2.3 Numerical simulation

Often, one has to deal with systems for which analytical results are difficult, if not impossible, to obtain. For example, the finite size of the system may affect its kinetics significantly, or the variation of growth velocity at different regions and/or different times could be important. In such cases, computer simulation is the most direct and practical approach.

For one-dimensional KJMA processes, the most straightforward simulation method is to use an Ising-model-like lattice, where each lattice site is assigned either 1 or 0 (or -1, for the Ising model) representing island and hole, respectively. The natural lattice size is $\Delta x = v \cdot \Delta t$, with v the growth velocity. At each timestep Δt of the simulation, every lattice site is examined. If 0, the site can be nucleated by the standard Monte Carlo procedure, i.e., a random number is generated and compared with the nucleation probability $I(t) \cdot \Delta x \cdot \Delta t$. If the random number is larger than the nucleation probability, the lattice site switches from 0 to 1. Once nucleation is done, the islands grow by Δx, namely, by one lattice size at each end.

Although straightforward to implement, the lattice model is slow and uses more memory than necessary, as one stores information not only for the moving domain boundaries but also for the bulk. Recently, Herrick *et al.* used a more efficient algorithm [59]. Specifically, they recorded the positions of moving island edges only. Naturally, the nucleation of an island creates two new, oppositely moving boundaries, while the coalescence of an island removes the colliding boundaries.

For the present study, we have developed an even more refined algorithm, which has improved both simulation and analysis speeds by a factor of up to 10^3 (Fig. 2.10). Fig. 2.9 describes schematically the new algorithm (hereafter, the "double-list" algorithm): The basic idea is to maintain two separate lists of lengths: $\{i\}$ for islands, $\{h\}$ for holes. [3] The second list $\{h\}$ records the cumulative lengths of holes, while $\{i\}$ lists the individual island sizes. Using cumulative hole lengths simplifies the nucleation routine dramatically. For instance, for times t ranging between τ and $\tau + \Delta\tau$, the average number of new nucleations is $\bar{N} = I(\tau) \cdot \Delta x \cdot \Delta t$. Since the nucleation process is Poissonian, we obtain the actual number of new nucleations $N = p(\bar{N})$ from the Poisson distribution p. We then generate N random numbers between 0 and the total hole size, namely, the largest cumulative length of holes h_{max} (the last element of $\{h\}$). The list $\{h\}$ is then updated by inserting the N generated numbers in their rank order. Accordingly, $\{i\}$ is automatically updated by inserting zeros at the corresponding places. If $\{h\}$ were to record the actual domain sizes as $\{i\}$ does, the nucleation

[3] A slightly different way to record individual hole sizes has been used by Ben-Naim *et al.* [65].

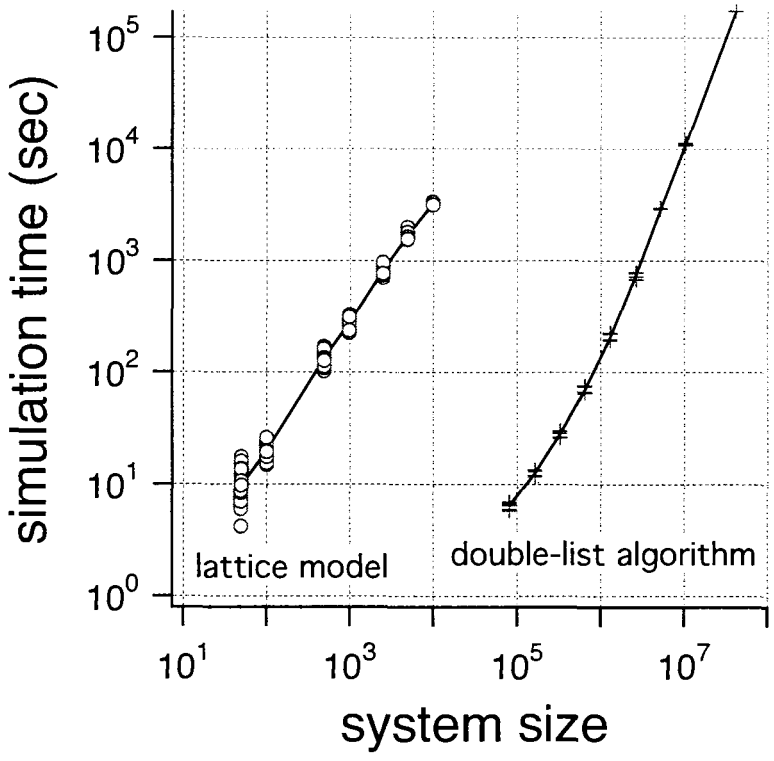

Figure 2.10: Comparison of simulation times for the two algorithms discussed in the text. For each system size, the number of Monte Carlo realizations ranges from 5–20. The lines connect the average simulation times. The double-list algorithm is two to three orders of magnitude faster.

routine would become much more complicated because the individual hole sizes would have to be taken into account as weighting factors in distributing the nucleation positions along the template.

Fig. 2.10 compares run times for the standard lattice model to the continuous double-list algorithm described above. We wrote and optimized both programs using the Igor Pro programming language [73], and they were run on a typical desktop computer (Apple Macintosh, 700 Mhz G4 processor). For both, we used the same simulation conditions: timestep $\Delta t = 0.1$, nucleation rate $I(t) = 10^{-5}t$, and growth velocity $v = 0.5$. Note that the performance of the lattice algorithm is $O(N)$, whereas the double-list algorithm is roughly $N^{1.5-2}$ for $10^5 \leq N \leq 10^7$. The main reason is that the double-list algorithm has to maintain dynamic lists $\{i\}$ and $\{h\}$. This requires searching and removing/inserting elements (as well as minor sorting), where each algorithm is linear, or

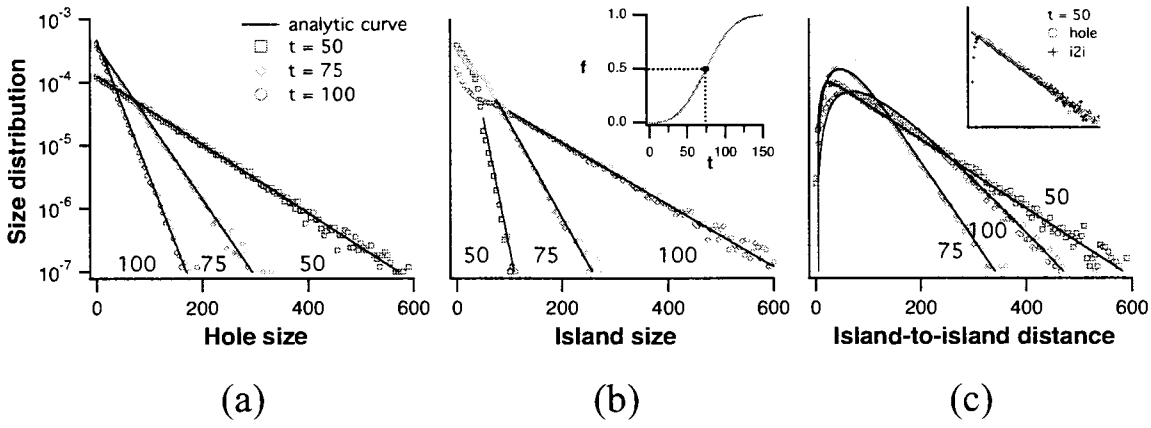

Figure 2.11: Theory and simulation results for $I(t) \sim t$. Size distributions are calculated at these timepoints: t = 50, 75, and 100. (a) Hole-size distribution $\rho_h(x,t)$. (b) Island distribution $\rho_i(x,t)$. The inset plots $f(t)$ vs. t, with the dot at $t = 75$ ($f = 0.5$). (c) Island-to-island distribution $\rho_{i2i}(x,t)$. The analytical curves have been obtained by Eq. 2.22b. There is a crossover of the decay constant slightly after t=75 ($f = 0.5$) (see text). The inset shows $\rho_h(x,t)$ and $\rho_{i2i}(x,t)$ for $t = 50$. All figures have the same vertical range of $10^{-7} - 10^{-3}$ (log-scale).

roughly $O(N^2)$ in overall. However, the double-list algorithm performed almost 3 orders of magnitudes faster even at a system size of 10^7, and we did not attempt to improve the efficiency further, for example, by using a binary search. By using a more rapid computer and coding the algorithm directly in a lower-level language such as C, one could presumably reduce the run time by a further factor of ~ 10.

Finally, the relative storage requirements for the lattice algorithm compared to the double-list algorithm can be estimated by the ratio N_{latt}/n_{max}, where N_{latt} is the total number lattice sites per unit length and n_{max} is the domain density. Equivalently, one may use $\ell_{min}/\Delta x$, where ℓ_{min} is the minimum island-to-island distance and Δx the lattice size. Since one usually sets up the simulation conditions such that $\ell_{min} \gg \Delta x$, the double-list algorithm requires much less memory.

In the next section, we present the simulation results.

2.4 Comparison between theory and simulation

In Fig. 2.11, we compare the various analytical results obtained in the previous sections with a Monte Carlo simulation. Shown are $\rho_h(x,t)$, $\rho_i(x,t)$, and $\rho_{i2i}(x,t)$ for $I(t) = 10^{-5}t$ at three different time points: t = 50, 75, and 100. The system size is 10^7 and the growth rate is $v = 1/2$. The chosen form of accelerating $I(t)$, linear in time, is the simplest nontrivial nucleation scenario. It is also relevant to the description of DNA replication kinetics in *Xenopus* early embryos, where the $I(t)$ extracted from experimental data has a bilinear form [59].

The agreement between simulation and analytical results is excellent. In particular, we emphasize that the analytic curves in Fig. 2.11 are not a fit. Note that, for $x \gg 1$, all three distributions decay exponentially as predicted by Eq. 2.9, 2.19, and 2.22b. [The $\rho_h(x,t)$ distributions are simple exponentials over the entire range of x.]

One interesting feature of $\rho_i(x,t)$ is the inflection point in the interval $0 \leq x \leq 2vt$, where $\rho_i(x,t)$ is slightly convex. Such behavior is even more dramatic when $I(t)$=const. [63], and $\rho_i(x,t)$ is strongly convex. In other words, $\rho_i(x,t)$ increases as x approaches $2vt^-$, but suddenly drops discontinuously at $x = 2vt$, decaying exponentially at larger x. This peculiar behavior of $\rho_i(x,t)$ originates from the fact that any island larger than $2vt$ must have resulted from the merger of smaller islands. Therefore, for $x \leq 2vt$, $\rho_i(x,t)$ has an extra contribution from islands that contain only a single seed in them, which makes $\rho_i(x,t)$ deviate from a simple exponential. Although such discontinuities are expected at every $x = n \cdot 2vt$ (n=1, 2, 3, ...), higher-order deviations decrease geometrically and are almost invisible.

Finally, the island-to-island distribution $\rho_{i2i}(x,t)$ provides important insight about the "seed distribution" and about the spatial homogeneity of the nucleation. Note that $\rho_{i2i}(x,t)$ is not monotonic and has a peak at $x > 0$ [see Fig. 2.11(c)]. This is not surprising because $\rho_{i2i}(x,t) \to 0$ as $x \to 0$ from Eq. 2.21. On the other hand, we see that $\rho_{i2i}(x,t)$ decays exponentially at large x, as predicted in the previous section (Eq. 2.22b). In contrast to $\rho_i(x,t)$ and $\rho_h(x,t)$, however, the decay constant is not a monotonic function of time. This can be understood as follows: at early times, the large island-to-island distances come from large holes and therefore $\rho_{i2i}(x,t) \sim \rho_h(x)$, as mentioned earlier. (The inset of Fig. 2.11(c) confirms this.) However, as the island fraction $f(t)$ approaches unity, the system becomes mainly covered by large islands, and $\rho_{i2i}(x,t)$ should approach $\sim \rho_i(x,t)^2$ asymptotically (see the second term in Eq. 2.22b).

In Fig. 2.12, we plot the decay constants for the three different distributions, τ_h, τ_i, and τ_{i2i}.

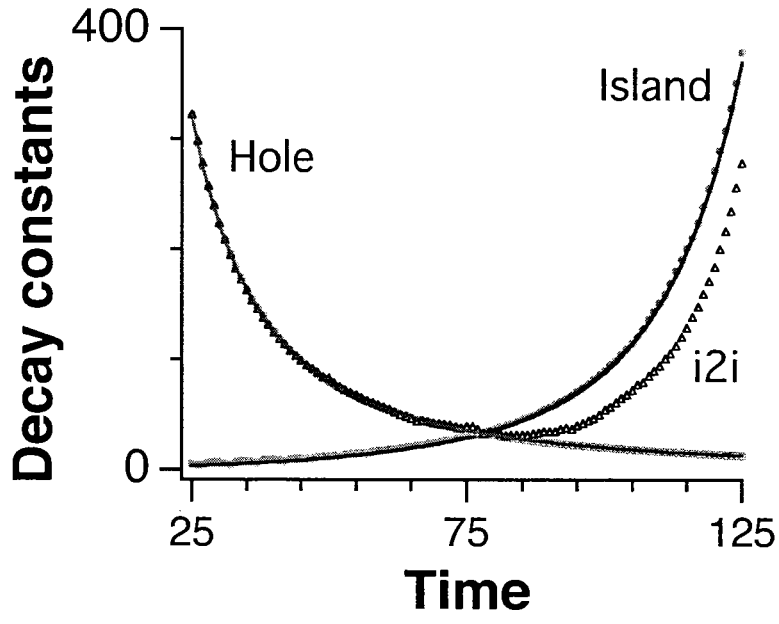

Figure 2.12: Decay constants for $\rho_h(x,t)$, $\rho_i(x,t)$, and $\rho_{i2i}(x,t)$. The symbols are simulations, and the solid lines are theory.

Note that when $f < 0.5$, $\tau_h \approx \tau_{i2i}$, as discussed above. As $f \to 1$, the behavior of τ_{i2i} is controlled by τ_i, as suggested by Eq. 20. Because $\rho_{i2i} \sim \rho_i^2$, we expect $\tau_{i2i} \to 0.5\,\tau_i$; however, the corrections to this relationship in Eq. 20 imply that this holds true only for large x and t. Note that the actual minimum of τ_{i2i} is at $f > 0.5$ because ρ_{i2i} depends on ρ_i^2 and not ρ_i alone.

One final note about the island-to-island distribution is that, unlike $\rho_i(x,t)$, it is a continuous function of x. The reason for this is that for any island-to-island distance x, the discontinuous $\rho_i(y < x, t)$ contributes to $\rho_{i2i}(x,t)$ in a cumulative way, as can be seen in Eq. 2.21. This implies that there is no specific length scale where discontinuity can come in. From a mathematical point of view, this is equivalent to saying that the integral of a piecewise discontinuous function (the integrand in Eq. 2.21) is continuous.

2.5 Conclusion

To summarize, we have extended the KJMA model to the case where the homogeneous nucleation rate is an arbitrary function $I(t)$ of time, deriving a number of analytic results concerning the properties of various domain distributions. We have also presented a highly efficient simulation algorithm for 1D nucleation-growth problems. Both analytical and simulation results are in excellent agreement.

In the next chapter, we discuss the application of these results to experiments in general and to the analysis of DNA replication kinetics in particular.

Chapter 3

Application to DNA Replication Kinetics

3.1 Introduction

Since its development in the late 1930s, the phenomenological model of nucleation and growth of Kolmogorov, Johnson-Mehl, and Avrami (KJMA) has been widely applied to the analysis of kinetics of first-order phase transformations, mostly in two and three spatial dimensions [39–43]. The model has several exact results given the following basic assumptions: (1) The system is infinitely large and untransformed at time t=0; (2) nucleations occur stochastically, homogeneously, and independently one from one another; (3) the transformed domains grow outward uniformly, keeping their shape; and (4) growing domains that impinge coalesce.

Although the KJMA model is conceptually simple, experiments often have complicating factors that make the contact between theory and experiment delicate and lead to deviations from the basic model. For example, a principal result of the KJMA model is that the fraction $f(t)$ of the transformed volume at time t is

$$f(t) = 1 - e^{-At^a}, \tag{3.1}$$

where A and a are constants: A depends upon the growth velocity v, the nucleation rate I, and the spatial dimension D, while a is determined by I and D. In the literature, a is called the Avrami exponent. "Avrami plots" of $-\ln[\ln(1-f)]$ vs. $\ln t$ should thus be straight lines of slope a.[1] Unfortunately, Eq. 3.1 often does not fit data well because the experimental conditions do not satisfy

[1] Eq. 3.1 comes from the more general expression $f(t) = 1 - \exp[-v^D \int I(\vec{x},t) d^D x]$, where the integral is performed over the so-called extended volume. For $D = 3$ and $I(\vec{x},t) = I = \text{const.}$, one obtains $f(t) = 1 - \exp(-\frac{\pi}{3} I v^3 t^4)$, giving $A = \frac{\pi}{3} I v^3$ and $\alpha = 4$. Note that different values of A are related by rescalings of v and I.

the assumptions of the KJMA theory [54, 74, 75]. For example, nucleation can be inhomogeneous or correlated [71, 76]; real systems are finite; and there is always measurement noise.

In two- or three-dimensional systems, where only limited theoretical results such as Eq. 3.1 are available, it can be difficult to pinpoint the origins of discrepancies between experimental data and the predictions of the KJMA model. In one-dimensional systems, however, we have seen in the previous chapter that one can push the analysis much further than for the original version of the KJMA model [62–65, 77].

In this chapter, we shall show that a detailed theoretical understanding of the KJMA model in 1D lets us compare theory and experiment more directly. In other words, we can extract the kinetic parameters from data under less-than-ideal experimental circumstances. Our discussion will be set in the context of recent DNA-replication experiments that have drawn attention from both the physics and biology communities [44, 59, 78].

3.2 Application of the 1D-KJMA Model to Experimental Systems

Although there are many analytical results for the 1D-KJMA model, only a very few 1D systems that are well-described by this model have been identified (e.g., [57]), and very little detailed analysis has been done on those systems. In the previous chapter, however, we have shown that DNA replication can be mapped onto the 1D nucleation-growth model. Equally important, Herrick *et al.* have developed experimental methods that can yield large quantities of data [44], allowing the extraction of biologically important, detailed statistical quantities (see Sec. 2.1). We can thus extract the kinetic parameters $I(t)$ and v from data using the results obtained in Ch. 2.

For the ideal case, the procedure is straightforward. For real-world data, on the other hand, one has to be cautious because of the generic problems explained above. We have already mentioned that the molecular combing process chops the DNA into finite-size segments, which effectively truncates the full statistics [44]. Another problem in the experimental protocols is that an *in vitro* replication experiment usually has many different nuclei in the test tube. These nuclei start replication at different, unknown times and locations along the genome [44, 78]. The asynchrony leads to sample heterogeneity and creates a starting-time distribution for the DNA replication [59]. Finally, the finite resolution of the microscope used to measure domain sizes may affect the statistics.

Below, we shall examine each of these complicating factors, present empirical criteria for their significance, and then discuss the implications of these criteria for the design of experiments.

To set the stage, we begin with the problem of extracting experimental parameters from ideal data.

3.2.1 Ideal case

From the theoretician's point of view, a system can be said to be ideal when it satisfies all underlying assumptions of the theory. In the context of DNA replication and the KJMA model, this means that the DNA molecule is infinitely long and that the initiation rate I of replication is homogeneous and uncorrelated. Also, statistics should be directly obtainable at any time point t at arbitrarily fine resolution. Because the growth velocity of replicated DNA domains has been measured to be approximately constant, we shall limit our analysis to this special case. One can then apply the KJMA model to a single experimental realization to extract kinetic parameters such as $I(t)$ and v.

In order to do this, we note that the simulation in Ch. 2 is in practice such a case (system size = 10^7, $v = 0.5$, $\Delta t = 0.1$, $I(t) = I \cdot t$, where $I = 10^{-5}$). Using the theoretical results obtained in the previous chapter, we can find an expression to invert $I(t)$ from data. For example, the domain density $n(t)$ and the island fraction $f(t)$ at time t, given a time-dependent nucleation rate $I(t)$ are

$$\begin{aligned} n(t) &= g(t)\, e^{-2v\int_0^t g(t')dt'} \\ f(t) &= 1 - S(t) \\ &= 1 - e^{-2v\int_0^t g(t')dt'}. \end{aligned} \tag{3.2}$$

In Eq. 3.2, $g(t) = \int_0^t I(t')dt'$, and $S(t)$ is the hole fraction. Note that $n(t)^{-1}$ is equal to the average island-to-island distance $\bar{\ell}_{i2i}(t)$ at time t. On the other hand, the average hole size $\bar{\ell}_h(t)$ is $S(t)/n(t) = g(t)^{-1}$. Since all three domains (island, hole, and island-to-island) have equal densities $n(t)$ in one dimension, we have the following general relationship among them, which is valid even in the presence of correlations between domain sizes:

$$\bar{\ell}_{i2i}(t) = \bar{\ell}_i(t) + \bar{\ell}_h(t) \tag{3.3a}$$

$$f(t) = \frac{\bar{\ell}_i(t)}{\bar{\ell}_i(t) + \bar{\ell}_h(t)}. \tag{3.3b}$$

In other words, there are only two independent quantities among $f(t), \bar{\ell}_i(t), \bar{\ell}_h(t), \bar{\ell}_{i2i}(t)$, and we

can calculate $\bar{\ell}_i(t)$ even if we do not know the exact expression for the island distribution $\rho_i(x,t)$:

$$\begin{aligned} \bar{\ell}_i(t) &= \frac{1}{g(t)}\left[e^{2v\int_0^t g(t')dt'} - 1\right] \\ \bar{\ell}_h(t) &= \frac{1}{g(t)} \\ \bar{\ell}_{i2i}(t) &= \frac{1}{g(t)} e^{2v\int_0^t g(t')dt'}. \end{aligned} \tag{3.4}$$

Note that $\bar{\ell}_i(t)$ [$\bar{\ell}_h(t)$] is a monotonically increasing (decreasing) function of time, and therefore, Eq. 3.3a implies that $\bar{\ell}_{i2i}(t)$ has a well-defined minimum. We emphasize that Eqs. 3.2 and 3.4 set the basic time and length scales, t^* and ℓ^*, of the system. Because the KJMA model has essentially only one scale, it is simpler than other common stochastic models in physics that lack an intrinsic scale and hence show fractal behavior (structure at all scales). Since $f(t)$ is sigmoidal, varying from 0 to 1, we define t^* to be the time required for the system to reach $f = 0.5$. On the other hand, we define ℓ^* to be the minimum eye-to-eye (island-to-island) distance during the course of replication [see Fig. 3.1(c) and (d)].

From Eqs. 3.2 and 3.4, it is straightfoward to invert the mean quantities to obtain the nucleation rate $I(t)$ and the growth velocity v:

$$\begin{aligned} I(t) &= \frac{d}{dt}\frac{1}{\bar{\ell}_h(t)} \\ v &= -\frac{1}{2}\frac{\ln S(t)}{\int_0^t \bar{\ell}_h(t')^{-1}dt'}. \end{aligned} \tag{3.5}$$

Eq. 3.5 can then be applied to an ideal set of data, i.e., one for which noise-free measurements are made on infinitely long DNA. As Fig. 3.1 shows, we can recover the input parameters from simulation results in Ch. 2 accurately: the extracted parameters are $I = (0.99 \pm 0.04) \times 10^{-5}$ and $v = 0.50 \pm 0.02$. [The errors are the statistical errors from the curve fits in Figs. 3.1(a) and (b)]. We note that the fluctuations visible for $t \gtrsim 75$ arise from using direct numerical differentiation in Eq. 3.5. One could reduce the noise by appropriate data processing, using for example a smoothing spline [70]. However, because any data filtering is a delicate issue, and because direct numerical differentiation produced satisfactory results, we have decided to forego any smoothing.

We also note that there are statistical fluctuations related to the finite-size of the system: as $f(t)$ approaches 1, the number of domains $n(t)$ becomes very small; thus even small changes in $n(t)$ can cause significant fluctuations in average domain sizes. However, the finite-size effect in this case becomes visible only when the number of new nucleations in each step, $N(t)$, is roughly 1 ($t \gtrsim 165$

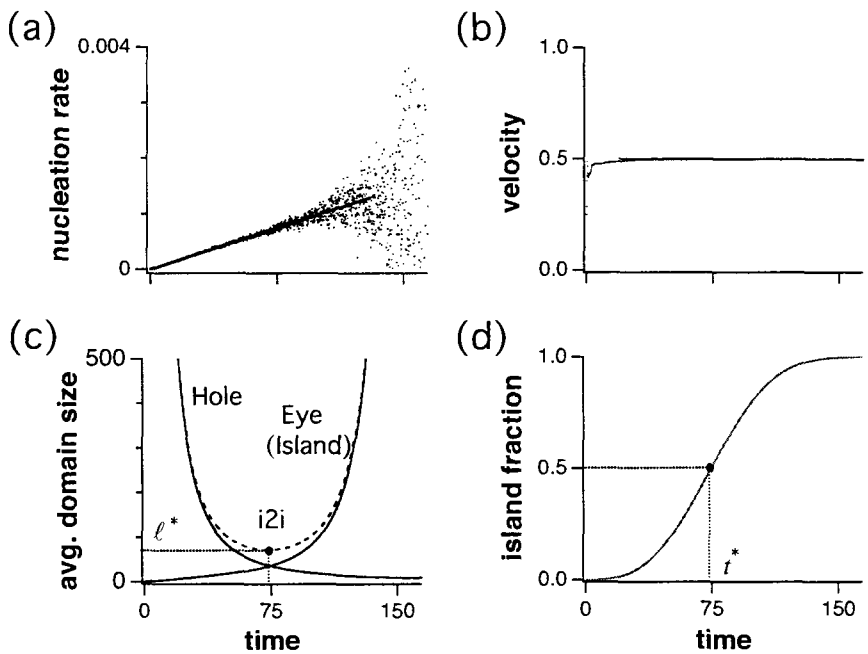

Figure 3.1: Parameter extraction from an almost ideal data set. (a) Inferred nucleation rate vs. time; (b) Velocity vs. time; (c) Average domain sizes vs. time; (d) Island fraction vs. time; theory and extracted $f(t)$ overlap. In (c), ℓ^* is the minimum average eye-to-to spacing, and sets the basic length scale. In (d), t^* is the time at which 50% of the genome has replicated. It sets the basic time scale.

or $f \gtrsim 0.999$). The effect can be ignored for $N(t) \gg 1$ for the practically infinite system considered here [53, 54].

In the following sections, we consider the complications that arise from less-ideal experimental conditions.

3.2.2 Asynchrony

As we mentioned above, data often come from experiments where the DNA from many different independently replicating cells is simultaneously present in the same test tube. The individual DNA molecules begin replicating at different unknown starting times. In such cases, it is simpler to begin by sorting data by the replicated fraction f of the measured segment [79]. The basic idea is that, for spatially homogeneous replication (namely, nucleation and growth), all segments with a similar fraction f are at roughly the same point in S phase. Since $f(t)$ is a monotonically increasing function

of t, we can essentially use f as our initial clock, leaving the conversion to real time t to a second step.

Once the data have been sorted by f, we extract the initiation frequency I as a function of f. Using Eqs. 3.2-3.4, one can straightforwardly obtain expressions analogous to Eq. 3.5:

$$\begin{aligned} \frac{I(f)}{2v} &= \frac{1}{\bar{\ell}_i + \bar{\ell}_h} \frac{d}{df} \frac{1}{\bar{\ell}_h} \\ 2vt(f) &= \int_0^f (\bar{\ell}_i + \bar{\ell}_h)\, df. \end{aligned} \tag{3.6}$$

In Eq. 3.6, $\bar{\ell}_i$ and $\bar{\ell}_h$ are functions of f. In other words, we have a direct inversion $I/2v$ vs. $2vt$ from data [Fig. 3.2(a)]. Note that both I and t are always accompanied by the factor $2v$, which has to be determined independently (see below). On the other hand, the fluctuations in the extracted $I/2v$ are the result of the direct numerical differentiation in Eq. 3.6 discussed in the previous section.

In the two-color labeling experiments, we can compile statistics into histograms of the distribution $\rho(f, \tau_i)$ of replicated fractions f at time τ_i [Fig. 3.2(b)], where τ_i is the timepoint where the second dye was added (Fig. 2.1). Note that the spread in $\rho(f, \tau_i)$ is related to the starting-time distribution $\phi(\tau)$ via the kinetic curve $f(t)$, where τ is the laboratory time that each DNA starts replicating, and t is the duration of time since the onset of replication. Since $\phi(\tau)d\tau = \rho(f(t), \tau_i) \cdot df(t)$, where $t = \tau_i - \tau$, we obtain

$$\rho(f, \tau_i) = \phi(\tau) \times \left(\frac{df}{d\tau}\Big|_{t=\tau_i - \tau} \right)^{-1}. \tag{3.7}$$

For a Gaussian starting time distribution $\phi(\tau)$, one can in principle fit all $\rho(f, \tau_i)$'s using three fitting parameters, v, the average starting time τ_0, and the starting time width σ_τ. Unfortunately, this "brute-force" approach did not produce satisfactory results, as the basin of attraction of the minimum proved to be relatively small.

Our strategy, then, was first to obtain a coarse-grained v vs. global χ^2 plot, shown in Fig. 3.2, as follows:

1. Guess a range of v between v_{min} and v_{max}.

2. Fix v (starting from $v = v_{min}$), and trace $\rho(f, \tau_i)$ back in time. For a specific value of f and timepoint τ_i, the corresponding starting time is $\tau_i - t(f)$ (Eq. 3.6). Repeat for all $\rho(f, \tau_i)$'s and reconstruct the starting time distribution $\phi(t)$.

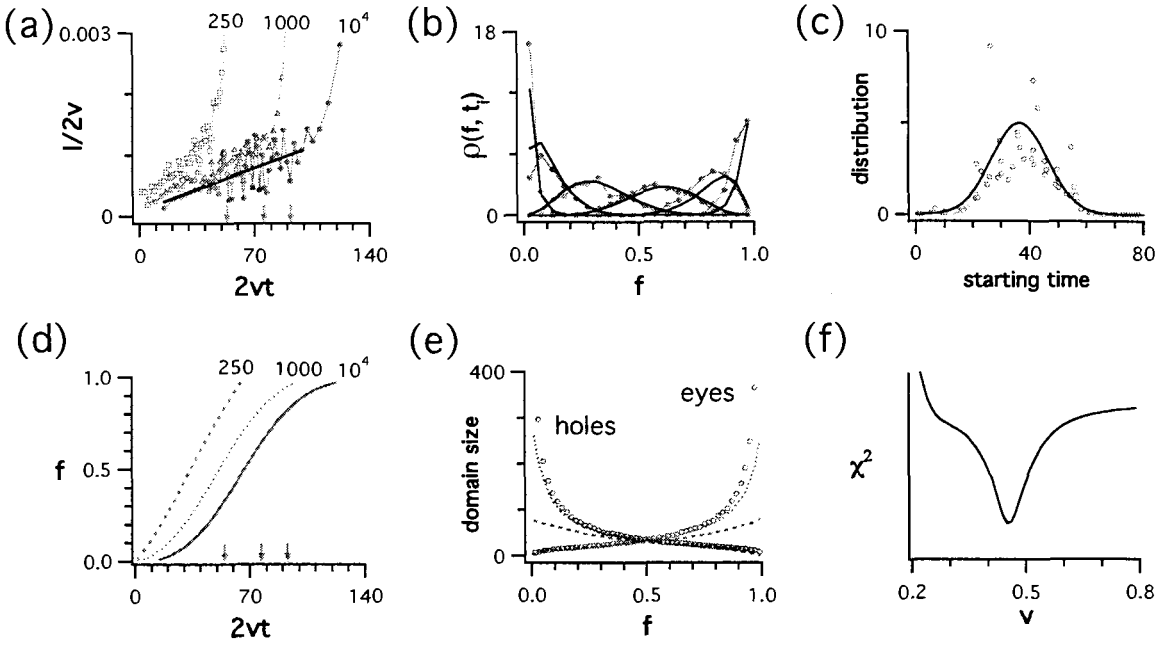

Figure 3.2: Inversion results in the presence of asynchrony and finite-size effects. (a) $I/2v$ vs. $2vt$. The arrows indicate where $f = 0.8$ in f vs. t curves in (d) for three different molecule sizes: 10^4 (unchopped), 1000 and 250 (chopped). (b) $\rho(f, \tau_i)$ for six time points 60, 80, 100, 120, 140, 160 (from left to right). The circles are simulation data; the solid lines are from Eq. 3.7, using the extracted parameters in Table 3.1. (c) Optimization results for the starting-time distribution $\phi(\tau)$. The solid line is a Gaussian fit. (d) f vs. $2vt$ for $\ell_c = 250$ and $\ell_c = 1000$. The solid line is the unchopped case (size 10^4). (e) Average domain sizes vs. f. The empty circles are for the unchopped case, while the dotted and dashed curves correspond to $\ell_c = 1000$ and 250. (f) Plot of $\log \chi^2$ $[\rho(f, \tau_i)]$ (arbitrary units) vs. v for size 10^4. The complete fit results are shown in Table 3.1. See also text.

3. Fit $\phi(\tau)$ obtained in step 1 to an empirical model. [In the absence of correlations among starting times, a Gaussian distribution is a reasonable choice.[2] One may also know the rough form of $\phi(\tau)$ from an understanding of the origins of the asynchrony.]

4. Regenerate $\rho(f, \tau_i)$ using Eq. 3.7 with the parameters obtained in steps 2 and 3. Calculate χ^2 for $\rho(f, \tau_i)$. This is also a global fit, as the χ^2 statistic is summed over data from all time

[2]Since the only relevant parameters of $\phi(\tau)$ are its mean and standard deviation, maximum-entropy arguments also justify the choice of a Gaussian distribution [80].

	input	extracted
I	1×10^{-5}	$(0.98 \pm 0.18) \times 10^{-5}$
v	0.5	0.453
starting t ($\tau_0 \pm \sigma_\tau$)	39.6 ± 14.1	36.5 ± 13.9

Table 3.1: Comparison between input and extracted parameters in the presence of asynchrony (starting t). Note that the input $\tau_0 \pm \sigma_\tau$ is the Gaussian fit to a single realization of 1000 molecules, where $\tau_0 = 40$ and $\sigma_\tau = 10$.[6]

points τ_i.

5. Increase v to $v+\Delta v$ and repeat 2–4. If there is a well-defined minimum of the $\chi^2(v)$ (with corresponding τ_0 and σ_τ) [e.g., Fig. 3.2(f)], one can find a more accurate estimate of the minimum using a standard optimization technique such as Brent's method [70].[3] Otherwise, go back to 1 and choose a different range of v.

In order to test how well the optimization method described above can work in the face of asynchrony, we have repeated the simulation in Ch. 2 with several modifications. First, we have used 1000 molecules that started nucleations asynchronously, following a Gaussian distribution of average starting time $\tau_0 = 40$ and of starting time width $\sigma_\tau = 10$.[4] Second, the size of each individual molecule is 10^4 instead of 10^7. This keeps constant the total number of "DNA basepairs" analyzed.

Since we used the same nucleation rate, the time to replicate to $f = 0.9$ was roughly 100 minutes, about the same as for the much larger system [see Fig. 3.1(d) and Fig. 3.2(d)]. We have chosen six timepoints ($\tau_i = 60, 80, 100, 120, 140, 160$) at which to collect data, and the distributions of fraction f are shown in Fig. 3.2(b). The spread in $\rho(f, \tau_i)$ reflects the starting time distribution $\phi(\tau)$.

We fit $I/2v$ vs. $2vt$ using $I(t) = a + I \cdot t$ in Fig. 3.2(a), excluding the last few points roughly above $f = 0.9$ to take into account the finite-size effect (see the following section). We then used the fit result to obtain the growth rate v by the optimization method given above. The results are shown

[3]The "Optimize" function in Igor Pro [73] uses Brent's method.

[4]We note that the actual realization of starting times in the particular simulation of Table 3.1 is $\tau_0 = 39.6$ and $\sigma_\tau = 14.1$. In other words, there are always errors related to the amount of data used in analysis, but this is a separate issue from the extraction methods presented here.

in Fig. 3.2 and Table 3.1. In the plot of χ^2 vs. v [Fig. 3.2(f)], we see a well-defined minimum of χ^2 at $v = 0.453$, 10% below the input value 0.5. Fig. 3.2(b) and (c) are reconstructions of $\rho(f, \tau_i)$ and $\phi(\tau)$ using the parameters in Table 3.1. The minor discrepancies in τ_0 and σ_τ are acceptable, given the small number of points of $\rho(f, \tau_i)$ used in the optimization (20 points in each of six histograms). Note that the finite size of sampled DNA is responsible for a larger part of the discrepancy with the original parameters than was our reconstruction algorithm.

The success of this method depends on the experimental design, as well; i.e., one has to choose the right timepoints τ_i in order to deduce $\phi(\tau)$ accurately [see Fig. 3.2(b) and (c)]. The key parameter is the ratio α between the replication time scale t^* and the starting-time width σ_τ, respectively: $\alpha = t^*/\sigma_\tau$. For the case considered here ($t^* \approx 75$ and $\sigma_\tau \approx 14$), $\alpha \approx 5.4$.

Ideally, $\alpha \gg 1$ (better synchrony with slow kinetics), so that $\rho(f, \tau_i)$ has a well-defined peak between $0 < f < 1$, and $\rho(f, \tau_i) \to 0$ as $f \to 0$ and 1. In this case, even a single $\rho(f, \tau_i)$ can be used to reconstruct $\phi(\tau)$ and extract v accurately. For example, for all timepoints in Fig. 3.2(b) each single histogram produced results that are accurate to 15%.

For $\alpha \ll 1$ (high asynchrony with fast kinetics), $\rho(f, \tau_i)$ is spread over $0 \leq f \leq 1$. In this case, experimentalists should choose at least $N = \sigma_\tau/t^*$ timepoints to cover the whole range of $\phi(\tau)$, where well-chosen τ_i's spread evenly the peaks of $\rho(f, \tau_i)$ between 0 and 1.

3.2.3 Finite-size effects

As mentioned above, the DNA is broken up into relatively short segments during the molecular-combing experiments. In order to estimate how the finite segment size affects the estimates of $I(t)$ and v, we have cut the simulated molecules in the previous section into smaller pieces of equal size ℓ_c.[7] Fig. 3.2 shows results for ℓ_c = 1000 and 250, with original size 10^4. As one can see, there is a clear correlation between ℓ_c and the statistics. First, the smaller the segments are, the smaller the average domain sizes become as $f \to 1$. This is as expected, since one obviously cannot observe a domain size larger than ℓ_c. Note that an underestimate of average eye and hole sizes, $\bar{\ell}_i$ and $\bar{\ell}_h$, leads to an overestimate of the extracted $I(t)$, as implied by Eq. 3.6. Second, as ℓ_c becomes smaller, the completion times are underestimated. Third, the sharp increase (decrease) in average eye (hole) sizes disappears, becoming nearly flat at a characteristic fraction f^*, and the kinetic curve

[7]Experimentally, the size distribution of DNA fragments is log normal. See Fig. 4.8. Similar finite-size effects are obtained for any unimodal distribution with the same mean.

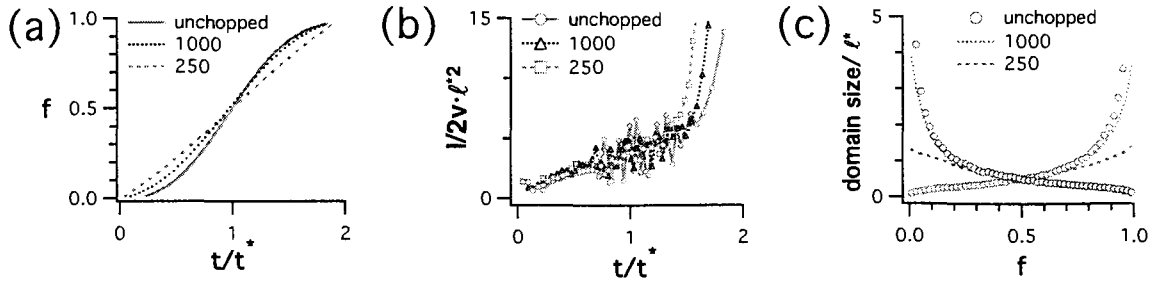

Figure 3.3: Rescaled graphs for finite-size effects (see text). (a) f vs. t/t^*. (b) $\frac{I}{2v}\ell^2$ vs. t/t^*. (c) ℓ/ℓ^* vs. f, where ℓ is the average hole (eye) size.

$f(t)$ significantly deviates from its sigmoidal shape, becoming nearly linear. In fact, there is a close relationship between these last two effects. The sharp increase in average eye size results from the merger of smaller eyes, which dominates the late stage of replication kinetics. Since chopping DNA eliminates the large eyes, as shown in Fig. 3.2(e), it effectively increases the number of domains $n(t)$ per unit length in truncated segments and overestimates the replication rate. (The replication rate $df/dt = 2vn$.)

We emphasize that the first two observations above imply that ℓ_c affects the basic time and length scales, t^* and ℓ^*, of the (chopped) systems introduced in the previous section. In Figs. 3.3(a)-(c), we re-plot $f(t)$, $I(t)$, and $\bar{\ell}_i$ and $\bar{\ell}_h$ using the dimensionless axes. One can clearly see that the chopping process straightens the sigmoidal $f(t)$ and the average domain size curves. Nevertheless, the basic shape of $I(t)$ does not change: curves corresponding to different values of ℓ_c collapse onto one another, and the finite-size effect only makes the up-shooting tails steeper.

As criteria for significance of finite-size effects, we first define a new parameter $\beta = \ell_c/\ell^*$, namely, the maximum average number of domains per chopped molecule (around $f = 0.5$). Then, more careful observation of Figs. 3.3(a) and (c) suggests that there might exist a critical value β^* (or corresponding chopping size ℓ_c^*), where the finite-size effects severely affect the statistics. In other words, for $\beta > \beta^*$, one can ignore the finite-size effects by excluding the last few data points close to $f = 1$ (Recall that ℓ^* is the minimum average eye-to-eye spacing). To see this clearly, in Fig. 3.4, we have plotted t^*/t^*_∞ vs. β for two different cases: $I(t) = 10^{-5}\,t$ and $I(t) = 0.001$, where t^*_∞ has been calculated using the basic kinetic curve $f(t) = 1 - \exp[-2v\int_0^t g(t')dt']$ (i.e., the system is infinitely large) [77] (see also footnote 1 under Eq. 3.1).

Indeed, changes in t^* are very slow above $\beta \approx 10$, but drop sharply below this ratio. Since β

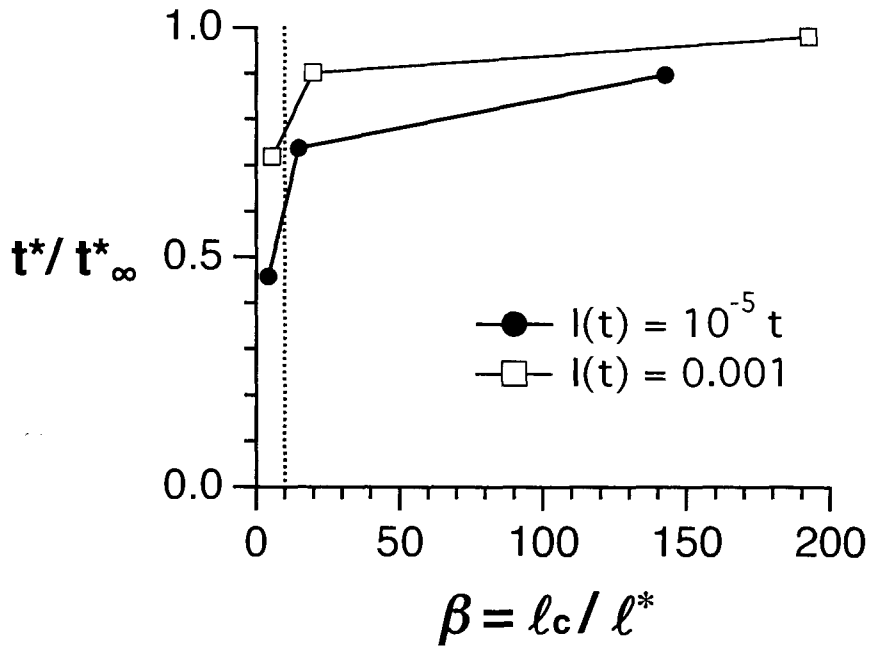

Figure 3.4: The finite-size effects and changes in the basic time and length scales. Shown are two different initiation rates $I(t) = 10^{-5}t$ and $I(t) = 0.001$. The vertical line is where the average number of domains per molecule is 10. The y-axis has been normalized relative to the initiation rate for an infinite system ($\beta \to \infty$).

is the average number of domains per molecule, we argue that the KJMA model can be applied to data directly when there are enough eyes in individual molecule fragments (roughly, at least 10). On the other hand, when $\beta \lesssim 10$, one would require more sophisticated theoretical methods to obtain correct statistics.

One subtle point is that t^*, unlike ℓ^*, is not very accessible experimentally and requires data processing for accurate extraction [e.g., Fig. 3.2(d) or Fig. 3.5(b)].

Finally, we note that the sudden up-shooting in the tails of the extracted $I(t)/2v$ vs. $2vt$ curves is yet another kind of finite-size effect related to numerical differentiation (Eq. 3.5). This can be simply excluded from the analysis.

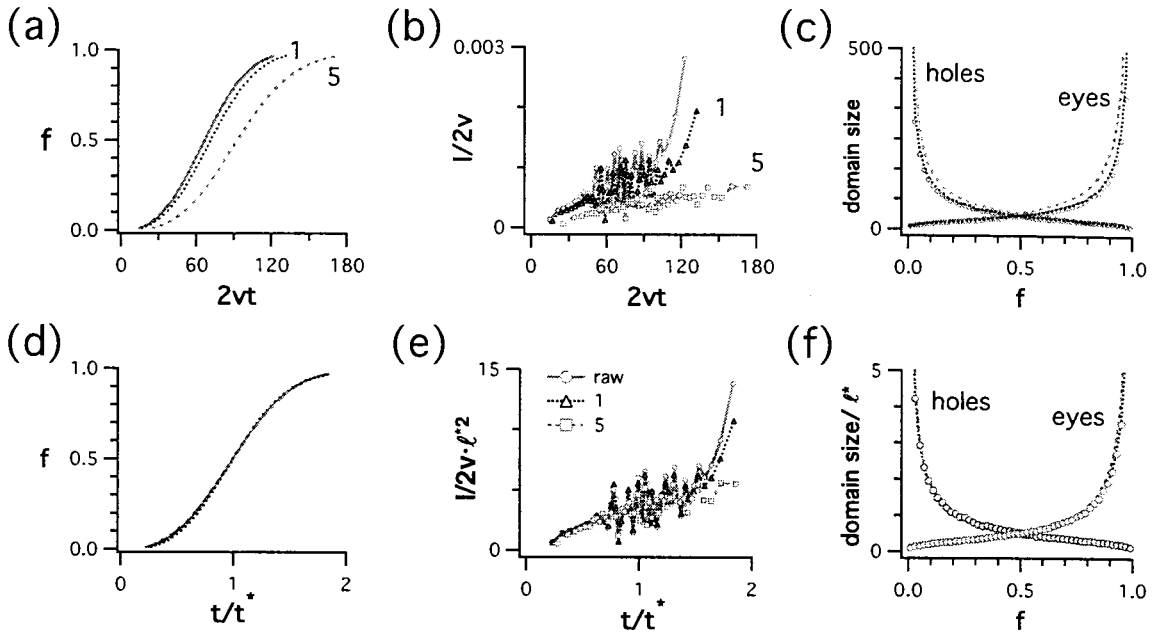

Figure 3.5: The effect of coarse-graining. (a) f vs. $2vt$. From left to right, $\Delta x^* = 0$, 1, 5. (b) $I/2v$ vs. $2vt$. From top to bottom, the coarse-graining factor $\Delta x^* = 0$ (no coarse-graining), 1 (comparable to optical resolution), and 5. (c) Average domain sizes vs. f. The empty circles are for no coarse-graining, while the dashed lines are for $\Delta x^* = 1$ and 5 (dotted and dashed, respectively). (d)-(f) Rescaled graphs.

3.2.4 Finite-resolution effect

Another generic problem is the finite resolution of measurements. In molecular-combing experiments, for example, epifluorescence microscopy is used to scan the fluorescent tracks of combed DNA on glass slides. The spatial resolution ($\sim$1 kb) means that smaller domains will not be detectable. Thus, two eyes separated by a hole of size $\leq$ 1 kb will be falsely assumed to be one longer eye. We evaluate this effect by coarse-graining the statistics with experimental resolutions Δx^*, while keeping $\Delta x = v \cdot dt$ in simulation much finer. To coarse grain by a factor $\delta = \Delta x^*/\Delta x$, we have used the raw, "unchopped" data set in the previous finite-size-effect section: after the simulation, we have scanned the final lists of eyes and holes, $\{i\}$ and $\{h\}$, and removed any eyes (holes) for $\delta < 1$, combining them with the two flanking holes (eyes) into a larger hole (eye) that equals the size of all three domains.

In Figs. 3.5(a)-(c), we show how the statistics change by coarse-graining only (i.e., without chopping), where the coarse-graining factors δ are 20 and 100.

The finite-resolution effect biases estimates in a way that is opposite to finite-size effects, i.e., converting eyes (holes) for $\delta < 1$ to holes (eyes) increases the average domain sizes. As a consequence, the extracted $I(t)$ is slightly underestimated. Nevertheless, the curves in each of $f(t)$, $I(t)$, and $\bar{\ell}_i$ and $\bar{\ell}_h$ almost perfectly collapse onto each other when the axes are rescaled using t^* and ℓ^*, confirming that, as with finite-size effects, the main consequence is a change in the basic time and length scales of the problem [Fig. 3.5(d)-(f)].

To find criteria for significance of finite-resolution effects, we recall that coarse-graining falsely eliminates eyes and holes smaller than the resolution Δx^* only ($\delta < 1$). For example, statistics for $f \approx 0$ (small eyes) or $f \approx 1$ (small holes) can be affected by coarse-graining. For these two cases, however, one can easily avoid a problem by excluding data for $f \approx 0$ and 1 from analysis.

On the other hand, a more serious situation can arise when $\gamma = \ell^*/\Delta x^* \lesssim 1$, because a resolution comparable to the minimum eye-to-eye distance will seriously alter the mean domain sizes $\bar{\ell}_i$ and $\bar{\ell}_h$ and thus the extracted $I(t)$, as well. Indeed, for $\gamma \gg 1$, the $\rho(f, \tau_i)$'s remain essentially unchanged (i.e., the optimization result for v remains the same) even at $\delta = 100$ (where, $\gamma \approx 70$) (data not shown). We conclude that $\gamma = 1$ is the relevant criterion to test the significance of finite-resolution effects.

3.3 Discussion and Conclusion

In the previous section, we have tested various generic experimental limitations via Monte Carlo simulation. When the system is large (10^7 for $v = 0.5$ and $I(t) = 10^{-5}\,t$), we have been able to extract all the input parameters accurately from a single realization of our simulation. As the experimental (simulation) conditions become less ideal, however, one requires more sophisticated tools.

In the presence of asynchrony, we have demonstrated that the input parameters can still be extracted to reasonable accuracy (roughly 10% for $\alpha \approx 5.4$) using an optimization method. In most DNA replication experiments, $\alpha \gtrsim 1$. In this case, the method presented here can even be applied to data $\rho(f, \tau_i)$ for a single well-chosen timepoint τ_i to extract v. The accuracy increases as more data are collected for different timepoints. Similarly, the significance of finite-size and finite-resolution effects can be estimated by the criterion $\beta = \ell^*/\ell_c \approx 10$ and $\gamma = \ell^*/\Delta x^* > 1$, respectively.

Among the various experimental limitations we have tested, the finite-size effects seem to be potentially the most serious problem in the molecular-combing experiments. Fortunately, we expect the finite-size effects in the experiments and analysis of refs. [44, 59] and in Ch. 4 to be relatively insignificant because $\beta > 10$. On the other hand, we need more sophisticated theoretical tools to correct the finite-size effects for $\beta < 10$. We recall that the coarse-graining of molecules affects the tails in Fig. 3.5(b) opposite to the way the finite-size of molecules affects them. We thus speculate that an intelligent way of annealing finite-sized molecules can reduce or correct the finite-size effects. We leave a detailed evaluation of this idea for future work.

In summary, we have discussed how to apply the KJMA model to data to extract kinetic parameters under various experimental limitations, such as asynchrony, finite-size, and finite-resolution effects. For the application to DNA-replication experiments, we have shown that finite-size effects can be ignored when the chopped molecules contain enough domains (i.e., $\beta \gtrsim 10$). Even when the size of molecules is smaller than the critical value ℓ_c^*, the shape of the nucleation rate $I(t)$ is not affected when plotted using rescaled parameters. On the other hand, finite-resolution effects are insignificant when $\gamma \gg 1$, which is the case for molecular combing experiments of DNA replication.

In the next chapter, we apply the analysis methods developed here to actual data from recent experiments on the *Xenopus* egg-extract system.

Chapter 4

Temporal Program of *Xenopus* Early-Embryo DNA Replication

4.1 Introduction

In the previous two chapters, we have introduced the KJMA model of nucleation-and-growth and have extended its 1D version to the case of arbitrary nucleation rate $I(t)$ [77]. We then mapped DNA replication processes onto the KJMA model and demonstrated that the "kinetic model" can be used to extract parameters such as the frequency of origin firings $I(t)$ and fork-growth rate v, which govern the kinetics of DNA replication [59, 81].

As replicon size and the duration of S phase depend on the values of these parameters, this information is indispensable for understanding the mechanisms regulating S phase in a given cell system [36, 82–87]. In other words, understanding how these parameters are coordinated during the replication of the genome is essential for elucidating the mechanism by which S phase is regulated in eukaryotic cells. In particular, the extracted $I(t)$ can be interpreted as a "temporal" program of DNA replication, suggesting a vocabulary that we find useful and intuitive for understanding the process of replication of various higher eukrayotes from a single unified theoretical framework.

As we shall see, the key feature of recent DNA replication experiments is that they have gathered much more data than previous experiments could possibly have obtained. In order to appreciate these advances, we review briefly some of the experimental methods used to analyze DNA replication. For a more detailed review of classic methods, see the book edited by S. Cotterill [88].

In the 1960s, several researchers used autoradiography [60, 89] and electron microscopy [90] to visualize DNA fibers of lengths ranging from μm to mm. It soon became obvious that one can use these visualization techniques to study DNA replication. Indeed, Huberman and Riggs in 1968 labeled replicating DNA molecules in vivo with ^{3}H-thymidine and stretched them out on filters or microscope slides and then autoradiographed them [91]. Wherever ^{3}H-thymidine had been incorporated into the DNA molecule, a track of silver grains was generated in the overlying photographic emulsion (sensitive to the β-particles given off by ^{3}H), and the density of silver grains in those tracks was proportional to the specific activity of the ^{3}H-thymidine. Thus, by intentionally altering the specific activity of the ^{3}H-thymidine during an experiment, they could infer the direction of DNA replication fork movement (as well as measure the fork movement rates and distances between origins) from the corresponding change in grain density in the final autoradiogram. In the mean time, electron micrographs were actively used to study DNA replication. In the 1970s, for example, Kriegstein and Hogness confirmed the bidirectional growth of replication forks [33], while Blumenthal *et al.* analyzed spatio-temporal distribution of replication bubbles [79] of *Drosophila* early embryos.

In the 1980s and 1990s, similar but improved techniques were developed, such as the use of fluorescent molecules instead of radioactive thymidine. An important example is fluorescence in situ hybridization (FISH) [92, 93]. In this technique, the DNA probe is either labeled directly by incorporation of a fluorescent-labeled nucleotide precursor, or indirectly by incorporation of a nucleotide containing a reporter molecule (such as biotin or digoxigenin) which after incorporation into the DNA is then bound to a fluorescently labeled affinity molecule.

FISH can also be combined with other powerful techniques to achieve high-resolution mapping. These techniques usually stretch DNA before hybridization. For example, direct visual hybridization (DIRVISH) involves lysing cells with detergent at one end of a glass slide, tipping the slide, and allowing the DNA in solution to stream down the slide [24, 25, 94, 95]. The molecular-combing technique [23] used in the *Xenopus* experiments of Herrick *et al.* relies on the action of a receding air/water interface, or meniscus, to uniformly straighten and align DNA molecules on a solid surface [see Fig. 2.2(d)]. Molecular combing has the advantage not only of producing large quantities of data but also of reproducibly stretching the DNA at a controlled extension. Thus, there is an accurate mapping between distances measured on a digital image and lengths along the genome. As explained in Sec. 2.1, these techniques can produce "snapshots" of replicating DNA that mimic the space-time diagram in Fig. 2.1. (See Fig. 2.3.)

Although different from the labeling and stretching techniques mentioned above, 2D-gel electrophoresis [96, 97] and DNA microarrays [98–100] have also been important tools to study replication kinetics, including mapping replication origins. For example, 2D gel electrophoresis allows the separation of DNA fragments based on both size and shape, thereby separating molecules containing branches in various arrangements (e.g., bubble or Y shapes) from linear molecules. Thus, by using restriction enzymes that cut DNA at specific sequences, one can map replication origins using 2D. In particular, the ratio of bubble-shaped molecules to Y-shaped molecules provides a qualitative estimate of origin efficiency, the relative fraction of cell cycles in which a given origin is activated [86, 101, 102].

Finally, microarrays containing an ordered set of unique-sequence DNA probes can be used to monitor DNA replication. They are well-suited for giving information about particular sites along the genome. For example, in a synchronous population of cells, those genes that have replicated are twice as abundant as unreplicated genes. One can then identify the position of replication forks by measuring the abundance of each gene, which is proportional to the amount of DNA that hybridizes to the array [98]. Similar methods can be extended to construct replication profiles containing precise locations of replication origins and fork velocities between neighboring origins [99].

These new experimental techniques now make it possible to extract large amounts of data from the replication process, giving detailed statistics about numbers and sizes of replicated domains as averaged over the genome, as well as many other related quantities. In particular, in the experiments by Herrick *et al.* discussed in this thesis [44], over 200 Mb of DNA replication fragments was analyzed.

4.2 Results

In this chapter, we apply the KJMA formalism developed in the previous two chapters to recent experiments on DNA replication in a particular model system of *Xenopus* egg extracts. Although our analysis is particular to this system, we stress that it is easily adaptable to experiments on other systems and experimental data described above.[1]

Since the kinetics of DNA replication in any cell system depends on two fundamental quantities, $I(t)$ and v, one of the principal goals of our analysis is to derive accurate values for these quantities,

[1]This type of model has also been shown to apply for the case of RecA polymerizing on a single molecule of DNA [103].

including any variation, during the course of S phase.[2] The model, as described in the previous chapters, allows us to draw on a number of previously derived results.

4.2.1 Summary of the *Xenopus* egg extracts replication experiment

Here, we describe recent experimental results obtained on the kinetics of DNA replication in the well-characterized *Xenopus laevis* cell-free system [44, 78]. One of the main goals of this chapter will be to show that, using the theoretical approach described previously, one can extract more information – more reliably – than before from such experiments.

In the *Xenopus* egg extracts replication experiments, fragments of DNA that have completed one cycle of replication are stretched out on a glass surface using molecular combing [23, 105, 106]. The DNA that has replicated prior to some chosen time τ_i is labeled with a single fluorescent dye, while DNA that replicated after that time is labeled with two dyes. The result is a series of samples, each of which corresponds to a different time t during S phase. Using an optical microscope, one can directly measure eye, hole, and eye-to-eye lengths at that time. We can thus monitor the evolution of genome duplication from time point to time point, as DNA synthesis advances. (See Fig. 2.1.)

Cell-free extracts of eggs from *Xenopus laevis* support the major transitions of the eukaryotic cell cycle, including complete chromosome replication under normal cell-cycle control and offers the opportunity to study the way that DNA replication is coordinated within the cell cycle. In the experiment, cell extract was added at $\tau = 2$ min, and S phase began 15 to 20 min later. DNA replication was monitored by incorporating two different fluorescent dyes into the newly synthesized DNA. The first dye was added before the cell enters S phase in order to label the entire genome. The second dye was added at successive time points $\tau_i = 25$, 29, 32, 35, 39, and 45 min, in order to label the later replicating DNA (Fig. 4.1). DNA taken from each time point was combed, and measurements were made on replicated and unreplicated regions.

The same approach has recently been adapted to study the regulatory parameters of DNA replication in HeLa cells [95]. Molecular combing, however, has the advantage that a large amount of DNA may be extended and aligned on a glass slide which ensures significantly better statistics (over several thousand measurements corresponding to several hundred genomes per coverslip). Indeed, the molecular-combing experiments provide, for the first time, easy access to the quantities of data

[2] Although $v = $ const. is a good approximation for *Xenopus* early embyos, in general, the fork velocity can vary greatly in other eukaryotes depending on the position along the genome [99, 104], and it would be interesting and important to do new experiments testing this approximation in more detail.

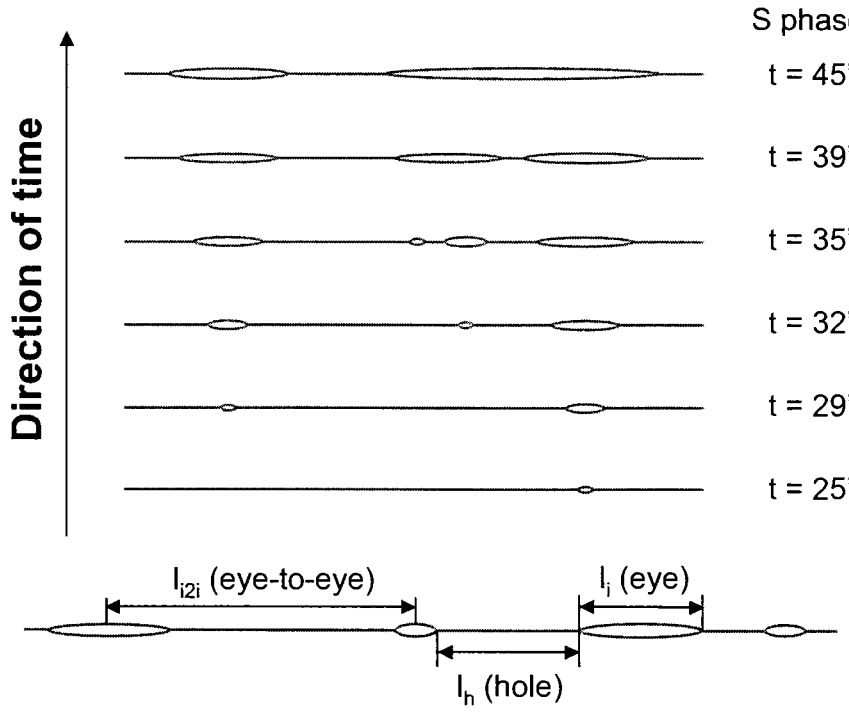

Figure 4.1: Schematic representation of labeled and combed DNA molecules. Since replication initiates at multiple dispersed sites throughout the genome, the DNA can be differentially labeled, so that each linearized molecule contains alternating subregions stained with either one or both dyes. The bubbles correspond to sequences synthesized in the presence of a single dye (red). The green segments correspond to those sequences that were synthesized after the second dye (green) was added. The result is an unambiguous distinction between eyes and holes (earlier and later replicating sequences) along the linearized molecules. Replication is assumed to have begun at the midpoints of the bubble sequences and to have proceded bidirectionally from the site where DNA synthesis was initiated. Measurements between the centers of adjacent eyes provide information about replicon sizes (eye-to-eye distances). The fraction of the molecule already replicated by a given time, $f(t)$, is determined by summing the lengths of the bubbles and dividing that by the total length of the respective molecule.

necessary for testing models such as the one advanced in this paper.

4.2.2 Generalization of the model to account for specific features of the *X. laevis* experiment

The experimental results obtained on the kinetics of DNA replication in the *in vitro* cell-free system of *Xenopus laevis* [44, 78] were analyzed using the kinetic model developed in the previous chapters. In formulating that model, we had to take into account explicitly a number of experimental limitations discussed in the previous chapter:

1) One goal of the experiment is to measure the initiation function $I(t)$, which is the probability of initiating an origin per unit length of unreplicated DNA after time interval t since the onset of replication. The simplest assumptions, in terms of our model, would be that either I is peaked at or near $t = 0$ (all origins initiated at the beginning of S phase) or $I(t) = \text{const.}$, (origins initiated at constant rate throughout S phase). However, neither assumption turns out to be consistent with the data analyzed here; thus, we formulated our model to allow for arbitrary initiation patterns and deduced an estimate for $I(t)$ directly from the data. We note that initiation is believed to occur synchronously during the first half of S phase in *Drosophila melanogaster* early embryos [79, 85]. Initiation in the myxomycete *Physarum polycephalum,* on the other hand, occurs in a very broad temporal window, suggesting that initiation occurs continuously throughout S phase [58]. Finally, recent observations suggest that, in *Xenopus laevis*, early embryos nucleation may occur with increasing frequency as DNA synthesis advances [24, 44, 78]. By choosing an appropriate form for $I(t)$, one can account for any of these scenarios. Below, we show how measured quantities may, using the model, be inverted to provide an estimate for $I(t)$.

2) The basic form of the model assumes implicitly that the DNA analyzed began replication at "laboratory time" $\tau = 0$, but this may not be so, for two reasons:

i) In the experimental protocols, the DNA analyzed comes from approximately 20,000 independently replicating nuclei. Before each genome can replicate, its nuclear membrane must form, along with, presumably, the replication factories. This process takes 15-20 minutes [107–109]. Because the exact amount of time can vary from cell to cell, the DNA analyzed at time τ_i in the laboratory may have started replicating over a relatively wide range of times.

ii) In eukaryotic organisms, origin activation may be distributed in a programmed manner throughout the length of S phase, and, as a consequence, each origin is turned on at a specific time (early and late) [110].

In the current experiment, the lack of information about the locations of the measured DNA segments along the genome means that we cannot distinguish between asynchrony due to reasons (i) or (ii). We have thus accounted for their combined effects using the starting-time distribution $\phi(\tau)$ introduced in Ch. 3, which is the probability—for whatever reason—that a given piece of analyzed DNA began replicating at time τ in the lab.

3) The combed DNA is broken down into relatively short segments (100-300 kb, typically). Also, the experiments are all analyzed using an epifluorescence microscope to visualize the fluorescent tracks of combed DNA on glass slides (with spatial resolution ≈ 0.3 μm). Thus, we have to estimate $\beta = \ell_c/\ell^*$ and $\gamma = \ell^*/\Delta x^*$ for these effects. (See Sec. 3.2.3.)

4.2.3 Application of the kinetic model to the analysis of DNA replication in *X. Laevis*

Using the generalizations discussed above, we analyzed recent results obtained on DNA replication in the *Xenopus laevis* cell-free system. DNA taken from each time point was combed, and measurements were made on replicated and unreplicated regions. Statistics from each time point were then compiled into six histograms (one for each time point) of the distribution $\rho(f, \tau_i)$ of replicated fractions f at lab time τ_i (Fig. 4.2).

One can immediately see from Fig. 4.2 the need to account for the spread in starting times. If all the segments of DNA that were analyzed had started replicating at the same time, then the distributions would have been concentrated over a very small range of f. But, as one can see in Fig. 4.2(c), some segments of DNA (within the same time point) have already finished replicating ($f = 1$) before others have even started ($f = 0$). This spread is far larger than would be expected on account of the finite length of the segments analyzed. Because of the need to account for the spread in starting times, it is simpler to begin by sorting data by the replicated fraction f of the measured segment. We thus assume that all segments with a similar fraction f are at roughly the same point in S phase, an assumption that we can check by partitioning the data into subsets and redoing our

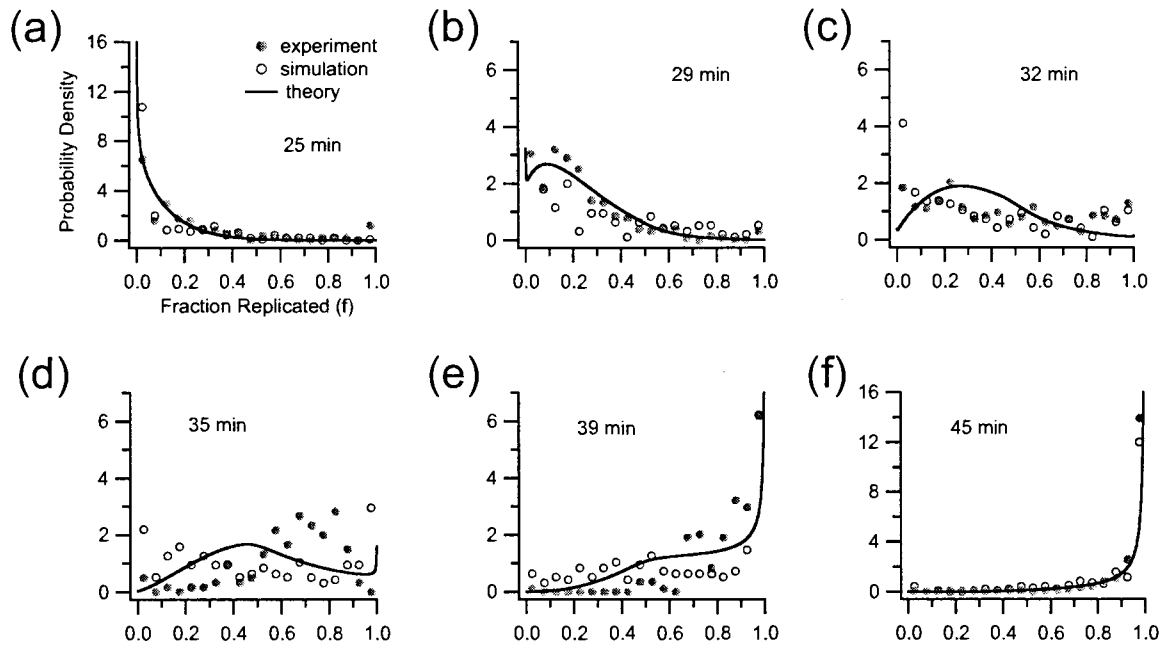

Figure 4.2: $\rho(f, \tau_i)$ distributions for the six time points. The curves show the probability that a molecule at a given time point (a)-(f) has undergone a certain amount of replication before the second dye was added. The filled circles represent the experimental data. The results of the Monte Carlo simulation are shown in open circles; analytical curves are the global fitting.

measurements on the subsets. In Fig. 4.3(a)-(c), we plot the mean values ℓ_h, ℓ_i, and ℓ_{i2i} against f.

We then find $f(t)$, $I(t)$, and the cumulative distribution of lengths between activated origins of replication, $I_{tot}(t)$. (See Fig. 4.4.) The direct inversion for $I(t)$ [Fig. 4.4(b)] shows several surprising features: First, origin activation takes place throughout S phase and with increasing probability (measured relative to the amount of unreplicated DNA), as recently inferred from a cruder analysis of data from the same system using plasmid DNA [78]. Second, about halfway through S phase, there is a marked increase in initiation rate, an observation that, if confirmed, would have biological significance. It is not known what might cause a sudden increase (break point) in initiation frequency halfway through S phase. The increase could reflect a change in chromatin structure that may occur after a given fraction of the genome has undergone replication. This in turn may increase the number of potential origins as DNA synthesis advances [111].

The smooth curves in Fig 4.3(a)-(c) are fits based on the model, using an $I(t)$ that has two linearly increasing regions, with arbitrary slopes and "break point" (three free parameters). The fits

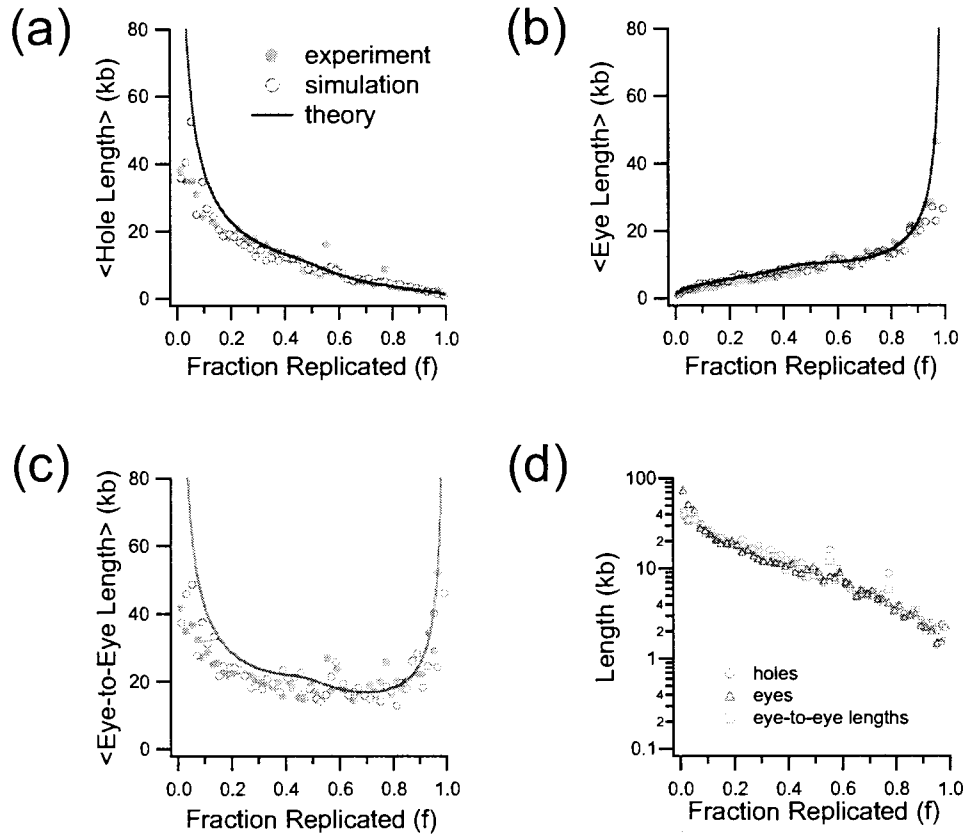

Figure 4.3: Mean quantities vs. replication fraction. (a) average hole size $\ell_h(f)$; (b) average eye size $\ell_i(f)$; (c) average eye-to-eye size $\ell_{i2i}(f)$. Filled circles are data; open circles are from the Monte Carlo simulation; the solid curve is a least-squares fit, based on a two-segment $I(t)$; (d) curves in (a)-(c) collapsed onto a single plot, confirming the mean-field relations (Eqs. 3.3a and 3.3b). (The discrepancies near $f = 0$ and 1 reflect measurement errors. Very small eyes or holes may be missed because of limited optical resolution; very large eyes or holes may be eliminated because of finite segment sizes.)

are quite good, except where the finite size of the combed DNA fragments becomes relevant. For example, when mean hole, eye, and eye-to-eye lengths exceed about 10% of the mean fragment size, larger segments in the distribution for $\ell_h(f)$, etc., are excluded and the averages are biased down. These biases due to finite sizes of the molecules also affect the last few points in the extracted $I(t)$ (see below). We confirmed this with the Monte Carlo simulations, the results of which are overlaid on the experimental data. The finite fragment size in the simulation matches that of the

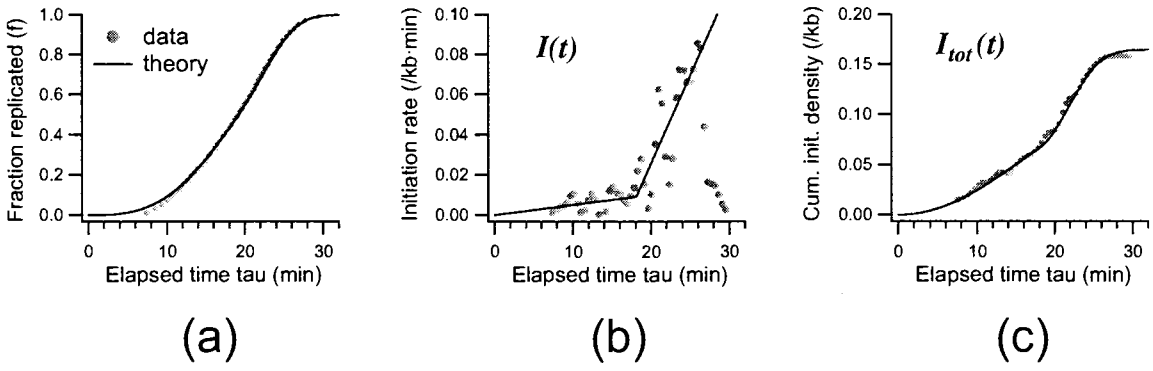

Figure 4.4: (a) Fraction of replication completed, $f(t)$. The points are derived from the measurements of mean hole, eye, and eye-to-eye lengths. The curve is an analytic fit (see below). (b) Initiation rate $I(t)$. The large statistical scatter arises because the data points are obtained by taking two numerical derivatives of the $f(t)$ points in (c). The last several points are artifacts due to finite-size effects and were not included in the analysis. (c) Integrated origin separation, $I_{tot}(t)$, which gives the average distance between all origins activated up to time t. In (a)-(c), the black curves are from fits that assume that $I(t)$ has two linear regimes of different slopes. The form we chose for $I(t)$ was the simplest analytic form consistent with the data in (b). The parameters for the least-squares fits (slopes I_1 and I_2, break point t_1) are obtained from a global fit to the eight data sets in Fig. 4.2(a)-(f) and Fig. 4.3(a)-(b), i.e., $\rho(f)$ from six time points, $\ell_h(f)$, and $\ell_i(f)$.

experiment, leading to the same downward bias. (See, also, Sec. 3.2.3) In Fig. 4.4, we overlay the fits on the experimental data. We emphasize that we obtain $I(t)$ directly from the data, with no fit parameters, apart from an overall scaling of the time axis. The analytical form is just a model that summarizes the main features of the origin-initiation rate we determine via our model, from the experimental data. We note that the last few points in Fig. 4.4(b) were excluded in the analysis for reasons explained above.[3] The important result is $I(t)$. From the maximum of $I_{tot}(t)$, we find a mean spacing between activated origins of 6.3 $\pm$ 0.3 kb, which is much smaller than the minimum

[3]To justify this, we first simulated longer molecules and then created a series of data sets by chopping the longer molecules. We observed that, as the chopped molecules become smaller, the downward bias in the extracted $I(t)$ becomes more visible and similar to the one in Fig. 4.4(b). The downward bias observed here results from a different choice of algorithm for extracting $I(t)$ than was used in Ch. 3. In that chapter, we used Eq. 3.5, while, in this chapter, we used $I(t) = -\frac{1}{2v}\frac{d^2}{dt^2}\ln[1 - f(t)]$. These two methods are identical for ideal systems, but they can lead to different biases (for example, upward and downward) in the presence of finite-size effects.

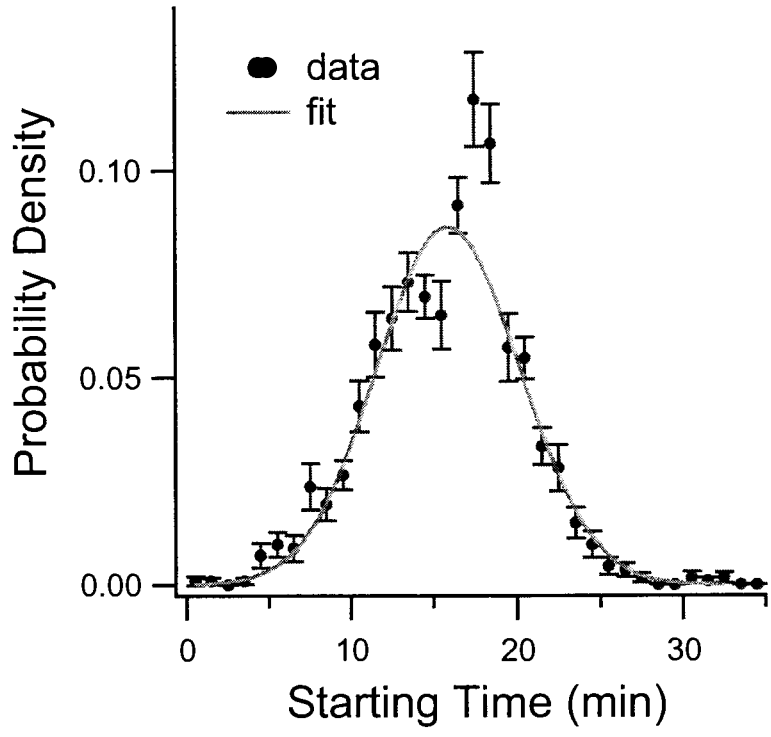

Figure 4.5: Starting-time distribution $\phi(\tau)$. Solid curve is a least-squares fit to a Gaussian distribution.

mean eye-to-eye separation 14.4 $\pm$ 1.5 kb.

In our model, the two quantities differ if initiation takes place throughout S phase, as coalescence of replicated regions leads to fewer domains, and hence fewer inferred origins.[4] The mean eye-to-eye separation is of particular interest because its inverse is just the domain density (number of active domains per length), which can be used to estimate the number of active replication forks at each moment during S phase. For example, the saturation value of I_{tot} corresponds to the maximum number (about 480,000/genome) of active origins of replication. Since there are about 400 replication foci/cell nucleus, this would indicate a partitioning of approximately 1,200 origins (or, equivalently, about 7.5 Mb) per replication focus [107, 112]. The distribution of f values in

[4]The minimum average eye-to-eye size is obtained by differentiating $\bar{\ell}_{i2i}(t) = \frac{1}{g(t)} e^{2v \int g(t') \cdot dt'}$, where $g(t) = \int_0^t I(t) dt$. For a constant initiation rate $I(t) = I_0$, one obtains $\bar{\ell}^*_{i2i} = \sqrt{2e} \cdot \sqrt{v/I_0}$. Also, we recall $\bar{\ell}_{i2i}(t) = \bar{\ell}_i(t) + \bar{\ell}_h(t) = \frac{\bar{\ell}_h(t)}{1-f}$, which allows one to collapse the experimental observations of all three mean curves onto a single one [see Eq. 3.4 and Fig. 4.3(d)].

the $\rho(f, \tau_i)$ plots can be used to deduce the starting-time distribution [$\phi(\tau)$], along with the fork velocity v (see Sec. 3.2.2). (Fig. 4.5). The spread in starting times ϕ is consistent with a Gaussian distribution, with a mean of 15.9 ± 0.6 min. and a standard deviation of 6.1 ± 0.6 min. For the fork velocity, we find $v = 615 \pm 35$ bases/min., in excellent agreement with previous estimates ~ 600 bases/min [113, 114]. As with the f data, we extracted $\phi(\tau)$ and v from a global fit to data from all six time points.

4.3 Discussion

4.3.1 Initiation throughout S phase

The view that we are led to here, of random initiation events occurring continuously during the replication of *Xenopus* sperm chromatin in egg extracts, is in striking contrast to what has until recently been the accepted view of a regular periodic organization of replication origins throughout the genome [83, 84, 115, 116]. For a discussion of experiments that raise doubts on such a view, see Berezney [104]. The application of our model to the results of Herrick *et al.* indicates that the kinetics of DNA replication in the *X. laevis in vitro* system closely resembles that of genome duplication in early embryos. Specifically, we find that the time required to duplicate the genome *in vitro* agrees well with what is observed *in vivo*. In addition, the model yields accurate values for replicon sizes and replication fork velocities that confirm previous observations [36, 113]. Though replication *in vitro* may differ biologically from what occurs *in vivo*, the results nevertheless demonstrate that the kinetics remains essentially the same. Of course, the specific finding of an increasing rate of initiation invites a biological interpretation involving a kind of autocatalysis, whereby the replication process itself leads to the release of a factor whose concentration determines the rate of initiation. This will be explored in future work.

4.3.2 Asynchrony, finite-size, and finite-resolution effects

In Ch. 3, we introduced various parameters to estimate the significance of experimental limitations in applying the kinetic model to data. In the data by Herrick *et al.* used here for analysis, all three effects – asynchrony, finite-size, finite-resolution – are present. Fortunately, we have found that the asynchrony is well-described by the Gaussian starting-time distribution $\phi(\tau)$. In this case, $\alpha = t^*/\sigma_\tau \approx 2.5$ (for the duration of S phase $t^* \approx 15$ mins. and the starting-time width σ_τ of 6.1

Effect	Parameter	Definition	when significant?	in *Xenopus* expt.
asynchrony	α	t^*/σ_τ	$\ll 1$	2.5
finite size	β	ℓ^*/ℓ_c	< 10	7-20
finite resolution	γ	$\ell^*/\Delta x^*$	< 1	10-100

Table 4.1: Summary table concerning the important parameters for experimental limitations.

mins), and the optimization method presented in Ch. 3 can be applied to the data to extract v from $\rho(f, \tau_i)$ accurately.

On the other hand, the significance of finite-size effects can be estimated by the criterion $\beta = \ell^*/\ell_c \approx 10$. In our case, ℓ^* for *Xenopus* sperm chromatin is roughly 15 kb, while the typical size of combed molecules ranges between 100 - 300 kb, thus giving $7 \lesssim \beta \lesssim 20$ and making the finite-size effects relatively insignificant. However, we note that the origin spacing of many higher eukaryotes, including *Xenopus* after the mid-blastula transition, can be as large as 100 kb. In such cases, it is of critical importance to obtain long combed molecules (> 1 Mb).

Similarly, finite-resolution effects are insignificant when $\gamma = \ell^*/\Delta x^* > 1$. This condition is satisfied in almost all molecular-combing experiments of DNA replication, since $\Delta x^* \approx 1$ kb while ℓ^* typically ranges between 10 and 100 kb ($\gamma \approx 10$ to 100).

In Table. 4.1, we present a summary showing the relative importance of these "real-world" effects.

4.3.3 Directions for future experiments in *X. laevis*

One effect that we did not include in our analysis is a variable fork velocity. For example, v might decrease as forks coalesce or as replication factor becomes limiting toward the end of S phase [107–109].

Another important question is to separate the effects of any intrinsic distribution due to early and late-replicating regions of the genome of a single cell from the extrinsic distribution caused by having many cells in the experiment. One approach would be to isolate and comb the DNA from a *single* cell. Although difficult, such an experiment is technically feasible. The latter problem could be resolved by *in situ* fluorescence observations of the chosen cell.

4.3.4 Applications to other systems

One can entertain many further applications of the basic model discussed above, which can be generalized, if need be. For example, Blumenthal *et al.* interpreted their results on replication in *Drosophila melanogaster* for $\rho_{i2i}(\ell, f)$ to imply periodically spaced origins in the genome [79]. (See their Fig. 7.) It is difficult to judge whether their peaks are real or only a statistical happenstance; but, if the conclusion is indeed that the origins in that system are arranged periodically, the kinetics model could be generalized in a straightforward way (by introducing an $I(x, \tau)$ that was periodic in x).

Very recently, detailed data on the replication of budding yeast (*Saccharomyces cerevisiae*) have become available [99]. The data provide information on the locations of origins and the timings of their initiation during S phase. These data support the view of origin initiation throughout S phase. Unlike replication in *Xenopus* prior to the mid-blastula transition, origins in budding yeast are associated with highly conserved sequence elements (autonomous replication sequence elements, or ARSs). Raghuraman *et al.* [99] also give the first estimates of the *distribution* of fork velocities during replication. Although broad, the distribution is apparently stationary, and there is no correlation between velocities and the time in S phase when the forks are initiated. The model developed here could be generalized in a straightforward way to the case of budding yeast. Knowing the sequence of the genome and hence the location of potential origins means that the initiation function would be an explicit function of position x along the genome, with peaks of varying heights at each potential origin. The advantage of the kind of modeling advanced here would be the opportunity to derive quantities such as the replication fraction as a function of time in S phase. Raghuraman *et al.* fit their data for this "timing curve" to an arbitrarily chosen sigmoidal function. (See their supplementary data, Section II-5.) Such modeling will make it easier to find meaningful biological explanations of the programming of S phase evolution.

4.3.5 The random-completion problem: part I

One outstanding issue in DNA replication in eukaryotes is the observation that the replication origins cannot be too far apart, as this would prevent the genome from being replicated completely within the length of a single S phase [117]. In the case of *Xenopus* early-embryo replications, most solutions suggested so far to prevent the formation fatal long origin spacings concern the density and the distribution of pre-replication complexes (pre-RCs) of highly conserved proteins, which

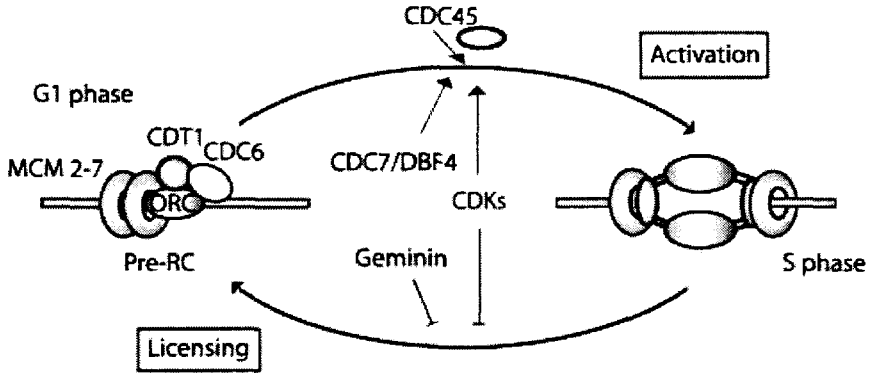

Figure 4.6: Licensing and activation of replication origins. MCM2-7 complexes, proteins that are believed to be competent to initiate replication, are loaded during late mitosis and G_1 phase onto replication origins by ORC, CDT1, and CDC6 (origin licensing). Pre-replication complexes (pre-RC) are activated at the G1/S transition by two kinases, CDC7/DBF4 and S-CDKs. A key step in this transition to replication is the recruitment of CDC45. MCM2-7 dissociate from DNA as S phase progresses. Reloading of MCM2-7 is prevented by at least two inhibitors, geminin and the CDKs. This inhibition persists until cells pass through mitosis, when geminin and cyclins are destroyed. Figure and caption from Ref. [35] by O. Hyrien. Copyright ©2003 Wiley-Liss, Inc., a subsidiary of John Wiley & Sons, Inc. Reprinted by permission of John Wiley & Sons, Inc.

assemble at ORC-bound DNA sites before the cell enters S phase (Fig. 4.6) [35].

For example, one solution that has been proposed is that there is an excess of pre-RCs (e.g., Lucas *et al.* [78], and references therein). In this case, the position of each potential origin of replication (POR) can be distributed randomly, with a statistically insignificant probability of having large gaps between PORs. The problem with this solution has been that the average POR spacing must be much smaller (less than 1-2 kb) than the reported 7-16 kb spacings of *Xenopus* ORC (XORC), protein complex that has been believed to be directly associated with PORs until recently [82, 118],

A second proposed solution to the random-completion problem is to invoke correlations in POR spacings. In other words, instead of assuming a purely random pre-RC distribution, one imposes constraints that force a partial periodicity on the POR spacing, so that most of the origins are spaced 5-15 kb apart (Blow et al. [24] and references therein). This suppresses the formation of large gaps but raises other issues. First, it requires an unknown mechanism to achieve this periodicity of POR

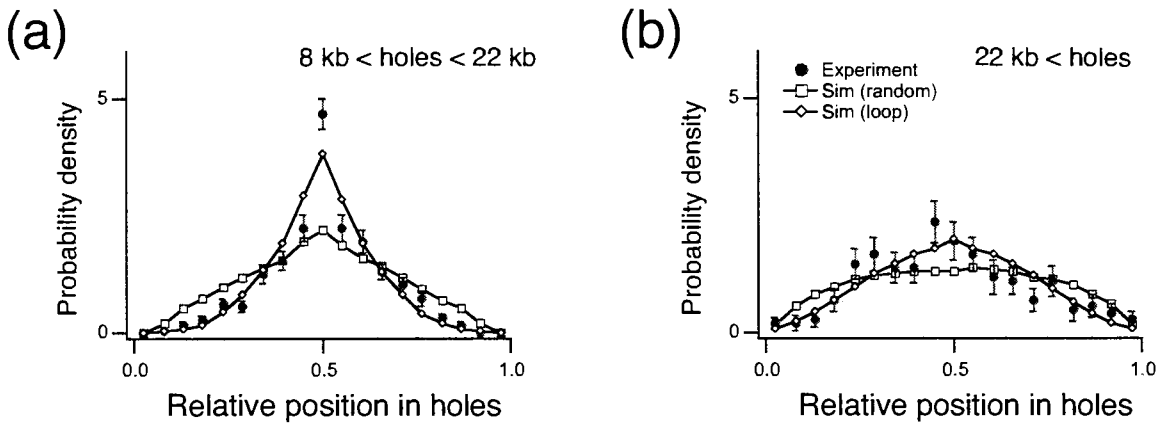

Figure 4.7: (a) Histogram of positions of initiation events for holes 8-22 kb in size. The events are determined by looking for replicated domains that are small enough that they very likely contain only a single replication origin. The state of the molecular fragment is then propagated back in time to the moment of initiation, where one records the hole size and relative position of the initiation event within the hole. The inset shows a hole flanked by two eyes. The experimental histogram shows that it is more likely that a new initiation occurs near the center of a hole, an observation compatible with the looping scenario but not with the purely random initiation scenario. (b) Holes larger than 22 kb. The difference between experiment and simulations (both random and loop formation) is much smaller than for small holes in (a).

spacing. Second, it assumes implicitly that most of the PORs fire during S phase, to prevent the 30 kb gap that could arise from a origin's failure to initiate. Blow's model is thus not robust in that the failure of a single origin to initiate could double the time needed complete replication. Third, if origins initiate throughout S phase, then there needs to be some kind of correlation that forces the more widely spaced origin groups to initiate early enough in S phase to complete replication in the required time.

Implicitly, our model adopts language consistent with the first solution, but it is straightforward to consider the correlations assumed in the second solution. The presence of significant correlations in PORs would not invalidate the results presented here, which pertain to mean quantities (e.g., Fig. 4.3); however, it would change their interpretation and could change biological models that one might try to make to explain the observed kinetic parameters we extract using the KJMA model. Indeed, the resolution of the origin-spacing problem in early embryos requires not only the temporal

$[I(t)]$ but also "spatial" program of DNA replication, and our data also suggest that initiation of replication origins is not spatially homogeneous. As an example, Fig. 4.7 shows histograms that record the relative position of new origins within a hole. In Fig. 4.7(a), we plot the distribution for small holes, 8-22 kb in length.[5] The experimental data shows a strong peak near 0.5, implying a tendency for origins to be as far away from other replicating domains as possible. By contrast, the experimental data for large holes shows a much more uniform distribution. In simulations that use spatially homogeneous initiation, new origins can appear almost anywhere in a hole, regardless of its size. This picture fits the large-hole data [Fig. 4.7(b)] but not the small-hole data [Fig. 4.7(a)]. By contrast, when we put in the effects of suppression of origin initiation by chromatin looping at very close spacings and an enhancement of initiation at a larger, characteristic distance, the simulation results match more closely the data of Fig. 4.7(a), while continuing to agree with the large-hole case.

In the next chapter (Sec. 5.3.2), we shall explain how the origin-spacing problem (or, the "random-completion" problem) can be solved by understanding the physical properties of chromatin and its looping.

4.4 Conclusion

So far, we have introduced a class of theoretical models for describing replication kinetics that is inspired by well-known models of crystal-growth kinetics. The model allows us to extract the rate of initiation of new origins, a quantity whose time dependence has not previously been measured. With remarkably few parameters, the model fits quantitatively the most detailed existing experiment on replication in *Xenopus*. It reproduces known results (for example, the fork velocity) and provides the first reliable description of the temporal organization of replication initiation in a higher eukaryote. Perhaps most important, the model can be generalized in a straightforward way to describe replication and extract relevant parameters in essentially any organism.

[5]Holes smaller than 8 kb in length showed a bias toward the center in the experimental data and were not included for comparison to models lacking such bias.

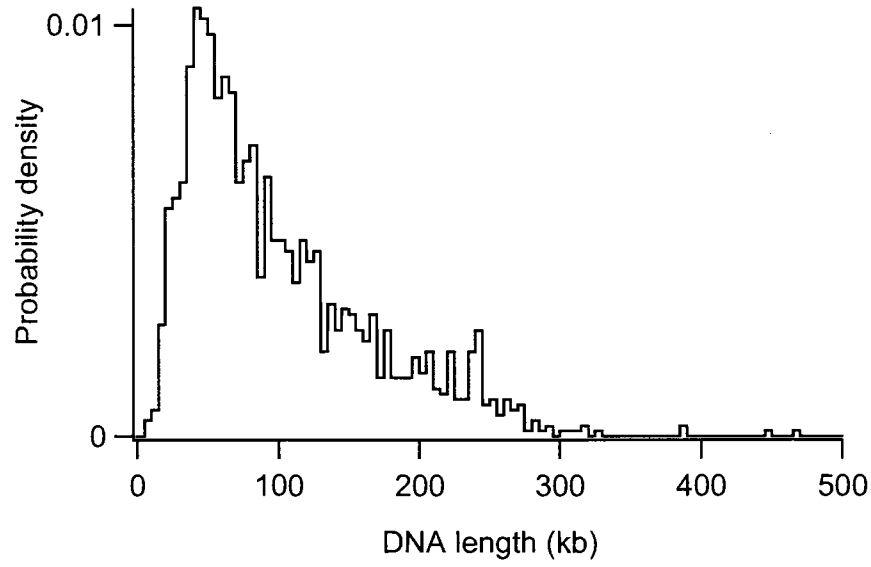

Figure 4.8: Distribution of combed DNA molecules used in the analysis: the average length was 102 kb and the standard deviation 75 kb. The distribution is approximately log normal.

4.5 Appendix

4.5.1 Monte Carlo simulations

We wrote a Monte Carlo simulation using the programming language of Igor Pro [73] to test various experimental effects that were difficult to model analytically. As we discussed in Ch. 3, these included the effects of finite sampling of DNA fragments (on average, 190 molecules per time point), the finite optical resolution of the scanned images, and – most important – the effect of the finite size of the combed DNA fragments. The size of each molecular fragment in the simulation was drawn randomly from an estimate of the actual size distribution of the experimental data (Fig. 4.8). This distribution was approximately log-normal, with an average length of 102 kb and a standard deviation of 75 kb.

We used both the lattice model and a variation of the double-list algorithm for our simulations (see Ch. 2). The timestep Δt = 0.2 min, and the lattice size $v\Delta t$ = 123 bp for the measured fork velocity v = 615 bp/min. The lattice scale is then roughly the size of origin recognition complex proteins. We sampled the simulation results at the same time points as the actual experiments (τ_i = 25, 29, 32, 35, 39, 45 minutes). Each sampled molecule is cut at random site to simulate the

combing process. The lattice is then "coarse grained" by averaging over approximately four pixels. The coarse lattice length scale is then 0.24 μm, which roughly corresponds to the resolution of the scanned optical images. Finally, the coarse-grained fragments were analyzed to compile statistics concerning replicon sizes, eye-to-eye sizes, etc. that were directly compared to experimental data.

We also used the simulation to test a previous algorithm for extracting $I(f)$, the initiation rate as a function of overall replication fraction. The previous algorithm [44, 119] looked for small replicated regions and extrapolated back to an assumed initiation time. The effects of eye coalescence is not taken into account. We tested this algorithm using our Monte Carlo analysis and, as expected, found significant bias in the inferred $I(f)$, while the algorithms we introduce here showed no such bias.

4.5.2 Parameter extraction from data and experimental limitations

We extracted data from both the real experiments and the Monte Carlo simulations by a global least-squares fit that took into account simultaneously the different data collected (i.e., the different curves in Figs. 4.2 and 4.3). As discussed above, we fit a two-segment straight line to the $I(t)$ curve extracted directly from the data for analytic simplicity. Assuming this form for $I(t)$, we derive explicit formulae for the curves in Figs. 4.2 and 4.3.

The finite size of the molecular fragments studied (102 ± 75 kb) causes systematic deviation from the "infinite-length" formulae. Such deviations could be detected using the Monte Carlo simulations by comparing the extracted values of parameters with those input. The deviations show themselves mainly in two settings: First, whenever the mean length of holes, eyes, or eye-to-eye distances approaches the mean segment length, the observed mean lengths will be systematically too small because the larger end of the experimental distributions is cut off by the finite fragment length. We dealt with this complication by restricting our fit to areas where the mean length being measured is less than 10% of the mean fragment size. The second complication is that the inferred fork velocity is systematically reduced (by about 5% for the fragment size in the experiments analyzed here). We measured this bias using the Monte Carlo simulations and then corrected the "raw" fork velocity that is given by our least-squares fits. Fortunately, these corrections are expected to be minor because the data we used satisfies the condition $\beta \gtrsim 10$. For further details, see Sec. 3.2.3.

One further subtle point in a global fit is the relative weighting to be given to the data in the $\rho(f)$ curves (Fig. 4.2) relative to the data in the mean-value curves (Fig. 4.3). We estimated the weights

using the boot-strap method [70]. The basic idea is to create M sets of data by randomly drawing data points from the original set. In other words, each created data set will consist of the same number of data points as the original one, but it now has a random fraction of the original points, typically $\sim 1/e \approx 37\%$. One then analyzes the artificial data sets as data from M independent experiments. In a similar spirit, we used repeated Monte Carlo simulations to estimate statistical errors in experimentally extracted quantities, i.e., we used our simulation to create an artificial data on which we repeated our analysis and extracted nucleation rates, fork velocities, etc. Repeating this over a number of runs (typically a few hundred), we could estimate the standard deviations in the various parameters.

Chapter 5

Spatial Program of *Xenopus* Early-Embryo DNA Replication

5.1 Introduction

In the previous chapters, we have focused on extracting the temporal program $I(t)$ of DNA replication from data. This is a "mean field" view of DNA replication, because a spatially homogeneous nucleation rate means that any site along the genome is equally capable of initiating replication and that initiation of one origin does not affect initiation of another. In real biological systems, however, knowing $I(t)$ only is not enough to describe the kinetics of DNA replication. Several extreme examples include prokaryotes such as *E. coli*, simple eukaryotes such as *S. cerevisiae*, and somatic cells. In all these, genome sequence plays an important role in defining origins of DNA replication [117]; thus, absolute position x along the genome of replication origins are pre-specified. Also, in *S. cerevisiae*, replication origins have different efficiencies, and an early-firing origin can inhibit initiation of its neighboring origins (passive replication) [101, 102].

Even for the organisms where origins are not associated with sequence, such as *Xenopus* and *Drosophila* early embryos [34, 35], potential origins cannot be distributed randomly along the genome (see the origin-spacing problem in Sec. 4.3.5). Otherwise, one expects a geometric (exponential) distribution of separations. Because the length of S phase is determined by the replication of the entire genome, even relatively rare long gaps could prolong S phase beyond its observed duration of 10-20 minutes for complete duplication of the whole genome (> 6 billion bases) [34, 36].

(a) Random-completion problem (b) Origin-redundancy model (c) Fixed-spacing model

Figure 5.1: Random-completion problem and two suggested solutions. (a) Random-completion problem: if origins are distributed randomly, their separations will follow an exponential distribution, implying large gaps that cannot be replicated in the time allotted to S phase. (b) Origin-redundancy model. (c) Fixed-spacing model.

The problem is all the more acute in that early embryo cells lack an efficient S/M checkpoint [37], which is used by many eukaryotic cells to delay entry into mitosis in the presence of unreplicated DNA. This problem is formally stated as the "random-completion problem" [116] and, for the reasons explained above, its solution requires not only a temporal program of replication but also a *spatial* program that regulates origin spacing.

Roughly, two approaches have been advanced to resolve the random-completion problem (see Fig. 5.1) [35]: In the first scenario (the "origin redundancy" model), potential origins exist in abundance and initiate stochastically throughout S phase. This allows large gaps to be "filled in" during the later stages of S phase [59, 78]. In the second scenario ("fixed spacing" model), one postulates a mechanism that imposes regularity in the distribution of potential origins, thus preventing the formation of problematic large gaps between origins [24]. In this chapter, we shall show that consideration of Herrick *et al.*'s experimental results on early embryo *Xenopus* replication leads to a more nuanced, "intermediate" view that incorporates elements of both scenarios and, more important, suggests a biological picture in which the secondary structure of chromatin – looping in particular – plays an important biological role in DNA replication.

In this chapter, we show that the molecular-combing data on DNA replication in early-embryo *Xenopus laevis* are most naturally explained by postulating that chromatin forms loops at "replication factories" [120, 121] and that these loops control origin spacing ("replication factory and loop" model; see Fig. 5.2 and also Fig. 1.6).[1] It is important to note that the size of such a loop is not

[1]The reader should not take the particular illustration of chromatin folding in Fig. 5.2 literally. In other words, we do not assume any particular (internal) structure of chromatin, i.e., our interpretation of chromatin is that it is a polymer, which has an intrinsic stiffness and, thus, there exists a specific length, where loop-formation probability is maximum (see text).

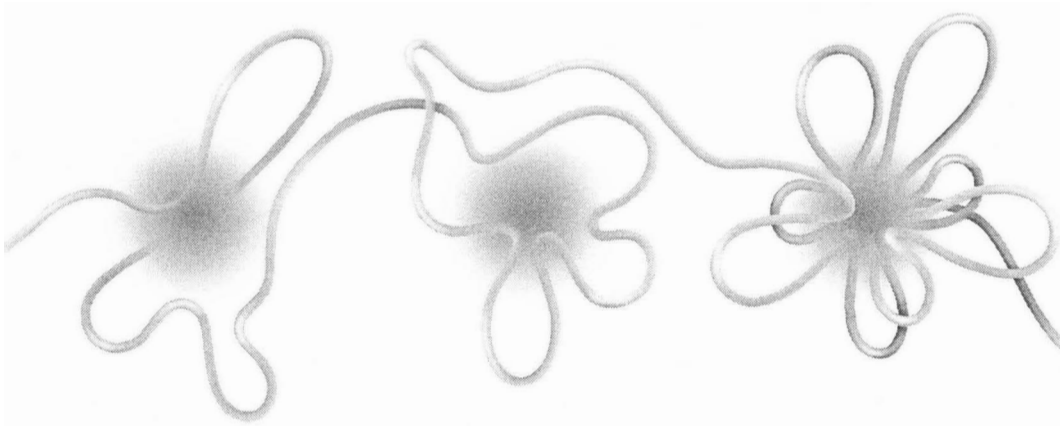

Figure 5.2: Replication factory and chromatin loops. Schematic description of how chromatin folding can lead to replication factory with loops. The loop sizes are not arbitrary (see text).

arbitrary. The stiffness of the polymer means that loops that are too small cost too much energy, while loops that are too large have too many conformations to explore for the ends to meet and, thus, cost too much entropy. Balancing these effects gives an optimal loop size, calculated correctly by Shimada and Yamakawa (SY)[2] in 1984 [122, 123], which leads to an origin-exclusion zone, since origins are connected by at least a single loop.

The sizes of the postulated loops extracted by fitting to experimental data turn out to be comparable to those obtained independently in single-molecule measurements of chromatin stiffness in other systems [124, 125]. Because the size of a polymer loop is controlled by its stiffness, we can link the physical properties of chromatin, when considered as a semiflexible polymer, to origin spacing during DNA replication. As we shall see, the physical properties of chromatin loops can explain both the observed regularity of initiation spacings [24] and the existence of an "origin-exclusion zone" [78], where origin firing is inhibited, reconciling apparently contradictory views on the nature of the mechanism that ensure rapid and complete genome replication in early embryos. Although our results concern one particular system, there is reason to suspect that they may apply more generally.

[2]Detailed physics of single-loop formation, from statics to dynamics, including the Shimada-Yamakawa distribution, will be explored in the next chapter.

5.2 Results

In Ch. 4, we drew on basic observations of DNA replication:

1. DNA is organized into a sequential series of replication units, or replicons, each of which contains a single origin of replication.
2. Each origin is activated not more than once during the cell-division cycle.
3. DNA synthesis propagates at replication forks bidirectionally from each origin.
4. DNA synthesis stops when two newly replicated regions of DNA meet.

We used these observations to construct a "kinetic model" of DNA replication based on three assumptions:

1. The initiation of origins could be described by a function $I(x,t)$ that gives the probability of initiating an origin at position x along the genome at time t during S phase.
2. Replicating domains expand symmetrically with a velocity v.
3. Replicating domains that impinge on each other coalesce.

We then used the mathematical model defined by these assumptions (cf., Ch. 2 and 3) to analyze data from the recent experiment on DNA replication by Herrick *et al.* [44]. In this experiment, cell-free early-embryo *Xenopus* was dual-labelled with two fluorescent dyes. The first was present at the beginning of the replication cycle; the second was added at a controllable time point during S phase. DNA fragments were then isolated and combed onto substrates, where they were analyzed by two-color epifluorescence microscopy. The alternating patterns of labelling then gave a "snapshot" of the state of the DNA fragment at the time the second label was added. Statistical analysis of such labels gave empirical distributions of replicated domain ("eye") lengths, "hole" sizes between replicated lengths, and "eye-to-eye" distances, defined as the distance between the center of one eye and the center of a neighboring eye. From the averages of eyes, holes, and eye-to-eye lengths, we inferred the spatially averaged initiation rate $I(t)$, the temporal program of DNA replication, which is defined as the number of new initiations per unit time per unit unreplicated length, at time t.

Although the previous analysis successfully incorporated information deduced from the averages of the various distributions (ρ_h, ρ_i, and ρ_{i2i}), we did not look at the distributions themselves. In

particular, the eye-to-eye distribution is an important quantity in that it approximates the origin-spacing distribution for small eye-to-eye distances because both eyes involved must also be small and thus likely contain just one origin each. Here, we show that analysis of these quantities including neighborhood eye-size correlations lead us to refine the assumptions made in the kinetic model, shedding light on the long-standing random-completion problem in the process.

5.2.1 The eye-to-eye distribution predicted using random initiation does not agree with experiment.

We extracted the distribution, ρ_{i2i}, of distances separating centers of neighboring eyes (eye-to-eye distances) from the raw experimental data that were also used for analysis in Ch. 4, and compared it with the ρ_{i2i} distribution obtained from a numerical simulation that assumed random distribution and activation of replication origins (data compiled from 6,300 runs of the simulation described in Appendix in Ch. 4) [Fig. 5.3(a)].

The difference between the distributions, $\Delta\rho_{i2i} = \rho_{i2i\_exp} - \rho_{i2i\_random}$, is shown in Fig. 5.3(b). Notice that there are two clearly distinct regimes. In the first regime ($\ell_{i2i} \lesssim$20 kb), the experimental data clearly differ from the simulation ($P = 4 \times 10^{-33}$; $\chi^2 = 165$ for $n = 6$ degrees of freedom). Initiations are inhibited over origin-to-origin distances smaller than 8 kb (mostly smaller than 4-5 kb). This is consistent with both the observation that there is only one origin initiation event on plasmids smaller than ~10 kb [36] and the speculation that an exclusion zone ensures a minimum origin-to-origin distance [78]. On the other hand, activation of one origin appears to stimulate the activation of neighboring origins each separated by a distance of 8-16 kb (peak at ~13 kb). This number is consistent with the previously reported origin spacings of 5-15 kb [24, 44] and the saturation density of *Xenopus* Origin Recognition Complexes (XORCs) [82, 118] along sperm chromatin in egg extracts.

The second regime ($\ell_{i2i} \gtrsim$ 20 kb) shows that for simulation and experiment the distribution of large eye-to-eye distances is statistically similar (P=0.14; χ^2=34 for n = 26), which implies that the random-initiation hypothesis holds for this regime, even as it fails at smaller origin separations.[3]

[3]The agreement between the two curves (experiment and random initiation) becomes better as the eye-to-eye distance increases. However, we note that the P-value for the two regimes (inhibition and enhancement) are most distinguishable when they are divided after the first two oscillations, i.e., at around ℓ_{i2i} = 20 kb. On the other hand, we also note that the simple random-initiation hypothesis reproduces all mean quantities such as the mean eye size throughout S phase very well, as shown in Ref. [59].

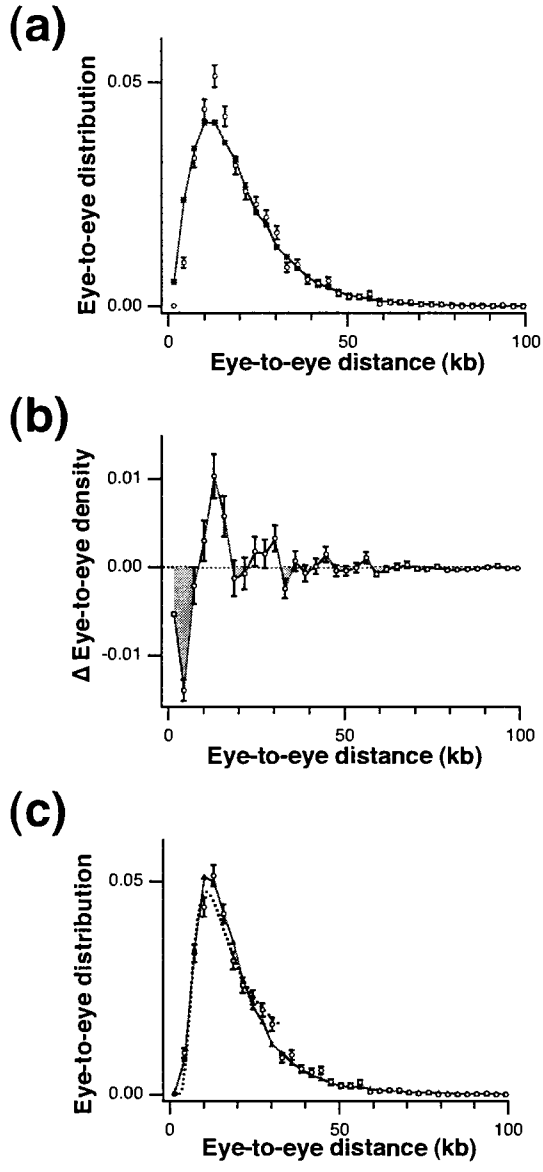

Figure 5.3: Distribution of replication origins and the loop-formation probability. Because the shape of the eye-to-eye distribution changes little during most of S phase, we pooled the experimental and simulation data for $f = 10 - 90\%$, where f is the fraction of the genome that has been replicated. (a) Eye-to-eye distribution ρ_{i2i}. (◯) Experiment; (■) Random initiation (simulation). (b) Difference between the experiment and assumed random initiations, $\Delta\rho_{i2i} = \rho_{i2i\_exp} - \rho_{i2i\_random}$. In the enhancement region (shaded blue above the zero line), more initiations occur than in the random case; in the exclusion zone (shaded red below the zero line), new initiations are inhibited. One can see that the first two oscillations ($\ell_{i2i} \leq 20$ kb) are statistically significant, while the agreement between ρ_{i2i_exp} and ρ_{i2i_random} becomes better as ℓ_{i2i} increases. (c) Experimental ρ_{i2i} and the Shimada-Yamakawa loop-formation probability. The dotted curve is a fit to the Shimada-Yamakawa approximate distribution, Eq. 6.8, over the range 0-35 kb. The fit gives $\ell_p = 3.2 \pm 0.1$ kb. The fit value of persistence length is biased downwards slightly because the SY distribution becomes inaccurate beyond a few times the persistence length [126]. The curve with triangles (▲) is the result of a simulation incorporating loops of ℓ_p = 3.2 kb, as discussed in the text.

5.2.2 Eye-size correlations and origin synchrony.

We can detect origin synchrony through correlations in the sizes of nearby replicated domains (or eye sizes). Adjacent (small) eyes of similar size will have initiated at about the same time. Thus, we tested for the presence of correlations between the sizes of nearby eyes. The correlation coefficient is defined as

$$C(|i-j|) = \frac{\langle (s_i - \langle s_i \rangle)(s_j - \langle s_j \rangle) \rangle}{\sqrt{\langle (s_i - \langle s_i \rangle)^2 \rangle \langle (s_j - \langle s_j \rangle)^2 \rangle}}, \tag{5.1}$$

where $s_i(s_j)$ is the i-th (j-th) eye size and brackets ($\langle \ldots \rangle$) denote average values. The neighborhood distance $|i-j|$ indicates how far two eyes are apart. For example, $C(1)$ is the correlation coefficient for nearest neighbors, $C(2)$ for next-nearest, and so on. Fig 5.4 shows that there is a weak but statistically significant positive correlation: larger eyes tend to have larger neighbors, and vice versa. Because domains grow at constant velocity, size correlations may be interpreted as origin synchrony. The value for the nearest-neighbor correlation, $C(1)$, is consistent with that reported by Blow *et al.* (0.16) [24].

The observation of eye-size correlations has qualitative significance in that no local initiation function $I(x,t)$ – whatever its form – can produce correlations (see Sec. 2.2.4). Intuitively, the presence of eye-size correlations means that the probability of initiating an origin is enhanced by the presence of nearby active origins and thus cannot be a function only of x and t (position along the genome and time during S phase). In Fig. 5.4, we calculate via Monte-Carlo simulation the eye-size correlations assuming that origins are placed at random along the genome (■) and intiations are independent from one another. As expected, the correlations are consistent with zero.

5.2.3 Origin spacing, loops, and replication factories.

Since the experimental eye-to-eye distribution is not consistent with the random-initiation hypothesis for short distances ($<$ 20 kb) and since eye-size correlations imply some kind of nonlocal interaction between origins, we tested an alternative hypothesis, that chromatin folding can lead to a replication factory with loops [104, 120, 121], against data. In the replication-factory-and-loop model, initiations occur at the replication factory, and there must be a correlation between the loop sizes and the distances between replication origins. As mentioned earlier, because of the intrinsic stiffness of chromatin, loops have a preferred size: activated origins will tend to occur at a characteristic separation from the replication forks of already activated replication origins.

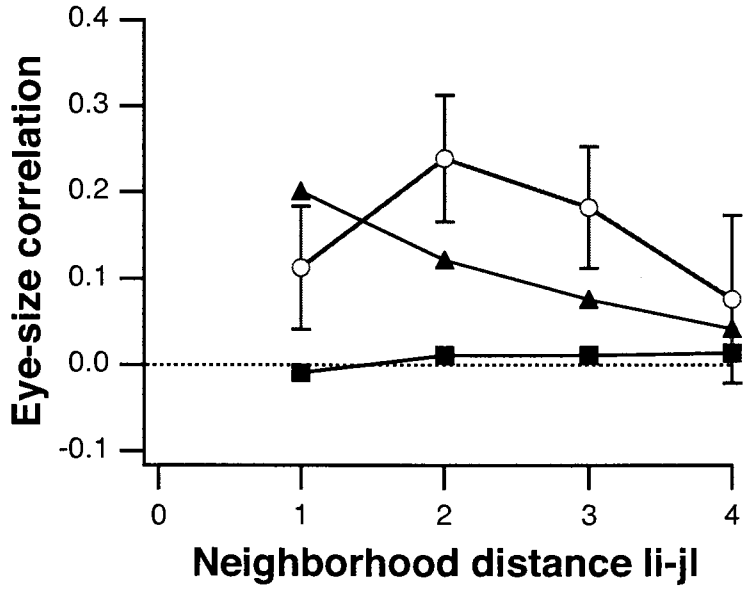

Figure 5.4: Eye-size correlation. Eye-size correlation $C|i-j|$ vs. neighborhood distance $|i-j|$ between eyes for three different cases (data for $f = 40-60\%$ pooled together): Experiment (○), random initiation (■) [59], and replication factory and loop model with loop-formation (▲) (each data set compiled from 400 runs of the simulation). The random-initiation case does not produce any correlations, as expected; however, both experiment and the replication-factory/loop-formation model produce statistically similar positive correlations.

To study the effect of adding chromatin loops to our model, we modified the Monte-Carlo simulations in Ch. 4 in a number of ways. We accounted for the size of origin proteins in pre-RC ($\sim$ 10 nm; see Fig. 4.6) by using a lattice size $\Delta x = 116$ basepairs (bp), which is fixed by setting the timestep of the simulation $\Delta t = 0.2$ minutes ($\Delta x = v \cdot \Delta t$, where the fork velocity $v = 580$ bp/min) [59]. The parameters used in the simulation, such as the number and size of combed molecules, are the same as in the experiment, which justifies a direct comparison between the two.

The simulation consists of three stages: origin "licensing," "S phase," and "molecular combing." In the licensing stage, potential origins are distributed along each molecule (or lattice site). In the random-initiation scenario, the potential-origin sites are chosen at random from the unreplicated domains of DNA. In the loop-formation scenario explored here, they are chosen in a way that depends

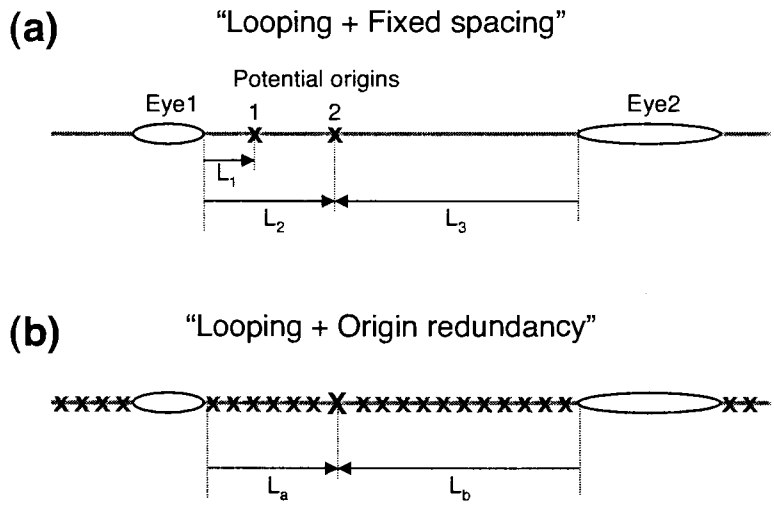

Figure 5.5: Computer simulation rules. Initiation rules for the computer simulations. (a) Looping + fixed spacing: there are two replication bubbles and two potential origins (**x**) 1 and 2. The probability of initiation of each potential origin is $p_1 = SY(L_1)$ and $p_2 = SY(L_2)$, respectively, where $SY(L)$ is the loop-formation probability (interpolated Shimada-Yamakawa distribution) of chromatin of loop-size L. (See Eq. 6.8, below.) Note that $p_2 \neq SY(L_3)$ because $L_3 > L_2$. We first calculate p's for all potential origins, and then we normalize the probabilities and initiate $\Delta N(t)$ potential origins using standard Monte Carlo procedure. (b) Looping + origin redundancy: initiation rules are the same as (a). Again, for an activated potential origin **X**, the probability of initiation is $SY(L_a)$ not $SY(L_b > L_a)$.

on the positions of the moving replication forks (see below and also Fig. 5.5).

In the S phase stage, origins fire and forks grow bidirectionally, as in previous simulations for the random-initiation scenario. In the modified simulation incorporating the replication-factory model, there are multiple chromatin loops around each factory. Each potential origin has a different probability of initiation depending on how far it is from the two left and right approaching forks. To calculate the probability of loop formation for a single loop of size L between a potential origin and the closest approaching fork, we used the following equation:

$$G_0(L/\ell_p) = (L/\ell_p)^{-\frac{3}{2}} \cdot \exp\left[-8\left(\frac{\ell_p}{L}\right)^2\right], \tag{5.2}$$

an approximation that interpolates between the SY and Gaussian-chain distributions (for details, see the next chapter). In Eq. 5.2, $G_0(L/\ell_p)\, d(L/\ell_p)$ is the relative number of loops whose scaled

contour length is between (L/ℓ_p) and $[(L + dL)/\ell_p]$. Note that the loop-formation probability is a function of the persistence length ℓ_p, which is the length scale below which (above which) a polymer can be considered stiff (flexible), and that, in the SY calculations, the distribution of loop sizes is peaked at 3-4 times ℓ_p. For the *Xenopus* chromatin, the persistence length has not been measured under the conditions applying to the present experiment. We fit the SY distribution (Eq. 6.8) to the eye-to-eye distribution to obtain an estimate of the persistence length ℓ_p [123]. We used the value from the fit (3.2 kb) in simulations incorporating the effects of loops. Then we determined how many origins to initiate, according to the experimentally determined initiation rate $I(t)$ [59]. In each time step Δt, the number of initiations is $\Delta N(t) = I(t) \cdot \Delta t \cdot L'$, where L is the length of DNA that is unreplicated at time t, and the frequency of initiation $I(t)$ is the number of initiations per unit time per unit length, averaged over the genome. Once the probability of initiation for each potential origin and the $\Delta N(t)$ are determined, the corresponding number of potential origins is chosen for initiation by standard Monte-Carlo procedure (Fig. 5.5). In our computer program, we recorded only the positions of the forks themselves, rather than the state of every lattice site; this allowed us to carry out lengthy simulations (400-6300 runs; 20-200 Mb of DNA simulated in each run) using an ordinary desktop computer. (See Sec. 2.3 for more details.)

In the final molecular-combing stage, we cut the molecules into fragments whose size distribution matches that of the actual experiment (roughly log-normal, with an average of 102 kb). We then coarse-grained the simulated molecules by averaging over a length scale of 480 bp ($\approx 0.24\ \mu m$) in order to account for the optical resolution of the experimental scanned images of combed molecules.

The final result is a simulation of the experimental data set that includes the different biological scenarios of interest, in this case chromatin loop-formation. We applied exactly the same data analysis to the simulated data set as we did to the experimental data set.

The results of our modified simulations are shown in Figs. 5.3(c) and 5.4 (data compiled from 400 runs of the simulation), which shows that incorporating the replication-factory-and-loop model into the initiation algorithm makes the ρ_{i2i} data from the simulation agree with experiment. In Fig. 5.4, the simulation data (▲) show eye-size correlations more consistent with experiment: this is an expected result since using the SY distribution as a relative initiation probability of potential origins from approaching forks implicitly enforces clustering and rough synchrony of origin firings. In Fig. 5.3(c), we plot both the SY and the measured ρ_{i2i} distributions (dotted and triangular curves, respectively). Note that the SY distribution itself should only approximate ρ_{i2i} for the following reasons: The SY distribution gives the probability that the ends of a polymer meet, while the ρ_{i2i}

distribution gives the probability that two points along the DNA meet. Unlike the SY distribution, which considers a finite segment of polymer that can form a loop only if the two ends meet, these multiple points are constrained to be discrete loci along the DNA wherever there are potential origins. In addition, if a long loop containing additional potential origins forms, multiple loops may be created by subsequent binding of one of the potential-origin sites interior to the original loop. Such possibilities are not considered in the SY distribution. Still, for small loop sizes, neither of these effects is important because the high bending-energy cost inhibits subloop formation in loops that are already small, and we may compare the SY and ρ_{i2i} distributions in this regime. The fit to the distribution result, in Fig. 5.3 (dotted curve), is reasonably consistent with the data over the fit range (0-35 kb) and gives a persistence length of 3.2 ± 0.1 kb. This persistence length was then used for the simulation data (triangles in Fig. 5.3(c) and blue points in Fig. 5.4). The optimal loop size is then $\sim$11 kb [peak of curves in Fig. 5.3(c)], and the exclusion zone is approximately one persistence length, $\sim$3-4 kb. These values are in excellent agreement with the observed average XORC saturation density, 7-16 kb along the *Xenopus* sperm chromatin in egg extracts [82, 118], the known values of origin-spacings of 5-15 kb [24, 44] and loop-sizes [115] of early embryo *Xenopus*, as well as the average origin-spacing 7.9 kb of transcriptionally quiescent *Drosophila* early embryos [79].

5.3 Discussion

5.3.1 Persistence length

The persistence length that we infer for *Xenopus* sperm chromatin fiber in egg extracts (3.2 ± 0.1 kb) is comparable to that found in other systems. Cui and Bustamante measured the persistence length of chromatin fibers under low-salt and in physiological conditions using force-extension curves obtained by stretching single chicken erythrocyte chromatin fibers [125]. They found ℓ_p = 30 nm, which corresponds to 3.5 kb for a typical packing ratio of 40 [126], slightly larger than our value. On the other hand, Dekker *et al.* [124] used their "Chromosome Conformation Capture" (3C) technique to estimate ℓ_p for chromosome III in yeast in the G1 phase of its cell cycle. They found ℓ_p = 2.5 kb, slightly smaller than our value. Although these measurements are for different systems, their similarity suggests that chromatin stiffness may typically be in this range and, also, that the looping scenario examined here may apply more generally.

5.3.2 The random-completion problem: part II

As mentioned in the Introduction and in Sec. 4.3.5, because replication origins in embryos are not linked to sequence, the relevant model of DNA replication must be able to address the random-completion problem, i.e., it must be able to account for both the observed duration of S phase and the relative infrequency of long "fluctuations" of the time to copy the genome. The two scenarios discussed above – "origin redundancy" and "fixed spacing" – have issues of concern. One problem with the origin-redundancy scenario is that, until recently, potential origins were believed to be directly associated with XORCs by assembly of pre-replication complexes (pre-RCs) consisting of several proteins (XORC, CDC6, CDT1 and MCM2-7) before the start of S phase ("origin licensing"; see also Fig. 4.6) [34, 35, 117]. The potential origins are then activated during S phase. The difficulty is that there are approximately the same number of XORCs as initiated origins. Recent data by Edwards *et al.* [127], however, suggest that all the MCM2-7 complexes, 10-40 of which are recruited by each XORC, may be competent to initiate replication and that the choice of MCM complex is not made before the start of S phase, implying that a much greater fraction of the genome serves as potential-origin sites. (More recently, Harvey and Newport [128] have shown that, indeed, replication initiation sites are coincident with MCM but not ORC, where binding of MCM complexes create an "initiation zone" of size larger than 2 kb.) Edwards *et al.* then showed that CDC45, which is essential for initiating replication at MCM complexes (Fig. 4.6), is limiting for DNA replication, and, based on this observation, they further speculated that activation of the first MCM complexes may lead to inactivation of neighboring MCM complexes, thereby restricting initiation to defined intervals. Even so, restricting initiation itself does not prevent the formation of large gaps between origins, nor does it explain the significant eye-size correlations, i.e., partial synchrony in origin firings. In other words, one still needs a structural basis for regulation of origin spacing and origin synchrony.

The problem with the other scenario (fixed spacing) is its fragility: If even one origin fails to fire, the length of S phase would increase significantly (at least of order 10 minutes for approximate XORC spacing 10 kb and fork velocity 600 bp/min) [35]. Thus, this fixed-spacing scenario requires an unknown mechanism to ensure very high efficiency of origin initiation to prevent two or more nearest-neighbor origins from failing to initiate.

The replication-factory-and-loop model considered here incorporates elements of both scenarios. Like the origin-redundancy scenario, it is based on the measured, increasing $I(t)$. But the

looping accounts naturally for the origin-exclusion zone, as well as the observation that individual origins may be more closely spaced than the typical exclusion-zone size. Like the fixed-spacing scenario, there is also regularity in the origin spacing. Note that, here, regularity appears as a natural consequence of the stiffness of chromatin, and no other mechanism is required. Both the redundant origins and the regularity contribute to making the failure to replicate the entire genome within the common duration of S phase unlikely.

In our case, we tested the replication-factory-and-loop model with various constraints on the distribution of potential-origin sites using computer simulations. The results shown here assumed an average potential-origin spacing of 7 kb, randomly distributed on a DNA molecule fragment whose length is approximately 500-1000 kb before being cut. The numbers reflect previously reported values for XORC spacings [82, 118] and the average origin spacing [24, 44]. The small size of the DNA fragments also prevents large gaps between origins, thus avoiding the random-completion problem. On the other hand, the assumption that MCM complexes completely cover the genome and all are competent for initiation also produced a result that is similar to the one presented here when looping (and the implicit synchrony rule) is incorporated in regulating initiation. At this point, the statistics available in the data of Herrick *et al.* [44] and the lack of theoretical understanding of chromatin behavior make it difficult to invert the data to draw conclusions about the form of the potential origin-site distribution. However, the wide range of potential origin distributions considered above gave results consistent with an important biological role for chromatin looping.

We emphasize that the replication-factory-and-loop model not only gives a better quantitative explanation of the ρ_{i2i} distributions, it also provides a basis for the correlations between neighboring eye sizes. Although the increase in initiation rate during S phase [44, 59, 78] can explain the observed duration of genome replication, it cannot give rise to correlations on its own. Some mechanism wherein the initiation of one origin has effects on the likelihood of nearby initiations is required. The detailed analysis of the experimental data presented here shows that inhibition near activated origins, coupled with enhancement at a characteristic farther distance, is required. We argue that loops are the simplest, most natural mechanism that can satisfy these requirements.

5.3.3 Chromatin loops and replication kinetics.

Our findings imply that higher-order chromatin structure may be tightly linked to the kinetics of DNA replication in the early-embryo *Xenopus laevis in-vitro* system. We note that looping is a well-

established way for DNA-bound proteins to interact over long distances [129]. At scales of hundreds of bases, it plays an important role in gene regulation. For example, the looping of dsDNA (ℓ_p=150 bp) with intrinsic curvature facilitates greatly the interaction between regulatory proteins at upstream elements and the promoter [130]. Loops are also known to appear in higher-order chromatin structures, such as the 30-nm fiber, at scales of thousands of bases or even longer [131]. For example, Buonguorno-Nardelli *et al.* [115] established a correlation between chromosomal loop sizes and the size of replicated domains emanating from a single replication origin (replicon). Chromatin loops are also an essential part of the replication-factory-and-loop model of DNA replication, where polymerases and their associated proteins are localized in discrete foci, with chromosomes bound to the factory complex at multiple nearby points along the genome [120, 121].

The natural follow-up to the results presented here would be to assess the generality of our results: Do they extend to other early-embryo systems? Are they valid *in vivo*? Do they apply to other transcriptionally quiescent regions of the genome?

Based on our results, we can also predict how altering chromatin structure should affect DNA replication. For example, if the replication-factory-and-loop model is correct, the loop size is roughly the origin spacing. Since the optimal loop size is proportional to ℓ_p, the duration of S phase increases with ℓ_p in a way that can be modeled quantitatively using the simulation. One experimental approach to testing these ideas would be to combine combing and single-molecule elasticity experiments (e.g., [125]) on *Xenopus*, isolating DNA from different regions of the genome. If there is heterogeneity in the stiffness of chromatin fibers in the genome, we would predict a corresponding heterogeneity in the origin-spacing distribution.

5.3.4 Loop formation and replication factories.

Currently, there are no direct experimental observations of the internal structure of replication factories. For example, the number of replicons or loops per individual factories or foci is only estimated indirectly from various quantities such as total number of origins, number of foci, fork velocities, and rough origin spacing. However, replication foci appear to be universal features of eukaryotic DNA replication and nuclear structure (e.g., Fig. 1.6). In mammalian cells, they are globally stable structures, with constant dimensions, that persist during all cell cycle stages, including mitosis (for a review see Ref. [104]). On the other hand, experimental evidence suggests that chromatin is very dynamic within individual foci at the molecular level (see, for example, Ref. [132]), consistent with

our computer simulations.

In Fig. 5.2, a schematic diagram shows how chromatin folding can lead to a replication factory with loops (see also footnote 1). Once loops form, they can dynamically fluctuate locally around factories throughout interphases, with highest mobility during the G1 phase, while the global structures of foci are stable within the nucleus. We note that recent theoretical calculations show that such chromatin folding can be very fast ($10^{-3} - 10^{-2}$ sec), and the loop-formation time is inversely proportional to the SY distribution. In other words, loop-formation is fastest when its size is 3-4 times the persistence length, and it increases exponentially as the loop size becomes smaller than the persistence length (see Ch. 6), leading us to further speculate that the origin-spacing in *Xenopus* or *Drosophila* early embryos may be selected to maximize the loop-formation and contact rate of origins.

On the other hand, the exact physical mechanisms of initiation and its partial synchrony within individual replication factory remain for future experiments. For example, although the eye-size correlation in our simulation decreases monotonically, the experimental data do not rule out the possibility of non-monotonic decay. Also, the correlations from both simulation and experiment are significant but weak. This suggests that the synchrony within a replication factory is not perfect, and nearest neighbor origins do not necessarily fire simultaneously [104].

Regardless of the biological complexity in replication foci, however, we emphasize that the loop sizes are determined by the basic physical principles explained above, namely, the balance between chromatin energy and entropy.

5.4 Conclusion

In *Xenopus* early embryos, replication origins do not require any specific DNA sequences nor is there an efficient S/M checkpoint, even though the whole genome (3 billion bases) is completely duplicated within 10-20 minutes. This leads to the random-completion problem of DNA replication in embryos, where one needs to find a mechanism that ensures complete, faithful, timely reproduction of the genome without any sequence dependence of replication origins.

The results presented here provide strong evidence that a combination of redundant origins and chromatin loops together provide such a mechanism. We find that the persistence length of chromatin loops plays a biological role in DNA replication, in that it determines the optimal distances between replication origins in *Xenopus* early embryos. Chromatin loops constitute a structural basis

for the observed distribution of replication origins in *Xenopus* early embryos, accounting for both origin exclusion zones and origin clustering along the genome. It would also be interesting to see whether the same scenario applies to other early-embryo systems such as *Drosophila.*

The picture of the replication process presented here also leads naturally to more detailed hypotheses about the role of chromatin, which should stimulate further modeling efforts.

Finally, it would be highly desirable to vary the persistence length of chromatin, to see whether the origin spacings change in a way predicted by our theory. Although such an experiment poses formidable challenges, it would be an important step forward in understanding the role of chromatin structure in DNA replication.

Chapter 6

Looping of Semiflexible Polymers: from Statics to Dynamics

6.1 Introduction

In Ch. 5, we have used the equilibrium loop-formation probability and the replication-factory-and-loop model to explain the eye-to-eye distribution during replication in *Xenopus* early embryos. One crucial assumption was that the timescale of chromatin dynamics, such as the loop-formation time τ_c, is much smaller than the typical timescale of *Xenopus* early-embryo DNA replication (10-20 minutes). Otherwise, our use of the equilibrium loop-size distribution cannot be justified. Motivated by this question of timescales, we study in this chapter a simplified version of the problem, namely, loop formation of a single chain with two "sticky" ends. As we show below, one can obtain a simple analytical expression to estimate the approximate τ_c of biopolymers using the Kramers theory and, indeed, τ_c for chromatin at the length scale relevant to DNA replication is 10^{-2} – 10^{-3} seconds, much smaller than the duration of S phase.

Indeed, polymer looping is ubiquitous in biological systems. The ability of a biopolymer to form a loop (in response to a cellular signal) is crucial for living cells to survive [38]. Polymer looping allows contact and chemical reaction between chain segments that would otherwise be too distant to interact. In gene regulation, looping allows a DNA-bound protein to interact with a distant target site on the DNA, greatly multiplying enzyme reaction rates [126, 129]. In protein folding, two distant residues start to come into contact via looping [133, 134]. On a more practical side, measurements of

loop formation in single-stranded DNA segments with complementary ends have also been used to extract elasticity information (e.g., the sequence-dependent stiffness of single-stranded DNA [135]).

Biopolymers constantly change their conformation (i.e., their shape) in response to thermal fluctuations or even weak perturbations. They are occasionally referred to as "shape-shifting" molecules [10]. Because they are flexible at large length scales, many of their global properties are well-characterized by flexible-chain models (e.g., the Gaussian chain model) [136, 137]. On the other hand, at short, biologically relevant length scales, biopolymers are stiff. Thus, one expects that a complete description of them will involve the notion of a semiflexible chain, i.e., one that is stiff below a given length scale (the "persistence length") and flexible beyond it.

Unlike flexible chains, semiflexible chains are not allowed to bend sharply, and they are locally inextensible. The origin of the local inextensibility is that the compression modulus E and the bending modulus κ of elastic rod of radius A are proportional to $Y \cdot A^2$ and $Y \cdot A^4$, respectively [138]. In other words, because of the stronger dependence of κ on the rod diameter, it is much easier to bend a thin filament than to stretch it [139]. From a mathematical point of view, this local inextensibility is very difficult to implement in analytical theories, and only a few properties of a semiflexible chain are well-understood. For example, an exact closed-form expression for the average end-to-end distance of an ideal semiflexible chain has been obtained as a function of chain stiffness, while other quantities of more practical interest such as the end-to-end distribution still elude analysis. Imposing any extra constraints, such as a fixed end-to-end distance (cf. Eq. 6.6, below), can dramatically complicate the calculations. Accordingly, a number of approximation schemes have been entertained (see [140, 141] and references therein). Chief among these are mean-field-type approximations, which amount to replacing the local inextensibility constraint by a global one. In the resulting picture, the constraint is enforced only on average. This model has been used extensively in describing both the statical and dynamical properties of a linear stiff chain [140–144].

In contrast to the case of flexible chains, much less progress has been made in describing the loop formation of a stiff chain. To date, there does not even exist a general theoretical approach to polymer loops in equilibrium that shows a crossover from the stiff- to flexible-chain limit. While the earlier work of Shimada and Yamakawa (SY) accurately describes an equilibrium ring-closure probability G_0 (the probability that the two ends meet) of a rather stiff chain, it becomes less accurate in the flexible-chain limit.

A more general treatment of G_0 by Liverpool and Edwards captures the essential physics in both the stiff and flexible limits. However, it is quantitatively inaccurate in the intermediate regime $\ell_p \simeq$

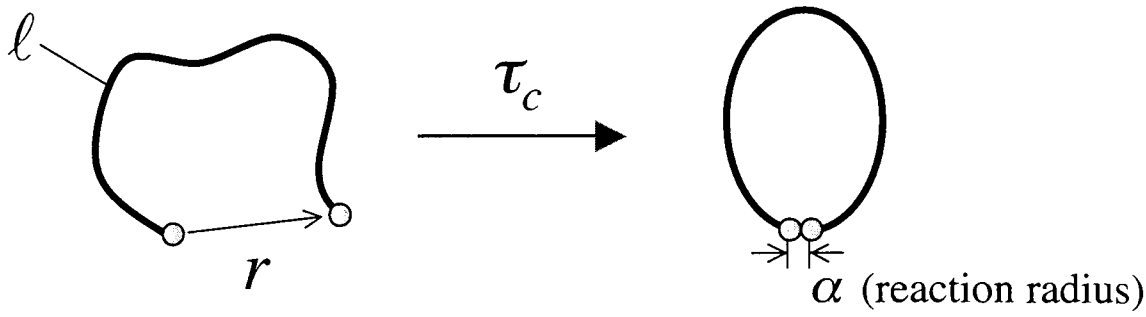

Figure 6.1: Schematic description of looping of a polymer whose reduced contour length is $\ell = L/\ell_p$ with two "sticky" ends of diameter $\alpha = a/\ell_p$, where ℓ_p is its persistence length. The end-to-end distance is $r = R/\ell_p$.

L, where G_0 does not show simple scaling behavior. Despite its relevance to biology, the looping dynamics of a stiff chain is poorly understood. Even for the simplest case of an ideally flexible polymer with no hydrodynamic effects (i.e., a Rouse chain [137]), there are two rival theoretical approaches that lead to contradictory results: Szabo, Schulten, and Schulten (SSS) conclude that the time to form a loop (the "closing time" τ_c) should scale for moderately large polymer lengths L as $\tau_{SSS} \sim L^{3/2}$ [145], while Doi, applying Wilemski-Fixmann (WF) theory [146, 147], finds $\tau_{Doi} \sim L^2$ [148]. The discrepancy between the two continues to spur debate [149, 150]. For the important case of stiff chains [151, 152], where the polymer length L is comparable to or smaller than the persistence length ℓ_p, extensive theoretical and numerical studies have only recently been carried out [153–156]. The main difficulty arises from the interplay between two seemingly distinct processes: chain relaxation and chain closure. This interplay is unique to a polymeric system and originates from the chain connectivity of a polymer immersed in a noisy environment.

In this chapter, we present simple theoretical models that describe the looping of a semiflexible chain. One major simplification is that we consider a finite segment of polymer with two "sticky" ends (Fig. 6.1), as oppose to the biologically more relevant case of infinitely long chains that are sticky everywhere (chromatin fibers can bond to replication factories at any point, as illustrated in Fig. 5.2). Also, we limit our discussion to ideal chains, i.e., those in a theta solvent, for which there is no excluded volume interaction between chain segments. We shall argue that, despite these simplifications, our calculations capture the basic physics of the looping.

In our calculations, we show how the equilibrium properties of a stiff chain are reflected in its looping dynamics. To this end, we compare the time scales of chain relaxation and chain closing.

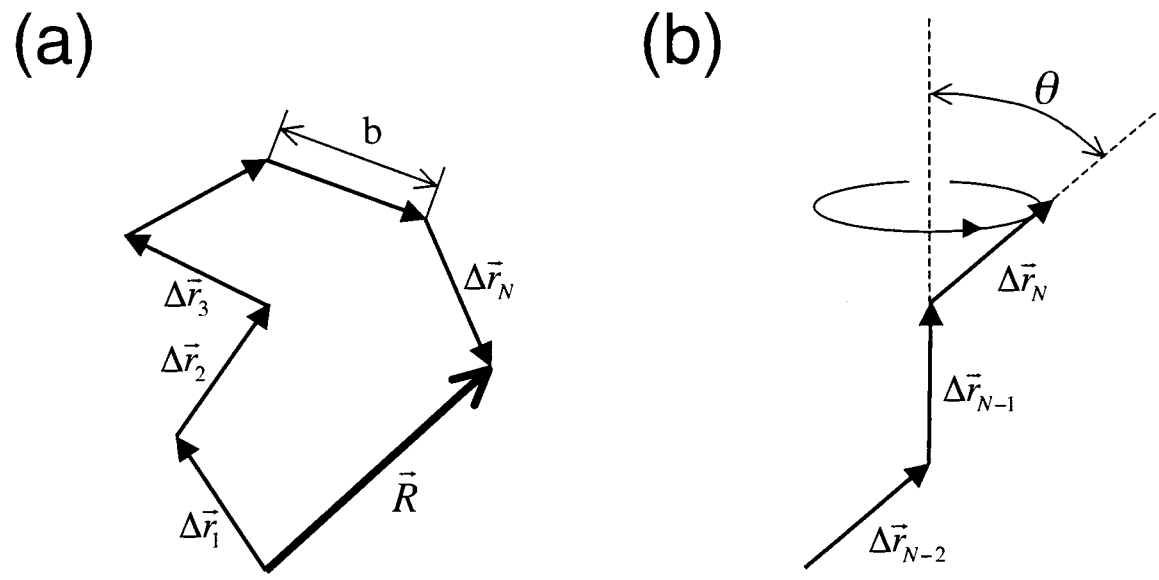

Figure 6.2: Discrete models of polymer. (a) Freely Jointed Chain (FJC) (b) Freely rotating chain.

For stiff chains, the closing time τ_c is typically much longer than the global chain-relaxation time τ_R. In this case, a Kramers rate theory [157, 158], to be developed below, leads to analytical approximations for τ_c. The main factor governing the looping in this regime turns out to be the equilibrium ring-closure probability. An important result is that, if one considers the loop-formation time for polymer chains of different lengths L, then there is a minimum for $L \approx 3 - 4\ell_p$. Roughly speaking, looping of shorter chains require too much energy relative to the thermal energy k_BT, while longer chains need to search too many conformations for ends to "find" each other. We also show that consideration of the requirements for Kramers theory to apply leads one naturally to identify different regimes governing the closing time τ_c. This classification shows how the physics of chain relaxation is intertwined with that of chain closing and clarifies the above-mentioned controversy between the SSS and Doi approaches to loop-formation dynamics. We also discuss briefly some biological implications of our results.

6.2 Theoretical Approaches to Modeling Polymers

We first review the overall classification of polymer models, both discrete and continuous. The simplest discrete polymer model is the freely jointed chain (FJC). Fig. 6.2(a) shows a model FJC as a chain of freely joined vectors of fixed length b. The FJC ignores both monomer interactions and finite chain stiffness and can be thought of as a random walk of a fixed step length, where each step is independent of the previous trajectory. Usually, the "size" of a polymer chains is defined as $\sqrt{\vec{R}^2}$, and one can derive a very simple scaling law $\sqrt{\vec{R}^2} \propto N^{1/2}$ from

$$\langle \vec{R}^2 \rangle = \left\langle \sum_i \Delta\vec{r}_i \cdot \sum_j \Delta\vec{r}_j \right\rangle = \sum_i \langle \Delta\vec{r}_i^2 \rangle + \left\langle \sum_{i \neq j} \Delta\vec{r}_i \cdot \Delta\vec{r}_j \right\rangle = N\, b^2. \tag{6.1}$$

When $N \rightarrow \infty$, the distribution of end-to-end vectors $\vec{R}$ is Gaussian. In a variant of the FJC, beads are separated by freely jointed linear springs, which leads to a Gaussian distribution of bond lengths. For large N, the distinction between the FJC and this "Gaussian-chain" model disappears.

A more realistic discrete model polymer, the freely rotating chain (FRC), is shown in Fig 6.2(b). The FRC consists of vectors with fixed bond angle but with completely free dihedral angles, thus naturally incorporating finite stiffness. In the FRC, $\langle \vec{R}^2 \rangle$ can be calculated exactly in a straightforward way, and it is easy to show that the FRC also follows the same scaling law in N as the FJC. Next, we define a quantity called the "persistence length" as

$$\ell_p \equiv \lim_{N \rightarrow \infty} \langle \vec{R} \cdot \Delta\vec{r}_0 \rangle = \frac{b}{1 - \cos\theta}, \tag{6.2}$$

which is the average length of the projection of the end-to-end vector along the direction of the first bond vector. As we shall show below, the persistence length is a measure of chain stiffness.

The continuum limit of the FRC is the Kratky-Porod (KP) wormlike chain [159]. We define the total contour length $L = N \cdot b$ and the contour distance s $(0 \leq s \leq L)$ from the zero'th to the i'th vector by $s = i \cdot b$. We then take the limit, $N \rightarrow \infty$, $b \rightarrow 0$, and $\theta \rightarrow 0$, with constraints that the chain length L and the persistence length ℓ_p remain constant. The discrete chain contour then becomes a continuous, differentiable space curve. The statistical properties of the KP wormlike chain are then determined by an effective free energy quadratic in the curvature $\partial\vec{u}(s)/\partial s$:

$$\mathcal{H}_b = \frac{\kappa}{2} \int_0^L \left[\frac{\partial\vec{u}(s)}{\partial s} \right]^2 ds \quad \text{with} \quad |\vec{u}(s)| = 1, \tag{6.3}$$

where $\kappa \equiv \ell_p \cdot k_B T$ is the bending modulus of the polymer, and the unit tangent vector $\vec{u}(t)$ at s on the curve is defined as $\vec{u}(t) = \frac{d\vec{r}(s)}{ds}$, with $\vec{r}(s)$ is the position vector. As we discussed above,

imposing the constraint of fixed polymer length, $|\vec{u}(s)| = 1$, is one of the major difficulties in handling the model analytically [140, 160].

Several quantities, nonetheless, are known exactly. One of the most important is the spatial correlation function for unit tangent vectors [137],

$$\langle \vec{u}(s) \cdot \vec{u}(s') \rangle = \exp\left(-\frac{|s - s'|}{\ell_p} \right). \tag{6.4}$$

Using Eq. 6.4, we can also calculate $\langle \vec{R}^2 \rangle$ exactly,

$$\langle \vec{R}^2 \rangle = \int_0^L \int_0^L \langle \vec{u}(s) \cdot \vec{u}(s') \rangle \, ds \, ds' = 2\ell_p L - 2\ell_p^2 \left(1 - e^{-L/\ell_p} \right). \tag{6.5}$$

Eq. 6.5 implies, for $L \ll \ell_p$, $\langle \vec{R}^2 \rangle = L^2$: the rod is rigid. For $L \gg \ell_p$, we have $\langle \vec{R}^2 \rangle = 2\ell_p L$, which is identical to Eq. 6.1, if we identify $b' = 2\ell_p$ and $N' = L/b'$ as effective segment lengths and polymerization indices, respectively. The behavior in these two limits shows that the KP wormlike chain interpolates between the rigid rod and the Gaussian chain. Hence, the persistence length ℓ_p is a measure of the chain stiffness in the KP model. One often uses a dimensionless chain length, $\ell = L/\ell_p$. We note that neither the KP nor the lattice models considers the torsional energy of a chain, which can lead to complications such as supercoiling and knotting [161]. The helical wormlike (HW) chain model has both bending and torsional energies, and it has been very successful in applications involving short lengths of DNA. Formally, the HW chain is obtained from a discrete chain with coupled rotations (the dihedral-angle distributions are non-uniform) [122].

A quantity of particular interest is the end-to-end distribution function defined as an ensemble average of $\delta(\vec{R} - \int_0^L \vec{u}(s)ds)$:

$$G(\vec{R}; L) = \left\langle \delta\left(\vec{R} - \int_0^L \vec{u}(s) ds \right) \right\rangle. \tag{6.6}$$

Unfortunately, the constraint $|\vec{u}(s)| = 1$ makes this integral intractable. One way to tackle this difficulty is to impose the hard delta-function constraint only on average. Using this "mean field" approach, Thirumalai and Ha (TH) [140] have obtained an approximate form for $G(r, \ell)$ in terms of the reduced parameters $r = R/\ell_p$ and $\ell = L/\ell_p$, as follows:

$$G(\vec{r}, \ell) = n(\ell) \cdot \left[1 - \left(\frac{r}{\ell} \right)^2 \right]^{-\frac{9}{2}} \times \exp\left\{ -\frac{3\ell}{4} \frac{1}{[1 - (r/\ell)^2]} \right\}, \tag{6.7}$$

where the normalization factor $n(\ell)$ is fixed by requiring $\int_0^\ell 4\pi r^2 G(r, \ell) dr = 1$. (The other end of a polymer of length ℓ must be located within a sphere of radius ℓ of the first end.) Note that a more

accurate but more complicated expression recently derived by Winkler [141] gives essentially the same results. The expression for G in Eq. 6.7 becomes exact as $\ell \to \infty$ but is less accurate for ℓ_p comparable to L (i.e., $\ell \simeq 1$). Although it underestimates the energy cost for tight bending, it is accurate to 10%.

Using $G(r, \ell)$, we define the ring-closure probability to be $G(\vec{r} = \mathbf{0}, \ell) \equiv G_0(\ell)$. As we shall discuss below, G_0 measures the difficulty in bringing the two chain ends close to each other. It will turn out to be a key quantity in the description of loop-formation dynamics. Note that both $G(r, \ell)$ and $G_0(\ell)$ include no constraints on the orientation of the end-point target vectors. In particular, $G_0(\ell)$ includes "kinked" loops with an orientation discontinuity between the two ends.

For flexible chains, the ring-closure probability $G_0(\ell)$ is analogous to the probability for a random walk to return to the origin and is given by $G_0(\ell) \sim \ell^{-3/2}$ [122]. We can understand this scaling, as follows: In this limit, the mean end-to-end distance r_g for an ideal flexible chain scales as $r_g \sim \ell^{1/2}$. The volume occupied by the chain is then given by $V \sim {r_g}^3 \sim \ell^{3/2}$. The probability to find the two ends at $R = 0$ is inversely proportional to V, leading to $G_0(\ell) \sim \ell^{-3/2}$.

For stiff chains ($\ell \lesssim 1$), the first theoretical result for $G_0(\ell)$ was obtained by Shimada and Yamakawa (SY) about twenty years ago [123]. The basic idea is to start from a ground-state conformation of a polymer ring and to consider small conformational fluctuations around it. This leads to

$$G_0^{SY}(\ell) = \left(\frac{896.32}{\ell^5}\right) \exp\left(-\frac{14.054}{\ell} + 0.246\,\ell\right). \tag{6.8}$$

Note that the $1/\ell$-term in the exponent in Eq. 6.8 solely arises from the bending energy, while the other terms come from chain fluctuations about the lowest-energy conformation. In other words, the leading term in the exponent ($\sim 1/\ell$) is the minimum bending energy of a stiff rod whose two ends are glued together without restricting the orientation of the tangents. The preferred angle between the tangents for minimum bending energy is called the Yamakawa-Stockmayer angle [162] and is roughly 82°. This explains why the leading term is slightly smaller than the bending energy of a circular polymer circumference L, which is $E_{\rm loop}/k_BT \approx \frac{1}{2}\ell_p L(2\pi/L)^2 \approx 19.7/\ell$ (Eq. 6.3).

It is worth noting that the expression derived by SY does not cross over to the result for a flexible chain, $G_0(\ell) = \ell^{-3/2}$. The reason is that, in the flexible limit, fluctuations about the ground state become too large to be treated as a perturbation.

Ringrose *et al.* [163] have given an *ad hoc* expression for $G_0(\ell)$ that is accurate over the entire

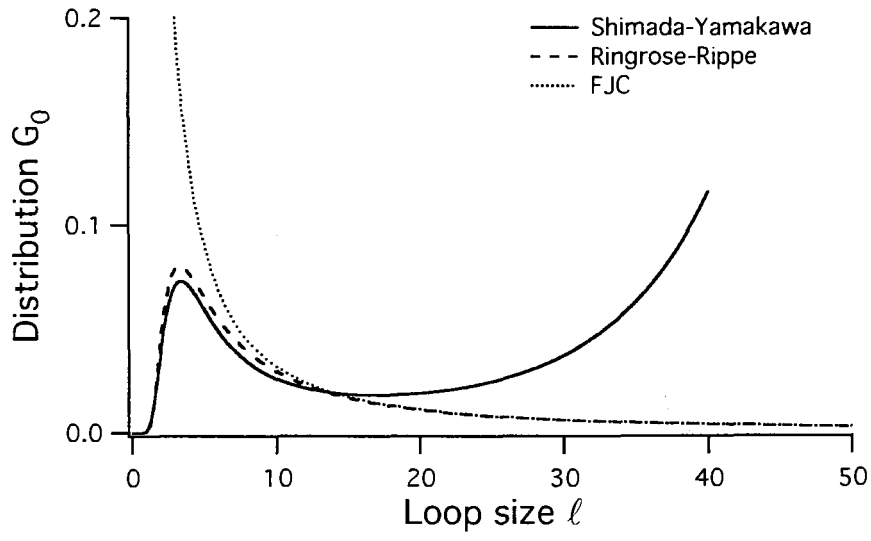

Figure 6.3: Loop-size distribution for three cases: Shimada-Yamakawa (Eq. 6.8), Ringrose-Rippe (Eq. 6.9), and Freely Jointed Chain (FJC).

range of ℓ:

$$G_0^R(\ell) = \ell^{-\frac{3}{2}} \cdot \exp\Big(-\frac{8}{\ell^2}\Big). \tag{6.9}$$

No matter which approximation we use, $G_0(\ell)$ should vary non-monotonically: For small ℓ (or $L \lesssim \ell_p$), chain closing (in equilibrium) is energetically discouraged and hence exponentially suppressed, as implied by Eq. 6.8. On the other hand, equilibrium looping is mainly determined by the chain entropy in the flexible chain limit $\ell \gg 1$ (Fig. 6.3).

6.3 Relaxation of a Stiff Chain

The previous section concerned equilibrium chain statistics. Here, we describe the process of chain equilibration, i.e., the way a chain configurations approach equilibrium as time elapses. To this end, we will invoke a simplification that is only qualitatively valid but, nevertheless, provides much of the information we need to proceed with our discussion about the looping dynamics.

The dynamics of each monomer depends on and is complicated by other monomers in the same chain. In what follows, we shall focus on the strong-damping (high-friction) limit, as it is the relevant case for biomolecules in viscous media (e.g., water). The essential assumption is that the

velocity of each monomer $d\vec{r}(s,t)/dt$ equilibrates much faster than does its position. To quantify this statement, let us consider two time scales for a monomer: a velocity-relaxation time (τ_v) and a diffusion time scale over its own size b (τ_D). A particle of mass m and friction constant ζ (defined by $m\frac{dv}{dt} = -\zeta v$) in a viscous medium moves like a free particle for the time scale $t \ll \tau_v = m/\zeta$; for $t \gg \tau_v$, however, its motion becomes diffusive. The high-damping limit pertains as long as $\tau_v \ll \tau_D \approx b^2/D_0$ or $\zeta \gg \sqrt{mk_BT/b^2}$, where $D_0 = k_BT/\zeta$ is the diffusion constant of each monomer. If we assume a spherical monomer of radius b and mass density ρ is immersed in a solvent of viscosity η_s, then $\zeta = 6\pi\eta_s b$ and $m = 4\pi b^3\rho/3$. For a typical biopolymer, we find that $\tau_D \gg \tau_v$ by several orders of magnitude. In this high-damping limit, the inertia term can thus be dropped.

For the corresponding flexible case, the polymer dynamics can be expressed as the sum over a number of independently moving modes, known as Rouse modes [136, 137]. The local inextensibility constraint of $|\vec{u}(s)| = 1$, however, complicates the analysis because it couples the normal modes to each other. To circumvent this difficulty, we consider a global chain deformation near the rod limit. The characteristic time scale for this deformation is essentially the global relaxation time τ_R (or chain equilibration time), as the higher-order modes will relax faster than this deformation. The time scale obtained this way is a reasonable estimate of the relaxation time for the slowest mode, i.e., τ_R. Now the physics near the rod limit is dominated by the bending energy E_b of the chain [164]. Since the lowest energy of bending a linear stiff chain is well-approximated in terms of a uniform curvature of radius $\mathcal{R}$, the bending energy in this case is $E_b/k_BT = \frac{1}{2}\ell_p L/\mathcal{R}^2 \simeq 2\ell_p(L-R)/L^2$. The relative position $\vec{R}$ of the two ends of the chain (experiencing a uniform deformation) behaves like a particle subject to a constant restoring force $f_c = 2k_BT\ell_p/L^2$. Inspired by the dumbbell model for flexible chains introduced by Kuhn and Péterlin (see Ch. 6 in Ref. [136] and references therein), which pictures the whole chain as a spring subject to (entropic) elastic force, we can write a similar equation for a stiff chain

$$\zeta_{\rm tot}\dot{\vec{R}} = -f_c\frac{\vec{R}}{R}, \tag{6.10}$$

where $\zeta_{\rm tot}$ is a friction constant (see below). From dimensional analysis, Eq. 6.10 leads to a scaling relation for the characteristic time for stiff-chain deformation ($\sim L$):

$$\tau \sim \frac{\zeta_{\rm tot}}{f_c}L \sim \frac{\zeta_{\rm tot}}{k_BT}\frac{L^3}{\ell_p}. \tag{6.11}$$

If we choose $\zeta_{\rm tot} \sim N = L/b$ (additivity of friction for individual monomers), we get $\tau \sim \frac{\zeta_0}{k_BT}\frac{L^4}{b\ell_p} = \frac{1}{D_0}\frac{L^4}{b\ell_p}$, where ζ_0 and D_0 are friction and diffusion constants for individual monomers,

respectively. Note that this has the same scaling as the relaxation times of a stiff chain (e.g., [165]), which is not surprising, since Eq. 6.10 only concerns the total elongation $\vec{R}$. Also, note that τ decreases as ℓ_p increases, because $\vec{R}$ feels a stronger restoring force for larger ℓ_p, relaxing faster. In principle, hydrodynamic effects can be included in the analysis; however, they only have a marginal effect on the longest relaxation time τ_R in the stiff limit. That is, τ_R is roughly proportional to $\ln N$ (namely, logarithmic corrections [137, 166]). Although this result is valid only as long as $L \lesssim \ell_p$, it clearly suggests that stiff chains equilibrate more efficiently than flexible chains, where $\tau_R \sim L^2/D_0$. In other words, the dynamics of a stiffer chain is less complicated by internal modes (degrees of freedom other than the global chain deformation).

6.4 Looping Dynamics

In this section, we will introduce a simple theoretical model for describing the looping dynamics of a stiff chain. To be specific, we consider a linear chain with two sticky ends, which become reactive when they are sufficiently close to each other. Clearly, the looping dynamics is controlled by two distinct rates: the rate at which two ends are brought close and the rate at which the two ends react. In the diffusion-limited case, which we mainly focus on, the reaction rate between the two ends is arbitrarily large: It is assumed that the chain forms a loop as soon as the two ends fall within a reaction radius a. This amounts to imposing an absorbing boundary condition on the (possibly time-dependent) distribution function of R. The closing time obtained this way is a first-passage time and, hence, only a lower bound for closing times in more realistic cases. Our discussion in the previous section implies that polymer dynamics is in general complicated by the presence of internal modes. As it turns out, the looping dynamics of a polymer is even trickier to formulate. The main difficulty arises from the absorbing boundary condition, which is hard to implement and which causes the Rouse modes for an ideal flexible chains to become coupled to each other, making the looping problem intractable without approximations.

Our discussion in the previous section implies that the effective potential felt by the two ends of a chain depends on how the chain relaxes. In other words, the looping dynamics can be influenced by chain relaxation. Similarly, chain relaxation can also be influenced by chain looping. If a is sufficiently large, then the chain closes before it relaxes. In other words, the processes of relaxation and looping are intertwined. However, for a sufficiently stiff chain, the closing time τ_c can be much longer than τ_R, a fact that can be tested *a posteriori*. In this case, we can ignore internal

modes and project the looping dynamics onto the one-dimensional reaction coordinate R. Consider a chain of reduced length $\ell \equiv L/\ell_p$ and end-to-end distance $r \equiv R/\ell_p$ with two ends that react when first brought within a distance a of each other ("diffusion-limited" loop-formation dynamics) (Fig. 6.1). We apply Kramers rate theory [157], viewing the process as a noise-assisted crossing over a potential barrier. In this picture, r is the only dynamic variable; even though the chain has already relaxed, the two sticky ends in the diffusion limited case are not allowed to equilibrate in the potential they create. In this regard, the combined system of the chain and the two sticky ends is said to be in "local equilibrium." After first presenting the straightforward calculation, we then consider carefully its domain of applicability and give a scaling description of loop formation outside this domain.

The basic idea is to project the internal degrees of freedom of the polymer chain onto a single "reaction coordinate" r and to use the equilibrium distribution function $G(r,\ell)$ to construct an approximate "effective potential" between the two ends

$$U(r,\ell) = -k_B T \ln P(r,\ell), \tag{6.12}$$

where $P(r,\ell) \equiv 4\pi r^2 G(r,\ell)$ is the radial distribution function of reduced end-to-end distances r of a polymer of length ℓ and $G(r,\ell) \equiv G(|\vec{r}_\ell - \vec{r}_0|;\ell)$, the angle-averaged distribution function for the end-to-end vector $\vec{r} = \vec{r}_\ell - \vec{r}_0$. (For justification of Eq. 6.12, see, for example, [141].) Here we assume isotropic chemical interactions between end monomers, so that end binding can be modeled by adding to U a smooth short-range potential $f(r/\alpha)$, with $\alpha \equiv a/\ell_p$ the scaled interaction range. Generalization to an anisotropic case is straightforward, but we consider only the isotropic case for simplicity. A typical distribution function and the resulting effective potentials are shown in Fig. 6.4. Then, in our "single-variable picture," we postulate that the long-time ($t \gg \tau_R$) dynamics are governed by the effective potential $U(r,\ell)$ and that they obey a Fokker-Planck equation for the time evolution of the distribution of r:

$$\frac{\partial P(r,\ell,t)}{\partial t} = D_{\text{eff}} \frac{\partial}{\partial r}\left[\frac{P}{k_B T}\,\partial_r U + \frac{\partial P}{\partial r}\right], \tag{6.13}$$

where D_{eff} is the effective diffusion constant for dynamics.

Because polymers – whatever their stiffness – have a most probable end-to-end separation, there is a local minimum in the effective potential at $r = r_b$ (bottom), which is $\sim \ell$ in the stiff-chain limit and $\sim \ell^{\frac{1}{2}}$ in the flexible-chain limit, neglecting self-avoidance effects. Also notice in Fig. 6.4 the barrier to chain closing at $r = r_t \approx \alpha$ (top), which is created by the balance of chain entropy

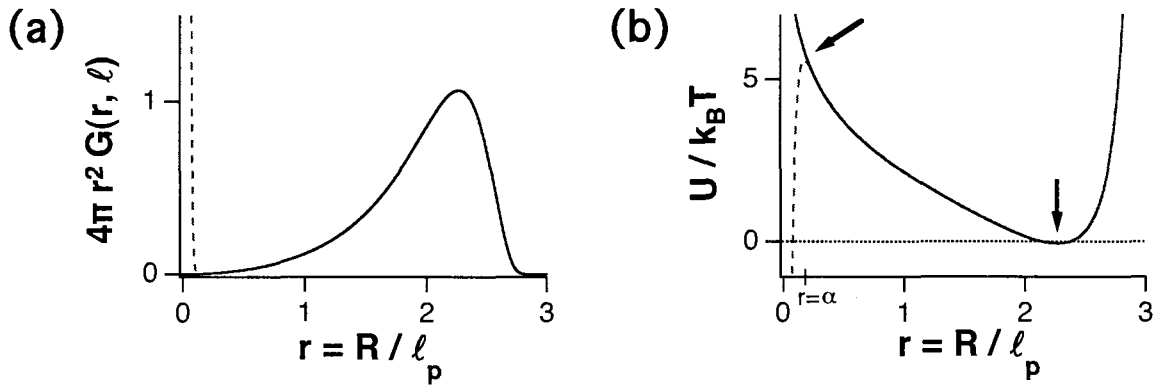

Figure 6.4: (a) The radial distribution density $P(r, \ell = 3)$. The dashed line shows the effect of a short-range interaction between the two polymer ends. (b) The resulting effective potential of the chain. Arrows denote the top and bottom of the effective potential well, as used in the Kramers calculation.

and bending energy, as implied by $U(r, \ell)$. The short-range attractive potential then rounds off the barrier.[1] The resulting effective potential has thus the qualitative form often assumed in Kramers-rate calculations.

In the limit of strong damping, the time needed to cross over the barrier (mean first-passage time), calculated using Kramers rate theory, is

$$\tau_{Kr} \approx \frac{1}{D_{\text{eff}}} \int_{r_b}^{r_t} dy\, e^{\frac{U(y)}{k_B T}} \int_{-\infty}^{r_b} dz\, e^{-\frac{U(z)}{k_B T}} \quad (\Delta U \gg k_B T), \tag{6.14}$$

where ΔU is the barrier height (Appedix 6.5). In the presence of the "capture force," the barrier top becomes smooth, and the above equation can be further simplified as

$$\tau_{Kr} = \frac{2\pi\zeta_{\text{eff}}}{\omega_t \omega_b} \exp\left(\frac{\Delta U}{k_B T}\right), \tag{6.15}$$

where the effective friction constant $\zeta_{\text{eff}} = \frac{k_B T}{D_{\text{eff}}}$ and the well curvatures $\omega(r) = \frac{1}{\ell_p}\sqrt{\partial_{rr} U(r, \ell)}$

[1] In the diffusion-limited first-passage time of a singe particle, the attractive potential can be considered as infinitely strong, and one may question the validity of assuming a smooth potential top. For polymers, however, we argue that the fluctuation of chain ends is rapid and "compact" (see Doi's argument below), thus smoothing the barrier top. In Appendix 6.5.1, we show that a "cusp-shaped" barrier also leads to essentially the same τ_{Kr} for loop formation as does a smooth potential barrier.

are evaluated at the top and bottom of the effective potential $U(r,l)$.[2] Here, we do not repeat the derivation of this result (see Appendix 6.5.1) but instead state the basic assumptions on which this result relies. Besides the strong-damping condition, a steady-state condition was assumed, based on $\Delta U \gg k_BT$. In other words, when the barrier is much higher than the thermal energy k_BT, the barrier-crossing rate is expected to be very small, and, thus, the solution of Eq. 6.13, $P(r,\ell,t)$, is expected to change very slowly with time, i.e., it remains very close to a steady-state solution. In the literature (e.g., [167]), this is often pictured as a system of non-interacting particles trapped in a potential well with a particle "source" and a particle "absorber," which keep the escape current constant: As soon as a particle escapes the barrier, it will be removed, and a new particle is then injected at the bottom of the potential. Here, the dominant contribution to the escape rate is the exponential term, often referred to as the Arrhenius factor. Other factors that also influence the Kramers rate are the curvatures (ω_b and ω_t) and friction. Larger friction means slower escape and hence longer τ_{Kr} as evidenced by Eq. 6.15. The curvature dependence of τ_{Kr} can also be understood: ω_b and ω_t are, respectively, the frequency of small oscillations around the potential bottom and bottom, which can be interpreted as the attempt rate.

It proves useful to rewrite τ_{Kr} in Eq. 6.15 as

$$\tau_{Kr} = \frac{\zeta_{\text{eff}}}{\omega_t} \times \left[\frac{2\pi}{\omega_b} \exp\left(\frac{\Delta U}{k_BT}\right)\right]. \tag{6.16}$$

Note that the term in brackets is the escape time in the transition-state theory (TST): $\tau_{TST} = \frac{2\pi}{\omega_b}\exp(\Delta U/k_BT)$ [158]. (See Appendix 6.5.1) As it turns out, the estimate τ_{TST} errs because it is too much of an equilibrium estimate. It can be obtained by counting particles crossing the barrier from right to left per unit time. In the polymer case, this time scale is related to an equilibrium ring-closure probability through $\tau_{TST} \sim G_0^{-1}$—the number of "particles" escaping the barrier in the sense of TST is inversely proportional to G_0. The extra factor in Eq. 6.16 implies that barrier crossing is further slowed down by diffusion of the particle on the barrier top until it is captured by the absorber; in the large friction limit, $\zeta_{\text{eff}}/\omega_t \gg 1$ and $\tau_{Kr} \gg \tau_{TST}$. In fact, the factor $\frac{\omega_t}{\zeta} \sim \frac{1}{a\zeta}$ is

[2]For intermediate-to-strong damping, the Kramers time τ_{Kr} is given by

$$\tau_{Kr}^{-1} = \frac{D_0}{k_BT}\frac{\omega_b\,\omega_t}{\pi} e^{-\frac{\Delta U}{k_BT}} \Bigg/ \left(1+\sqrt{1+\frac{4mD_0^2\,\omega_t^2}{(k_BT)^2}}\right).$$

The correction term $\frac{4mD_0^2\,\omega_t^2}{(k_BT)^2}$ is $\approx 10^{-7}$ for DNA monomers and can be neglected, justifying our use of the strong-damping limit (Eq. 6.15). This condition is consistent with the one given at the beginning of Sec. 6.3, i.e., $\frac{m}{\eta} \ll \frac{b^2}{D_0}$, as long as $a > b$, which can be easily seen by writing $\frac{4mD_0^2\,\omega_t^2}{(k_BT)^2} \ll 1$ as $\frac{m}{\eta} \ll \frac{k_BT}{\omega_t^2}\frac{1}{D_0} \approx \frac{a^2}{D_0}$.

proportional to the rate at which a random walk is captured by a spherical absorber of radius a [168]. As a result, $\tau_{Kr}(\ell)$ varies as $\tau_{Kr} \sim \frac{1}{\alpha D_{\text{eff}}} \sim \frac{1}{a D_{\text{eff}}}$. This dependence is unique to a random walk in the diffusion-limited case, where an absorbing boundary condition is imposed[3] and has nothing to do with equilibrium chain properties.

The simple scaling argument based on Eq. 6.16 gives the qualitative features of τ_{Kr}. More careful analysis of the Kramers formula in Eq. 6.15 leads to the surprisingly simple result,

$$\tau_{Kr}(\ell) = \mathcal{C} \frac{1}{\alpha D_{\text{eff}}} \frac{\ell_p^2}{G_0(\ell)}, \tag{6.17}$$

with $\mathcal{C}\left[r_b, G(r_b,\ell)\right] = 2\sqrt{2}\pi r_b^2 G(r_b,\ell) / \left(\frac{6}{r_b^2} - \frac{G''(r_b,\ell)}{G(r_b,\ell)}\right)^{1/2}$, a dimensionless prefactor that is practically a constant for all ℓ [155].[4]

Eq. 6.17 is a direct result of our hypothesis (Eq. 6.12) that the closing time may be estimated using the static distribution $G(r,\ell)$. As noted earlier, no analytic expression for $G(r,\ell)$ has been found that is accurate for all r and ℓ, and one must make do with a pastiche of approximations that are applied in different limits for r (and ℓ). For $r = 0$, we use the interpolative formula due to Ringrose *et al.* [163] mentioned above, which blends SY with the result for a freely jointed chain, $G_0(\ell) \sim \ell^{-3/2}$. For $r > 0$, we use the TH approximation [140] presented in Eq. 6.7. Using TH, we find that the dimensionless prefactor $\mathcal{C}(\ell)$ of Eq. 6.17 is $\mathcal{O}(10^{-1})$, varying less than a factor of 2 over $0 < \ell < \infty$.

One subtle issue of the single-variable picture, such as the one considered in this chapter, is the choice of D_{eff}. In general, D_{eff} can have a non-trivial dependence on the chain length ℓ. In what follows, we adopt the recent result $D_{\text{eff}} = 2D_0$ (where, D_0 is the diffusion constant for individual monomers), summarized in Refs. [149, 150]. Briefly, $D_{\text{eff}} = 2D_0$ is the relative diffusion constant of the chain ends, which is consistent with the interpretation of Eq. 6.16 that the friction-independent

[3]For a smooth short-range potential of range α, the curvature at the top must be $\sim 1/\alpha$ by dimensional analysis. We note that many simulations assume reaction upon first passage through the distance α. Despite the seeming difference between our Kramers' approach and simulations that track the time for particle ends to first pass through the $r = \alpha$ sphere, the "particle" (in a single-particle picture) in both cases is not allowed to equilibrate within the reactive region $r \approx \alpha$. Thus, in each case, one expects $\tau_c \sim 1/\alpha$ for $\alpha \ll 1$ (cf. Eq. 6.17). If we had assumed kinetic-limited looping, then the particle would sample most of the reactive region, resulting in $\tau_c \sim 1/\alpha^2$ [145].

[4]We note that the numerical prefactors in Eq. 6.17 and 6.18 depend on the form of capture force $f(r/\alpha)$, while their scalings are not affected by the form of short-range attractive forces (Appendix 6.5.1). Here, we have used a direct differentiation of Eq. 6.12 to calculate ω_t.

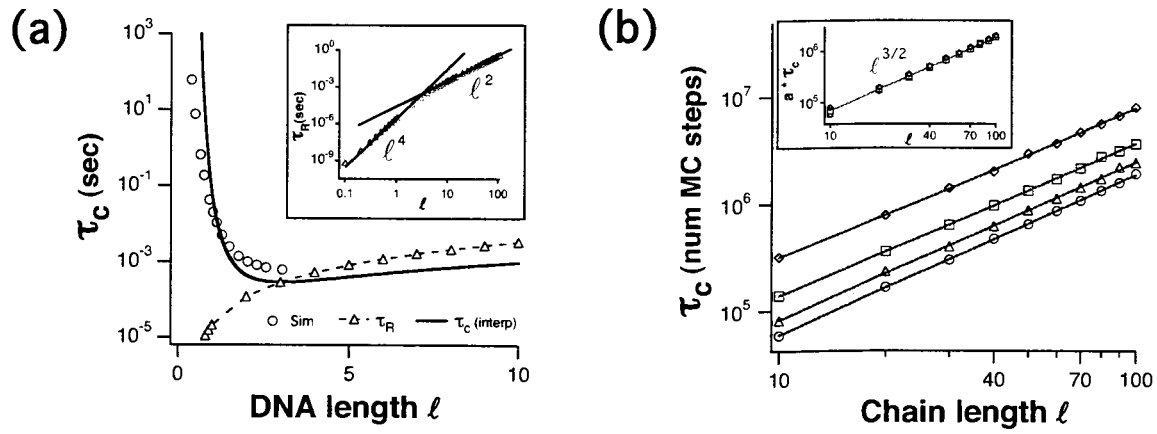

Figure 6.5: Closing time τ_c vs. chain length. (a) Brownian Dynamics simulation [153] (empty circles) and Kramers theory (eq. 6.17) are shown. For direct comparison, we used the same parameters as in the Ref. [153] (bead size = 3.18 nm for $D_{\text{eff}} = 2D_0 = 1.54 \times 10^{-11}\text{m}^2/\text{s}$ and $\alpha = 0.1$) with ℓ_p = 50nm. For $G_0(\ell)$, we used an interpolation by Ringrose *et al.* [163] (see text). Relaxation times τ_R for these parameters are also shown (triangular symbols), with the ℓ^4 and ℓ^2 scaling regimes apparent in the inset. (b) Single-"particle" MC simulations of τ_c with the potential $U/k_BT = -\log[P(r,\ell)]$ taken from Fig. 6.4b. Here, τ_c is a first-contact time averaged over about 2000 realizations of the initial position randomly selected from $P(r,\ell)$. We have chosen $\alpha = 0.25, 0.5, 0.75, 1.0$. As expected, $\tau_c \sim \frac{\ell^{3/2}}{a}$ (inset).

τ_{TST} explains the the time required to bring the "particle" near the barrier top, while the friction-dependent capture rate $\frac{\zeta_{\text{eff}}}{\omega_t}$ explains the diffusion (in our case, the fluctuations of the chain ends) of the particle at the barrier top.

In Fig. 6.5(a), we plot the $\tau_{Kr}(\ell)$ that results from Eq. 6.17, using the various approximations to $G(r,\ell)$ discussed above. The solid curve uses the Ringrose expression for all ℓ. The two curves compare well with recent simulations using parameters appropriate to dsDNA [153, 156, 169]. Note that the material parameters of the simulation were used (see caption). Considering the heuristic nature of the arguments, the agreement is excellent.

One striking feature of the plot of $\tau_{Kr}(\ell)$ is the existence of a minimum at $\ell \approx 3.4$, where

$$\tau^*_{Kr} = 0.78\frac{\ell_p^3}{a\,D_0}. \tag{6.18}$$

In Eq. 6.18, the prefactor 0.78 is calculated by a Monte Carlo simulation of $G(r,\ell)$, done in units of seconds. It is about 10% less than the prefactor obtained using the TH approximation.[5] As mentioned above, the existence of a minimum in τ_{Kr} reflects a balance between the energy of bending and the entropy of conformations that must be searched for two ends to meet.

For the above Kramers-rate calculation to hold (i.e., for the closing-time τ_c to equal τ_{Kr}), three conditions must be satisfied: (1) The damping must be sufficiently strong. (2) The barrier height ΔU must be large compared to k_BT (recall that this alone approximately ensures a steady-state condition as is assumed in the Kramers approach). And (3) the global chain-relaxation time τ_R must be much shorter than the Kramers time τ_{Kr}.

The first condition is normally satisfied for molecules in solution. For the second, since there is a minimum in the effective potential at r_b, we require that $\alpha \ll r_b$ so that the barrier height is large. The condition $\Delta U/k_BT = 1$ is shown in Fig. 6.6 as a dotted line in the $\ell - \alpha$ parameter plane, using a diffusion constant appropriate to dsDNA. To the left of the dashed line, the barrier height is larger than k_BT.

The third condition, $\tau_R \ll \tau_{Kr}$, is more subtle and requires discussion. In using a "one-particle" description of chain-closing dynamics, we are assuming that all internal degrees of freedom of the polymer chain have relaxed. As a result, the end-to-end distance r is the only dynamic variable (cf. Eq. 6.22). This assumption of local equilibrium is equivalent to assuming that the effective potential felt by the particle is derivable from the time-independent distribution $G(r,\ell)$. For $\Delta U/k_BT \gg 1$, the particle in local equilibrium will relax in the potential well, except around $r \approx \alpha$ in our diffusion-limited case. If the chain relaxation times are too long, our one-particle picture breaks down, because the chain dynamics are not well-characterized by a single timescale, such as the Rouse time. This will not only influence the ℓ dependence but also the α dependence of the closing time (see below). We thus compare the scaling behavior of $\tau_R(\ell)$ with $\tau_{Kr}(\ell)$ and $\tau_c(\ell)$ in both the flexible ($\ell \gg 1$) and stiff-chain ($\ell \lesssim 1$) limits.

In the flexible limit, we can use the Rouse model to estimate the longest relaxation time, which gives $\tau_R \sim \ell^2$, in units of the basic time scale ℓ_p^2/D_0. By contrast, at large ℓ, Eq. 6.17 gives $\tau_{Kr} \sim \ell^{3/2}/\alpha$. (This is just the result of SSS [145, 149] and has been confirmed by single-"particle" simulations—see Fig. 6.5(b) and the caption.) Thus, when $\ell > 1/\alpha^2$, the third condition is violated

[5]To calculate the end-to-end distribution $G(r,\ell)$, we have used a standard Kratky-Porod-type model for Monte Carlo simulation. In other words, a randomly selected monomer rotates an arbitrary angle about the axis defined by the vector connecting the two nearest-neighbor monomers. See, for example, the simulation methods in Ref. [156].

and the Kramers calculation does not hold. In this case, we can still estimate the upper-limit of τ_c as follows: The closing time is at most the time necessary for the slowest "random walker" to travel, by diffusion of the entire chain ($D_{\rm CM} \sim D_0/l$, where CM stands for center-of-mass), the mean end-to-end distance r_g. Since $r_g \sim \sqrt{\ell}$, we have $\tau_c \lesssim \frac{r_g^2}{D_{\rm CM}} \sim \frac{\ell^2}{D_0} \sim \tau_R$. In other words, when the third condition does not hold, τ_c is not τ_{Kr} but is set by the Rouse time τ_R. On the other hand, the α-dependence of the closing time of a Rouse chain is a delicate issue.

In an important paper [148], Doi has shown that $\tau_c \sim \tau_R$ and is independent of the reaction radius α, for $1 \ll \alpha \ll r_g$ (the "Doi-condition").[6] Doi's basic reasoning is that, if one expresses the end-to-end vector $\vec{r}(t)$ in terms of the normal modes, the first normal mode represents a random walk in a harmonic potential and dominates the long-time behavior of $\vec{r}(t)$. On the other hand, the higher modes correspond to a stronger harmonic potential, relaxing faster; they are rapid compared to the first mode and can be considered as the fluctuation of $\vec{r}(t)$, which is very small (i.e., $\delta r \ll |\vec{r}(t)|$). If $\delta r \ll \alpha$, then the fluctuation does not affect the looping dynamics and $\tau_c \propto 1/\alpha$. If $\delta r \geq \alpha$, however, the reaction takes place as soon as $|\vec{r}(t)|$ becomes smaller than δr (not α), since the motion of $\vec{r}(t)$ is very fast and "compact" in the sphere of radius δr. Later, de Gennes explained the reaction-radius-independence and dependence of reaction rate in terms of compact vs. non-compact exploration, respectively [170].

As the chain stiffness increases, the looping dynamics enters the regime of noncompact exploration. In other words, the a dependence of τ_c in the stiff-chain limit is not complicated by internal modes. To see this, note that chain stiffness leads simultaneously to faster relaxation times τ_R and higher energy barriers, which implies that the Kramers calculation should be valid. As shown in the previous section, for $L < \ell_p$, $\tau_R \sim \frac{L^4}{2\ell_p b D_0}$ and the third condition ($\tau_R \ll \tau_{Kr}$) is always satisfied: the lower limit of τ_c is given by the time scale for a random walk to travel a distance $R \sim L$; thus, $\tau_{Kr} \sim \tau_c \gtrsim \frac{R^2}{D_{\rm CM}} \sim \frac{L^3}{b D_0} > \frac{L^4}{\ell_p b D_0} \gtrsim \tau_R$.

To summarize, $\tau_R \sim L^4$ for $\ell < 1$ and $\sim L^2$ for $\ell \gg 1$: contrary to what one may expect, the looping dynamics is much more subtle for flexible chains than for semiflexible chains. In other words, for large-enough ℓ, τ_R becomes larger than the Kramers estimate [165],[7] as shown in Fig. 6.5(a) and in the inset.

In Fig. 6.6(a), we summarize the above arguments schematically in a closing-time tree. In

[6]Note also that the condition $\ell > 1/\alpha^2$ in previous paragraph implies that $r_g \gtrsim 1/\alpha$, since $r_g \sim \ell^{1/2}$.

[7]Using the results in this referencee, we have derived an approximate interpolation, accurate for all ℓ: $\tau_R(\ell) = (2/3\pi^2)(\ell_p^2/D_{chain})\frac{\ell^3}{(\pi/4)^2+\ell^2}$. This interpolation is used in Fig. 6.5(a) (inset).

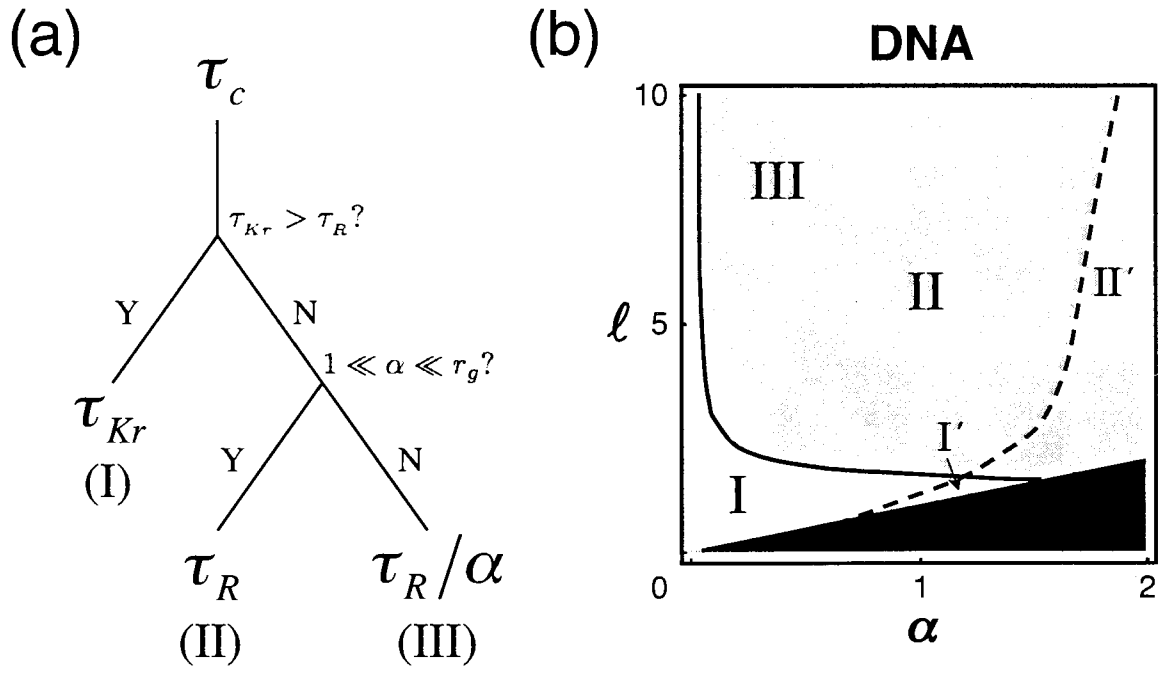

Figure 6.6: Closing time: Kramers time vs. Rouse time (see text). (a) Tree diagram. (b) Scaling regimes in the ℓ-α for DNA. Region I is the Kramers regime, with $\tau_c > \tau_R$; Region II is the dynamic-fluctuation regime. Region III is the intermediate regime. Crudely speaking, this is a region that separates Regions I and II. Also note that the boundary between regions II and III for large ℓ was constructed with the aid of the Doi's condition (see the text). On the other hand, the boundary for small ℓ was constructed based on the following physics ground: As ℓ decreases, δr decreases, implying that the intermediate region is narrower for smaller ℓ. In the primed regions to the right of the dashed line, $\Delta U/k_BT < 1$. The black region is unphysical: $a > L$.

Fig. 6.6(b), we also *qualitatively* plot $\tau_R(\ell) = \tau_{Kr}(\ell)$ in the ℓ-α plane. The white area is Region I (Kramers Regime), where $\tau_{Kr} > \tau_R$, and therefore $\tau_c \sim \tau_{Kr}$. The shaded area is Region II ("dynamical fluctuation" or "Doi" Regime, see below), where $\tau_{Kr} < \tau_R$ and $\tau_c \sim \tau_R$. Areas I′ and II′ show where $\Delta U < k_BT$. The black region, defined by $\alpha > \ell$, is unphysical. Finally, Region III is the intermediate regime, where $\tau_R > \tau_{Kr}$ and $\tau_c \sim \tau_R/\alpha$.

In Region II, the relaxation and closing processes are coupled. In this case, one may have to solve an N-particle diffusion problem, subject to a boundary condition that is difficult to im-

pose [146–149]. Nevertheless, much insight can still be obtained from the simple scaling analysis of random walks given above. In this view, a chain can close because the two ends randomly meet each other while freely relaxing. The existence of such a dynamical-fluctuation or "Doi" regime, where $\tau_c \sim \tau_R$, is a unique feature of flexible chains (Fig. 6.6) – the dynamic fluctuation $\delta R(t) \equiv \sqrt{\langle [R(t) - R(0)]^2 \rangle}$ grows up to R as $t \to \tau_R$ and thus can assist chain closing. For a Rouse chain, $\delta R(t)$ can be given as a sum of Rouse modes [136, 148] and, in our simple scaling analysis, τ_c can be inferred by analyzing this. The short-time behavior of $\delta R(t)$ reflects the internal motion and varies as $\delta R(t) \sim \sqrt{t}$ for $t \ll \tau_R$. (See Appendix 6.5.2). We argue, however, that this will not appreciably influence τ_c, as $\delta R(t) \to R$ only when $t \to \tau_R$. In other words, τ_c is governed by the slowest mode and our assertion of $\tau_c \sim \tau_R$ will not be invalidated by the internal motion, which is important at time scales much smaller than τ_c (or τ_R) – according to our earlier discussion, the internal motion in the flexible-chain limit only influences α dependence of τ_c. In the stiff-chain limit, this dynamical fluctuation regime disappears. Note that the boundaries between Regions I and II are not sharp but are crossovers. Loop-formation kinetics in the crossover area will likely combine aspects of both regimes, as indicated in recent simulations [149] and by results that show that τ_{SSS} and τ_{Doi} are respectively lower and upper bounds for τ_c [150].

As the Doi-condition $1 \ll \alpha \ll r_g$ for Region II is violated, τ_c becomes dependent upon $1/\alpha$ [148]. Indeed, based on their BD simulation results, Podtelezhnikov *et al.* [171] suggested that $\tau_c \simeq \tau_R/\alpha$ when $1 \approx \alpha \ll r$. In Fig. 6.6, this is Region III.

Our discussion has neglected hydrodynamic effects and excluded-volume interactions. Both can influence chain relaxation and closing simultaneously. The hydrodynamic effect will not change τ_{Kr}, since it is a function of the equilibrium distribution $G(r, \ell)$. However, the hydrodynamic interaction tends to promote chain relaxation (e.g., in the Zimm model, $\tau_R \sim \ell^{3/2}$, in contrast to $\tau_R \sim \ell^2$ in the Rouse model considered here [136]) by increasing the mobility of the chain, resulting in a wider Kramers regime than implied by Fig. 6.6. On the other hand, the excluded-volume interaction both decreases $D_{\rm CM}$ and reduces G_0 [136, 172]. But for loops of just a few persistence lengths, which are the most physically relevant (see below), both effects are expected to be minor. A final caveat is that we have assumed isotropic binding interactions. While mathematically simpler and relevant to simulations [153], most real polymers have directional bonding. In the Kramers calculation, this would modify $G_0(\ell)$.

The Kramers calculation holds in Region I of the $\ell - \alpha$ parameter space shown in Fig. 6.6. What are the physically relevant values of α and ℓ? The interaction distance $a = \alpha \ell_p$ will be the thickness

of the polymer, or less. For polymers of biological interest, the persistence length will be typically at least this size and often much larger. For example, for double-stranded DNA, the monomer size is 0.34 nm while the persistence length is 50 nm. For chromatin, the thickness is 30 nm, comparable to its persistence length [124].[8] Thus, we generally expect $\alpha < 1$ and sometimes $\alpha \ll 1$.

What are the relevant values of ℓ? Although polymers in principle may have any length, the existence of a minimum closing time τ^*_{Kr} (Eq. 6.18) leads one to speculate that where looping is biologically relevant, polymer lengths near $\ell \approx 3 - 4$ might be favored because they minimize τ_c. In this regime, the Kramers calculation will be valid, for small α. Thus, biological selectivity may arise from a physical mechanism. Indeed, in Ch. 5 we have shown that the typical spacings between replication origins in early embryo *Xenopus* are 3-4 times the ℓ_p of chromatin, the DNA-protein complex present during replication. It is then natural to speculate that origins are related by looping and that the spacing may have been selected to maximize the contact rate of origins, optimizing replication efficiency.

In conclusion, we have shown that Kramers rate theory gives a straightforward order-of-magnitude estimate of the closing time of a semiflexible polymer. We have examined how the static chain properties are reflected in the looping dynamics. Although phenomenological, the calculation explains the existence of a minimum closing time and accurately reproduces numerical simulations. Moreover, considering the requirements for the calculation to hold shows how the intertwining of the relaxation time with the closing time explains the apparently conflicting results for τ_c (SSS and Doi). Fortunately, the physically relevant cases are precisely the ones where the Kramers calculation is expected to hold. They may even be selected biologically through evolution. Finally, although we have neglected the possibility of formation of multiple loops (Fig. 5.2 vs. Fig. 6.1), we emphasize that, even in such cases, the intrinsic stiffness of polymer implies the existence of characteristic loop size, where the loop-formation probability is maximum and τ_c is minimum.

[8] Note that the value of the persistence length of chromatin fibers is still controversial. See endnote 30 of Dekker *et al.* [124].

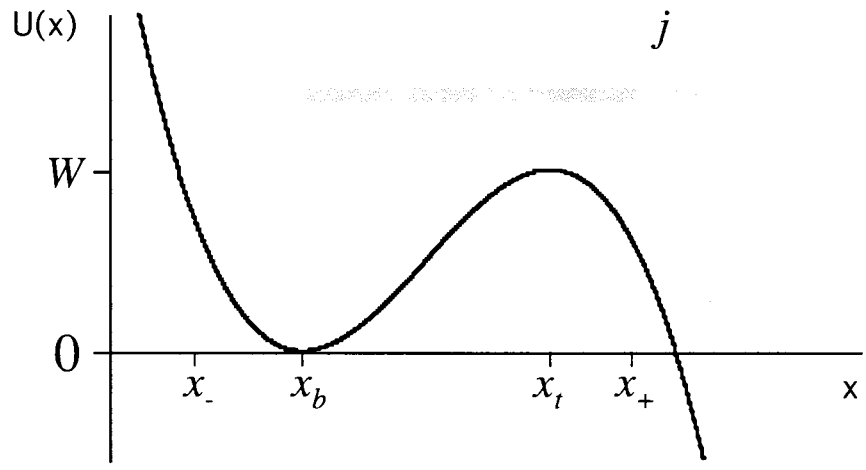

Figure 6.7: Illustration of the trapping potential $U(x)$. The current j gives the flux of particles tunneling from the bottom well over the top.

6.5 Appendix

6.5.1 Review of the Kramers problem

Kramers treatment of the escape of a particle over a potential barrier extended an earlier theory known as the Transition-State Theory (TST). We begin with a review of TST and then show how to add the effects introduced by Kramers [158, 173, 174].

The transition-state theory (TST)

Imagine a classical particle placed in the vicinity of the bottom $x = x_b$ of the potential $U(x)$ in Fig. 6.7, where the potential barrier height $W = U(x_t) - U(x_b)$ is larger than the average energy $\langle E \rangle \sim k_B T$ of the particle. (Here, x is a reaction coordinate coupled to an environment.) In other words, the particle is trapped. In the presence of thermal fluctuations, however, this particle can escape from the potential well, since there is always a non-zero probability $\sim \exp(-E/k_B T)$ that the particle can acquire enough energy $E > W$ from the environment. More precisely, the environment provides the thermal noise whose fluctuations can kick the particle over the barrier. If the thermal energy $k_B T$ is much smaller than the barrier height W, the particle will escape from the trap after a long time τ_{esc}, when the accumulated action of the random force has driven it over the barrier. In this case, a particle inserted into the trap initially equilibrates in the potential well in a

time $\tau_{eq} \ll \tau_{esc}$, approaching the Boltzmann distribution

$$P_{eq}(x,v) = \begin{cases} \frac{1}{Z} e^{-\frac{1}{k_B T}\left\{\frac{1}{2}mv^2 + U(x)\right\}} & (x \le x_t) \\ 0 & (x > x_t) \end{cases} \tag{6.19}$$

At short times, the normalization constant Z can be calculated as

$$\begin{aligned} Z = Z_v\, Z_x &= \left[\int_{-\infty}^{\infty} dv\, e^{-\frac{1}{2}\frac{mv^2}{k_B T}}\right] \cdot \left[\int_{-\infty}^{x_t} dx\, e^{-\frac{U(x)}{k_B T}}\right] \\ &\approx \left[\sqrt{\frac{2\pi k_B T}{m}}\right] \cdot \left[\sqrt{\frac{2\pi k_B T}{m\omega_b^2}} e^{-\frac{U(x_b)}{k_B T}}\right], \end{aligned} \tag{6.20}$$

where we have used the quadratic approximation $U(x) \approx U(x_b) + \frac{1}{2}m\omega_b^2(x - x_b)^2$ for the potential U in the vicinity of $x = x_b$, where the main weight of the integral over x is located. We also extend the upper limit of the integral from x_t to ∞, an approximation that is accurate as long as the barrier height is much larger than $k_B T$.

From Eq. 6.19, we can obtain a first estimate of the escape rate by calculating the current j of right-moving probability,

$$j = \int_0^{\infty} dv\, v\, P_{eq}(x = x_b, v) = \frac{\omega_b}{2\pi} e^{-\frac{W}{k_B T}}. \tag{6.21}$$

This is the result of the classical transition-state theory (TST) [158], where the escape rate is proportional to the "attempt rate" ω_b and the Boltzmann factor $k_B T$. The TST rate is always an upper bound to the true rate because it is based on the following two assumptions: (i) Thermodynamic equilibrium prevails throughout the entire system for all degrees of freedom. Any deviation from the equilibrium distribution is neglected. (ii) Once the particle crosses the barrier, it never diffuses back.

In the Kramers escape problem, one treats the trapped particle via Langevin dynamics. Below, we derive the escape rate for the strong-damping case.

The flux-over-population method

We start with the Langevin equation for the particle,

$$m\ddot{x} = -U'(x) - \gamma\, m\dot{x} + \xi(t), \tag{6.22}$$

where the prime indicates differentiation with respect to x. The fluctuating force $\xi(t)$ denotes Gaussian white noise with zero mean, obeying the fluctuation-dissipation theorem,

$$\langle \xi(t) \rangle = 0 \tag{6.23a}$$

$$\langle \xi(t) \cdot \xi(t') \rangle = 2m\gamma k_B T\, \delta(t - t'). \tag{6.23b}$$

In the strong-damping case, one drops the inertial term $m\ddot{x}$ in Eq. 6.22. From Eqs. 6.22-6.23b, one can then obtain the time evolution of the probability $p(x,t)$ (the so-called Smoluchowski equation) [137]

$$\frac{\partial p(x,t)}{\partial t} = \frac{1}{m\gamma}\left[\frac{\partial}{\partial x}U'(x) + k_B T \frac{\partial^2}{\partial x^2}\right] p(x,t). \tag{6.24}$$

Note that Eq. 6.24 has the structure of the continuity equation $\frac{\partial p(x,t)}{\partial t} + \vec{\nabla} \cdot \vec{j}(x,t) = 0$, where $j(x,t)$ is identified as $-\frac{1}{m\gamma}\left[U'(x) + k_B T \frac{\partial}{\partial x}\right] p(x,t)$.

In rate theory, a common procedure to calculate the escape rate is to consider a stationary situation in which a steady probability current from x_b to x_t is maintained by sources and sinks of particles [158]. The sources supply the potential well with particles at energies that are a few $k_B T$ below the barrier-height W. These particles first equilibrate before they eventually leave the well over the barrier. Beyond the barrier, the particles are removed immediately by sinks. The total probability flux j over the barrier is then given by the product of the escape rate k from x_b to x_t, and the population of the well n_0, i.e.,

$$k = \tau_{esc}^{-1} = \frac{j}{n_0}. \tag{6.25}$$

We place the source at $x_- < x_b$ and the sink at $x_+ > x_t$. The stationary solution $\rho(x)$ then carries the current j and obeys the absorbing boundary condition $\rho(x = x_+) = 0$. Thus, $\rho(x)$ is given by the following solution:

$$j = -\frac{1}{m\gamma}\left[U'(x) + k_B T \frac{\partial}{\partial x}\right] \rho(x). \tag{6.26}$$

This equation is easy to solve by noting that it has an integrating factor,

$$k_B T\, e^{-\frac{U(x)}{k_B T}} \frac{d}{dx}\left[e^{\frac{U(x)}{k_B T}} \rho(x)\right] = \frac{dU(x)}{dx}\rho(x) + k_B T \frac{d\rho(x)}{dx} = -m\gamma\, j. \tag{6.27}$$

Thus, the stationary solution of the distribution is obtained as

$$\rho(x) = \frac{m\gamma|j|}{k_B T}\, e^{-\frac{U(x)}{k_B T}} \int_x^{x_+} e^{\frac{U(y)}{k_B T}} dy, \tag{6.28}$$

while the population n_0 is simply $n_0 = \int_{-\infty}^{x_t} dx\, \rho(x)$. Therefore, we obtain the following average escape time

$$\tau_{esc} = k^{-1} = n_0/j = \frac{m\gamma}{k_BT} \int_{-\infty}^{x_+} dy\, e^{-\frac{U(y)}{k_BT}} \int_{y}^{x_+} dz\, e^{\frac{U(z)}{k_BT}}, \tag{6.29}$$

which can be integrated by parts as follows:

$$\tau_{esc} = \frac{m\gamma}{k_BT} \int_{-\infty}^{x_+} dy\, e^{\frac{U(y)}{k_BT}} \int_{-\infty}^{y} dz\, e^{-\frac{U(z)}{k_BT}} \tag{6.30a}$$

$$\approx \frac{m\gamma}{k_BT} \underbrace{\int_{x_b}^{x_t} dy\, e^{\frac{U(y)}{k_BT}}}_{I_1} \cdot \underbrace{\int_{-\infty}^{x_b} dz\, e^{-\frac{U(z)}{k_BT}}}_{I_2} \quad (W \gg k_BT). \tag{6.30b}$$

For smooth bottom and top of barriers that can be approximated as $U(x) = U(x_{b,t}) \pm \frac{1}{2}m\omega_{b,t}^2(x - x_{b,t})^2$, it is straightforward to show using Eq. 6.30b that

$$\tau_{esc} = \left[\frac{\omega_b\omega_t}{2\pi\gamma}\, e^{-\frac{W}{k_BT}}\right]^{-1}. \tag{6.31}$$

Re-derivation of scaling in Eq. 6.17 [175]

Note that Eq. 6.30 does not depend on the shape of the potential top, while Eq. 6.31 assumed a parabolic shape. In other words, ω_b and ω_t are the curvatures at $x = x_b$ and $x = x_t$, respectively.

In Eq. 6.17 in Sec. 6.4, the $1/\alpha$ dependence came from the curvature ω_t at the potential top ($r = \alpha$); however, if there is no attraction between the two sticky ends of the polymer, it is more appropriate to consider the first-passage time when the ends first are within a distance a of each other. In this case, the effect is to truncate the potential at x_t, implying that there is a cusp at x_t rather than a smooth top. One may then question whether the scaling in τ_{Kr} is still valid. In fact, Eq. 6.17 is a general result. To see this, for Eq. 6.12 [$U(r,\ell) = -k_BT \ln P(r,\ell)$], we note that the integrand in the first integral I_1 in Eq 6.30b is

$$e^{\frac{U(r)}{k_BT}} = [4\pi r^2 G(r,\ell)]^{-1}. \tag{6.32}$$

Then, I_1 becomes

$$\begin{aligned} I_1 &= \int_{r_b}^{r_t=\alpha\ll 1} \{4\pi r^2\, G(r,\ell)\}^{-1} dr \\ &\approx \frac{1}{G(0,\ell)} \int_{r_b}^{r_t=\alpha} \frac{dr}{4\pi r^2} \\ &\sim \frac{1}{\alpha\, G(0,\ell)}, \end{aligned} \tag{6.33}$$

and we recover the scaling in Eq. 6.17, which is valid even for a non-parabolic potential top (i.e., in the absence of artificial attractive potentials in Fig. 6.4).

6.5.2 Reaction-radius dependence and compact vs. non-compact exploration

To understand the α-independence of $\tau_c \sim \tau_R$ for $\ell \gg 1$,[9] it is worth considering first the much simpler case of free random walks, which are characterized by diffusive motion:

$$\delta x(t) \equiv \sqrt{\langle [\vec{x}(t) - \vec{x}(0)]^2 \rangle} \sim \sqrt{Dt}.$$

The rate at which a random walk is captured by an absorbing sphere of radius a in a steady-state is proportional to aD. Note that the rate at which two random walks of radius a collide into each other also varies as aD. This simply states how effectively the random walk "searches" the volume available to it [177]. For a time t, the random walk has searched through a total volume of $\sim aDt$. This implies that the collision rate or the absorbing rate is proportional to aD, reminiscent of $\tau_{Kr}^{-1} \sim aD$. It is instructive to compare this with the corresponding collision rate of molecules in a gaseous phase, which is proportional to $1/a^2$. The main difference between these two cases is that the path of a random walk is denser. Random walks are hence correctly referred to as space-filling objects [177].

To further proceed with this line of reasoning, consider the general case for which the time evolution of particles follows $\delta x(t) \sim t^{\gamma/2}$.[10] Let us introduce the density of volume searched by a particle during a time t as $\rho(t)$, which equals the ratio of the total volume explored to the (distance the particle has travelled)^3. Clearly, $\rho(t) \sim t/\left(t^{\gamma/2}\right)^3 \sim t^{1-3\gamma/2}$. When $\gamma < 2/3$, $\rho(t)$ diverges as $t \to \infty$. This divergence implies that any volume fraction δV will be visited infinitely often (this phenomenon is termed "compact exploration" [170]). It is not hard to imagine that the a-dependence of the collision or absorbing rate is dictated by the exponent γ; we have already seen the difference between the cases $\gamma = 2$ (gaseous molecules) and $\gamma = 1$ (free random walk). For $\gamma < 2/3$, the rate is expected to become insensitive to a, since the paths of the particles overlap many times over the length scale of a: When two such particles separated by a distance d have travelled a distance $\sim d$, their paths have certainly crossed (i.e., reacted) each other, no matter how small a is.

[9] This section reports recent results of Bae-Yeun Ha [176].

[10] Note that the exponent is not intrinsic to the random walk. It is determined by such factors as space dimensions or the presence of disorder in the medium in which the random walk takes place.

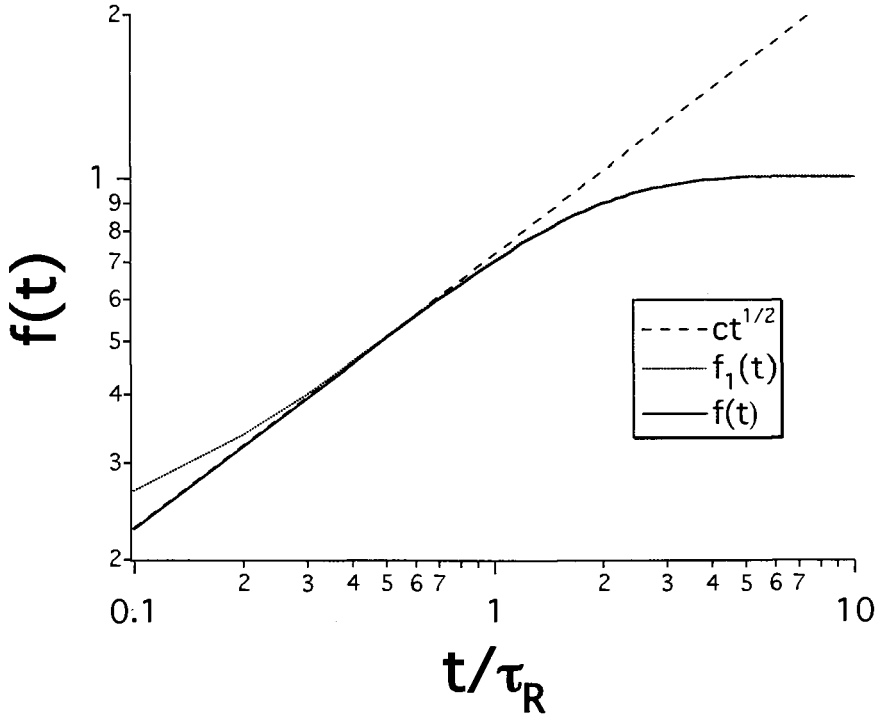

Figure 6.8: The function $[f(t)]$ as a function of t/τ_R along with a short-time ($ct^{1/2}$) and long-time approximation ($f_1(t)$). The constant c is chosen so that the two curves match each other for sufficiently small t. For $t \lesssim \frac{1}{2}\tau_R$, $\phi(t)$ varies as $(t/\tau_R)^{1/2}$, while for $t \gtrsim \frac{1}{2}\tau_R$, $f(t) \approx f_1(t)$. In each region, $f(t)$ and its approximation essentially collapse onto each other. (Courtesy of Bae-Yeun Ha.)

We now turn to the polymer problem. For simplicity, we only consider a Rouse chain (ideal flexible chain) here. In contrast to the previous random-walk case, polymer dynamics is complicated by the competition between various internal modes; a single exponent cannot fully characterize end fluctuations defined by $\delta R^2(t) \equiv \left\langle [R(t) - R(0)]^2 \right\rangle$. In terms of normal modes:

$$\delta R^2(t) = \delta R^2_\infty \cdot f(t), \tag{6.34}$$

where

$$f(t) = \frac{8}{\pi^2} \sum_p^\infty \frac{1}{p^2} \left(1 - e^{-tp^2/\tau_R}\right) \tag{6.35}$$

and $\delta R^2_\infty \equiv \delta R^2(t = \infty) = 2\left\langle R^2 \right\rangle$ and $p = 1, 3, 5....$

We find that $f(t) \sim (t/\tau_R)^{1/2}$ (see Fig. 6.8 and the caption) and hence $\delta R(t) \sim \delta R_\infty (t/\tau_R)^{1/4}$

(subdiffusive) for $t \lesssim \frac{1}{2}\tau_R$, while $\delta R(t) \approx \delta R_\infty f_1(t)$ for $t \gtrsim \frac{1}{2}\tau_R$, where $f_1(t) = 1 - \frac{8}{\pi^2}e^{-t/\tau_R}$ [11]. This means the path of $\vec{R}(t)$ is compact when it is observed over short time scales $t \lesssim \frac{1}{2}\tau_R$. Much beyond this, the end fluctuation gets saturated at its equilibrium value: δR_∞. The characteristic radius of Doi's sphere (inside which the path is compact) is then $R_{Doi} \approx \frac{1}{2}\delta R(t \approx \frac{1}{2}\tau_R) \approx \frac{1}{2}R = \frac{1}{2}\sqrt{Lb}$. Note that this is somewhat larger than Doi's original estimate based on equilibrium considerations [148]; internal modes are underestimated in the latter, leading to a smaller $R_{Doi} \approx 0.2R$. Following Doi [148], a-dependence of τ_c depends whether R_{Doi} is larger than a or not. When $R_{Doi} \gg a$ (or $r_g \gg \alpha$), then the interaction range is set by R_{Doi} rather than a.

As it turns out, the condition $r_g \gg \alpha$ is only a necessary condition for τ_c to be independent of α: $\tau_c \sim \tau_R$. Recall that, for subdiffusive motion, $\rho(t) \to \infty$ in the limit $t \to \infty$. On the other hand, the end fluctuation of a polymer gets saturated as $t/\tau_R \to \infty$. This implies that the limit $\rho(t) \to \infty$ is not realized in this analysis. If a is much larger than b, the smallest length scale in the system, however, the paths of the two ends will more likely overlap each other when they fall in the range R_{Doi}. Hence Doi's condition is summarized by $1 \ll \alpha \ll r_g$ for a Rouse chain.

[11] Strictly speaking, Eq. 6.35 (hence $f(t) \sim t^{1/2}$ for small t) holds in the continuum limit: $N \to \infty$ and $b \to 0$ so that $L = Nb$. For a chain consisting of a finite number of chain segments, $f(t)$ can be shown to vary as t for small t [148]. This implies that the Doi's regime is realized only for sufficiently large N.

Chapter 7

Conclusion

In this thesis, we have introduced several problems in theoretical physics that were inspired by the phenomenon of DNA replication. The 1D KJMA model has been extended to the case of arbitrary nucleation rate $I(t)$, and we have obtained various analytical results for evolution of domain-size distributions. We also have presented a new simulation algorithm that is faster than more standard methods by a factor of $10^2 - 10^3$. The simulation and the analytical results are in excellent agreement.

In addition, using the Kramers escape rate theory, we have obtained a simple analytical expression to estimate the closing time τ_c of biopolymers in the diffusion-controlled case. An interesting point is that the intrinsic stiffness of polymers implies a minimum chain closing time τ_c. Shorter chains require too much energy relative to the thermal energy k_BT, while longer chains need to search too many conformations for ends to find each other. The energy and entropy balance when the chain length is approximately 3-4 times its persistence length, giving the minimum loop-formation time and the maximum loop-formation probability.

Equally important, these theoretical tools have then been employed to tackle problems in DNA replication itself. First, DNA replication processes have been modeled as a 1D nucleation-and-growth problem, and the extended 1D KJMA model has been applied to extract the temporal program $[I(t)]$ of *Xenopus* early embryos. The extracted $I(t)$ from actual data of molecular-combing experiments shows striking features: replication origins fire throughout S phase, and the initiation rate suddenly increases in the middle of S phase.

Second, we have demonstrated that looping of chromatin can solve the long-standing "random-completion problem" in early embryonic DNA replication. In other words, origins of replication

in early embryos are distributed non-randomly along the genome, with typical spacings of 5-15 kb. In the absence of a sequence requirement, biologists have not been able to understand what exactly regulates the origin spacing. We have explained the distribution of origin-spacing based on chromatin looping, quantitatively. In particular, we have shown that the 5-15 kb origin-spacing corresponds to the typical loop-size of chromatin. Also, the persistence length 3.2 ± 0.1 kb of *Xenopus* sperm chromatin fiber deduced using the Shimada-Yamakawa distribution is consistent with experimental results for other organisms such as chicken *erythrocyte* and Yeast chromosome.

The successful interplay between theory and experiment presented in this thesis encourages us to to extend our methods even further. From the theoretical point of view, it would be highly desirable to generalize the kinetic model to include correlation (e.g., origin-interference effects) and sequence information in the nucleation rate I, as well as variable fork velocity v, to construct a complete replication profile. Such information can be obtained by molecular-combing experiments on a single-nucleus experiment, which is a formidable task but technically feasible.

Also, we have noted that the looping problem discussed in this thesis, that of a finite-sized chain with two reacting ends, is only the first step toward understanding the true chromatin dynamics during the cell cycle, especially during DNA replication. In real systems, many protein complexes distributed along a practically-infinitely-long chain interact with replication factories, forming multiple loops. In this case, we expect the loop-size distribution to decay exponentially (as opposed to the $\ell^{-3/2}$-algebraic decay of a single chain) and the corresponding dynamics to be much more complicated. We thus have to find a way to extend our results to the case of multiple-loop formation.

Perhaps a more important implication of our results is not that one can find interesting physics problems in biological systems but that we now have a model that makes quantitative predictions in DNA replication that can be tested *experimentally*. Indeed, with the recent progress on single-molecule manipulation techniques and genetic engineering, one can hope to see whether varying the persistence length of chromatin will change the kinetics of DNA replication of early embryos in the way that our theory predicts. In addition, because of the current detailed understanding of cell-cycle regulation and DNA replication, the kinetic model can be used as a tool to extract and compare replication profiles of various organisms. For example, understanding the replication kinetics of cancer cells and how this kinetics differs from that of normal cells would be one of the many important practical applications that one can entertain using the kinetic model.

Finally, we emphasize that, without the recent availability of large quantities of data such as were provided by the *Xenopus* experiment, a kinetic model based on the formal analogy between

the 1D KJMA model and DNA replication would have been just another "premature" calculation. In this thesis, I hope to have convinced the reader that our work on DNA replication is illustrative of a mature interaction between theory and experiment that will continue to bear fruit in the years ahead.

Bibliography

[1] Editorial, "Can physics deliver another biological revolution?," Nature **397**, 89 (1999).

[2] T. S. Kuhn, *The Structure of Scientific Revolutions.* University of Chicago Press, Chicago, 1962.

[3] S. Luria and M. Delbrück, "Mutation of Bacteria from virus sensitive to virus resistant," Genetics **28**, 491–511 (1943).

[4] E. Schrödinger, *What is Life?* Cambridge University Press, Cambridge, England, 1944.

[5] J. D. Watson and F. H. C. Crick, "Molecular structure of nucleic acids: A structure for deoxyribose nucleic acid," Nature **171**, 737–738 (1953).

[6] S. Forsén, ed., *Nobel Lectures in Chemistry 1971-1980.* World Scientific, Singapore, 1993.

[7] H. Frauenfelder, P. G. Wolynes, R. H. Austin, "Biological physics," Rev. Mod. Phys. **71**, S419–S430 (1999).

[8] G. Lim, M. Wortis, and R. Mukhopadhyay, "Stomatocyte-discocyte-echinocyte sequence of the human red blood cell: Evidence for the bilayer-couple hypothesis from membrane mechanics," Proc. Nat. Acad. Sci. **99**, 16766–16769 (2002).

[9] J. Hertz, A. Krogh, and R. G. Palmer, *Introduction to the Theory of Neural Computation.* Addison-Wesly, Reading, MA, 1991.

[10] W. M. Gelbart, R. F. Bruinsma, P. A. Pincus, and V. A. Parsegian, "DNA-Inspired Electrostatics," Physics Today (September), 38–44 (2000).

[11] L. H. Hartwell, J. J. Hopfield, S. Leibler, and A. W. Murray, "From molecular to modular cell biology," Nature **402**, C47–C52 (1998).

[12] M. A. Savageau, "Biochemical systems analysis. I. Some mathematical properties of the rate law for the component enzymatic reactions," J. Theor. Biol. **25**, 365–369 (1969).

[13] M. A. Savageau, "Biochemical systems analysis. II. The steady-state solutions for an n-pool system using a power-law approximation," J. Theor. Biol. **25**, 370–379 (1969).

[14] M. A. Savageau, *Biochemical Systems Analysis: A Study of Function and Design in Molecular Biology*. Addison-Wesley, Reading, Mass., 1976.

[15] U. Alon, M. G. Surette, N. Barkai, and S. Leibler, "Robustness in bacterial chemotaxis," Nature **397**, 168–170 (1999).

[16] M. B. Elowitz and S. Leibler, "A synthetic oscillatory network of transcriptional regulators," Nature **403**, 335–338 (2000).

[17] H. Jeong, S. P. Mason, A. L. Barabási, Z. N. Oltavi, "Lethality and centrality in protein networks," Nature **411**, 41–42 (2001).

[18] T. I. Lee, N. J. Rinaldi, F. Robert, D. T. Odom, Z. Bar-Joseph, G. K. Gerber, N. M. Hannett, C. T. Harbison, C. M. Thompson, I. Simon, J. Zeitlinger, E. G. Jennings, H. L. Murray, D. B. Gordon, B. Ren, J. J. Wyrick, J.-B. Tagne, T. L. Volkert, E. Fraenkel, D. K. Gifford, and R. A. Young, "Transcriptional Regulatory Networks in *Saccharomyces cerevisiae*," Science **298**, 799–804 (2002).

[19] A. H. Y. Tong *et al.*, "Global Mapping of the Yeast Genetic Interaction Network," Science **303**, 808–813 (2004).

[20] E. B. Hook, ed., *Prematurity in Scientific Discovery: On Resistance and Neglect*. University of California Press, 2002.

[21] A. Koestler, *The Sleepwalkers*. Macmillan, New York, 1st ed., 1968.

[22] Sir I. Newton (translated by Andrew Motte and revised by Florian Cajori), *Mathematical Principles of Natural Philosophy*. William Benton, Chicago, 1953.

[23] A. Bensimon, A. Simon, A. Chiffaudel, V. Croqquette, F. Heslot, and D. Bensimon, "Alignment and sensitive detection of DNA by a moving interface," Science **265**, 2096–2098 (1994).

[24] J. J. Blow, P. J. Gillespie, D. Francis, and D. A. Jackson, "Replication origins in *Xenopus* egg extracts are 5-15 kilobases apart and are activated in clusters that fire at different times," J. Cell Biol. **152**, 15–25 (2001).

[25] P. Norio and C. L. Schildkraut, "Visualization of DNA replication on individual *Epstein-Barr* virus episomes," Science **294**, 2361–2364 (2001).

[26] W. Humphrey, A. Dalke, and K. Schulten, "Visual Molecular Dynamics," Journal of Molecular Graphics **14**, 33–38 (1996). http://www.ks.uiuc.edu/Research/vmd/.

[27] J. D. Watson and F. H. C. Crick, "Genetic implications of the structure of deoxyribonucleic acid," Nature **171**, 964–967 (1953).

[28] M. Meselson and F. W. Stahl, "The Replication of DNA in *Escherichia Coli*," Proc. Nat. Acad. Sci. USA **44**, 671–682 (1958).

[29] A. Kornberg, I. R. Lehman, M. J. Bessman, and E. S. Simms, "Enzymic synthesis of DNA," Biochim. Biophys. Acta. **21**, 197–198 (1956).

[30] A. Kornberg and T. Baker, *DNA replication.* W. H. Freeman & Co, New York, 2nd ed., 1992.

[31] J. SantaLucia Jr., H. T. Allawi, and P. A. Seneviratne, "Improved nearest-neighbor parameters for predicting DNA duplex stability," Biochemistry **35**, 3555–3562 (1996).

[32] B. Alberts, D. Bray, J. Lewis, M. Raff, J. H. Miller, R. C. Lewontin, *Molecular Biology of the Cell.* Garland Publishing Inc., New York, 3rd. ed., 1994.

[33] H. J. Kriegstein and D. S. Hogness, "Mechanism of DNA replication in *Drosophila* Chromosomes: Structure of Replication Forks and Evidence for Bidirectionality," Proc. Nat. Acad. Sci. USA **71**, 135–139 (1974).

[34] J. J. Blow, "Control of chromosomal DNA replication in the early *Xenopus* embryo," EMBO J. **20**, 3293–3297 (2001).

[35] O. Hyrien, K. Marheineke, and A. Goldar, "Paradoxes of eukaryotic DNA replication: MCM proteins and the random completion problem," BioEssays **25**, 116–125 (2003).

[36] O. Hyrien and M. Mechali, "Chromosomal replication initiates and terminates at random sequences but at regular intervals in the ribosomal DNA of *Xenopus* early embryos.," EMBO J. **12**, 4511–4520 (1993).

[37] J. W. Raff and D. M. Glover, "Nuclear and cytoplasmic mitotic cycles continue in *Drosophila* embryos in which DNA synthesis is inhibited with aphidicolin," J. Cell Biol. **48**, 399–407 (1988).

[38] P. R. Cook, *Principles of Nuclear Structure and Function.* Wiley-Liss, New York, 2001.

[39] A. N. Kolmogorov, "On the statistical theory of crystallization in metals," Izv. Akad. Nauk SSSR, Ser. Fiz. [Bull. Acad. Sci. USSR, Phys. Ser.] **1**, 355–359 (1937).

[40] W. A. Johnson and P. A. Mehl, "Reaction kinetics in processes of nucleation and growth," Trans. AIMME **135**, 416–442 (1939).

[41] M. Avrami, "Kinetics of phase change. I. General theory," J. Chem. Phys. **7**, 1103–1112 (1939).

[42] M. Avrami, "Kinetics of phase change. II. Transformation-time relations for random distribution of nuclei," J. Chem. Phys. **8**, 212–224 (1940).

[43] M. Avrami, "Kinetics of phase change. III. Granulation, phase change, and microstructure," J. Chem. Phys. **9**, 177–184 (1941).

[44] J. Herrick, P. Stanislawski, O. Hyrien, and A. Bensimon, "Replication fork density increases during DNA synthesis in *X. laevis* egg extracts," J. Mol. Biol. **300**, 1133–1142 (2000).

[45] J. W. Christian, *The Theory of Phase Transformations in Metals and Alloys, Part I*, Volume 1. Pergamon Press, New York, 3rd ed., 2002.

[46] C. P. Yang and J. F. Nagle, "Phase transformations in lipids follow classical kinetics with small fractional dimensionalities," Phys. Rev. A **37**, 3993–4000 (1988).

[47] T. Huang, T. Tsuji, M. R. Kamal, and A. D. Rey, "Domain-spatial correlation functions and scaling relations of nucleation and growth in polymer films," Phys. Rev. E **58**, 789–792 (1998).

[48] M. Fanfoni and M. Tomellini, "The Johnson-Mehl-Avrami-Kolmogorov model: A brief review," Nuovo Cimento D **20**, 1171–1182 (1998).

[49] G. Korniss and T. Caraco *et al.* preprint (2004).

[50] B. Kämpfer, "Cosmic phase transitions," Ann. Phys. (Leibzig) **9**, 1–33 (2000).

[51] J. W. Evans, "Random and cooperative sequential adsorption," Rev. Mod. Phys. **65** (**4**), 1281–1329 (1993).

[52] R. A. Ramos, P. A. Rikvold, and M. A. Novotny, "Test of the Kolmogorov-Johnson-Mehl-Avrami picture of metastable decay in a model with microscopic dynamics," Phys. Rev. B **59**, 9053–9069 (1999).

[53] H. Orihara and Y. Ishibashi, "A statistical theory of nucleation and growth in finite systems," J. Phys. Soc. Jap. **61** (**6**), 1919–1925 (1992).

[54] J. W. Cahn, "The time cone method for nucleation and growth kinetics on a finite domain," Mater. Res. Soc. Symp. Proc. **398**, 425–438 (1996).

[55] J. W. Cahn, "Johnson-Mehl-Avrami kinetics on a finite growing domain with time and position dependent nucleation and growth rates," Trans. Indian Inst. Met. **50**, 573–580 (1997).

[56] A. Rényi, "On a one-dimensional random space filling problem," Publ. Math. Inst. Hung. Acad. Sci. **3**, 109–127 (1958).

[57] B. Derrida, C. Godrèche, and I. Tekutieli, "Stable distributions of growing and coalescing droplets," Europhys. Lett. **12** (**5**), 385–390 (1990).

[58] M. L. DePamphilis, ed., *DNA Replication in Eukaryotic Cells.* Cold Spring Harbor Laboratory Press, Cold Spring Harbor, New York, 1996.

[59] J. Herrick, S. Jun, J. Bechhoefer, and A. Bensimon, "Kinetic Model of DNA replication in eukaryotic organisms," J. Mol. Biol. **320**, 741–750 (2002).

[60] J. A. Huberman and A. D. Riggs, "Autoradiography of chromosomal DNA fibers from Chinese hamster cells," Proc. Natl. Acad. Sci. USA **55**, 599–606 (1966).

[61] B. R. Jasny and I. Tamm, "Temporal organization of replication in DNA fibers of mammalian cells," J. Cell Biol. **81**, 692–697 (1979).

[62] K. Sekimoto, "Kinetics of magnetization switching in a 1-D system – size distribution of unswitched domains," Physica **125A**, 261–269 (1984).

[63] K. Sekimoto, "Kinetics of magnetization switching in a 1-D system II – Long time behavior of switched domains," Physica **128A**, 132–149 (1984).

[64] K. Sekimoto, "Evolution of the domain structure during the nucleation-and-growth process with non-conserved order parameter," Int. J. Mod. Phys. B **5**, 1843–1869 (1991).

[65] E. Ben-Naim and P. L. Krapivsky, "Nucleation and growth in one dimension," Phys. Rev. E **54**, 3562–3568 (1996).

[66] J. Krug, P. Meakin, and T. Halpin-Healy, "Amplitude universality for driven interfaces and directed polymers in random media," Phys. Rev. A **45**, 638–653 (1992).

[67] E. Ben-Naim, A. R. Bishop, I. Daruka, and P. L. Krapivsky, "Mean-field theory of polynuclear surface growth," J. Phys. A: Math. Gen. **31**, 5001–5012 (1998).

[68] M. L. Boas, *Mathematical Methods in the Physical Sciences*. John Wiley & Sons, New York, 2nd ed., 1983.

[69] G. Arfken and H. Weber, *Mathematical Methods for Physicists*. Academic Press, San Diego, 4th ed., 1995.

[70] W. H. Press, S. A. Teukolsky, W. T. Vetterling, and B. P. Flannery, *Numerical Recipes in C*. Cambridge, New York, 1st ed., 1992.

[71] S. Jun, J. Herrick, A. Bensimon, and J. Bechhoefer, "Persistence Length of Chromatin Determines Origin Spacing in Xenopus Early-Embryo DNA Replication: Quantitative Comparisons between Theory and Experiment.," Cell Cycle **3** (**2**), 223–229 (2004).

[72] M. Tomellini, M. Fanfoni, and M. Volpe, "Spatially correlated nuclei: How the Johnson-Mehl-Avrami-Kolmogorov formula is modified in the case of simultaneous nucleation," Phys. Rev. B **62**, 11300–11303 (2000).

[73] Igor Pro. WaveMetrics, Inc. P. O. Box 2088, Lake Oswego, Oregon 97035, USA. http://www.wavemetrics.com.

[74] C. DeW. van Siclen, "Random nucleation and growth kinetics," Phys. Rev. B **54**, 11845–11848 (1996).

[75] M. Tomellini and M. Fanfoni, "Why phantom nuclei must be considered in the Johnson-Mehl-Avrami-Kolmogoroff kinetics," Phys. Rev. B **55**, 14071–14073 (1997).

[76] M. Fanfoni and M.Tomellini, "Beyond the Kolmogorov Johnson Mehl Avrami kinetics: inclusion of the spatial correlation," Eur. Phys. J. B **34**, 331–341 (2003).

[77] S. Jun and J. Bechhoefer, "Nucleation and growth in one dimension, part I: The generalized Kolmogorov-Johnson-Mehl-Avrami model," preprint (2004).

[78] I. Lucas, M. Chevrier-Miller, J. M. Sogo, O. Hyrien, "Mechanisms ensuring rapid and complete DNA replication despite random initiation in *Xenopus* early embryos," J. Mol. Biol. **296**, 769–786 (2000).

[79] A. B. Blumenthal, H. J. Kriegstein, and D. S. Hogness, "The units of DNA replication in Drosophila melanogaster chromosomes," Cold Spring Harbor Symp. Quant. Biol. **38**, 205–223 (1974).

[80] D. S. Sivia, *Data Analysis: a Bayesian Tutorial.* Oxford, New York, 1996.

[81] S. Jun and J. Bechhoefer, "Nucleation and growth in one dimension, part II: Application to DNA replication kinetics," preprint (2004).

[82] J. Walter and J. W. Newport, "Regulation of replicon size in *Xenopus* egg extracts," Science **275**, 993–995 (1997).

[83] D. Coverly and R. A. Laskey, "Regulation of eukaryotic DNA replication," Ann. Rev. Biochem. **63**, 745–776 (1994).

[84] J. J. Blow and J. P. Chong, eds., *DNA Replication in Eukaryotic Cells.* Cold Spring Harbor Laboratory Press, Cold Spring Harbor, 1996.

[85] T. Shinomiya and S. Ina, "Analysis of chromosomal replicons in early embryos of Drosophila melanogaster by two-dimensional gel electrophoresis," Nucleic Acids Research **19**, 3935–3941 (1991).

[86] B. J. Brewer and W. L. Fangman, "Initiation at Closely Spaced Replication Origins in a Yeast Chromosome," Science **262**, 1728–1731 (1993).

[87] M. Gomez and F. Antequera, "Organization of DNA replication origins in the fission yeast genome," EMBO J. **18**, 5683–5690 (1999).

[88] S. Coterill, ed., *Eukaryotic DNA Replication: A Practical Approach.* Oxford, 1999.

[89] J. Cairns, "The Chromosome of *E. coli*," Cold Spring Harbor Symposia on Quantitative Biology **28**, 43–46 (1963).

[90] A. J. Solari, "Structure of the chromatin in sea urchin sperm," Proc. Nat. Acad. Sci. **53**, 503–511 (1965).

[91] J. A. Huberman and A. D. Riggs, "On the mechanism of DNA replication in mammalian chromosomes," J. Mol. Biol. **75**, 327–341 (1968).

[92] B. J. Trask, "Fluorescence in situ hybridization: applications in cytogenetics and gene mapping," Trends Genet. **7**, 149–154 (1991).

[93] G. J. van Ommen, M. H. Breuning, and A. K. Raap, "FISH in genome research and molecular diagnostics," Curr. Opin. Genet. Dev. **5(3)**, 304–308 (1995).

[94] I. Parra and B. Windle, "High resolution visual mapping of stretched DNA by fluorescent hybridization," Nat. Genet. **5**, 17–21 (1993).

[95] D. A. Jackson and A. Pombo, "Replication Clusters Are Stable Units of Chromosome Structure: Evidence That Nuclear Organization Contributes to the Efficient Activation and Propagation of S Phase in Human Cells," J. Cell Biol. **140**, 1285–1295 (1998).

[96] K. Friedman and B. Brewer, "Analysis of replication intermediates by two-dimensional agarose gel electrophoresis," Meth. Enzymol. **262**, 613–627 (1995).

[97] J. A. Huberman, "Mapping replication origins, pause sites, and termini by neutral/alkaline two-dimensional gel electrophoresis," Methods: A Companion to Methods in Enzymology **13**, 247–257 (1997).

[98] A. B. Khodursky, B. J. Peter, M. B. Schmid, J. DeRisi, D. Botstein, P. O. Brown, and N. R. Cozzarelli, "Analysis of topoisomerase function in bacterial replication fork movement: Use of DNA microarrays," Proc. Nat. Acad. Sci. **97**, 9419–9424 (2000).

[99] M. K. Raghuraman, E. A. Winzeler, D. Collingwood, S. Hunt, L. Wodlicka, A. Conway, D. J. Lockhart, R. W. Davis, B. J. Brewer, and W. L. Fangman, "Replication dynamics of the yeast genome," Science **294**, 115–121 (2001).

[100] J. J. Wyrick, J. G. Aparicio, T. Chen, J. D. Barnett, E. G. Jennings, R. A. Young, S. P. Bell, and O. M. Aparicio, "Genome-wide distribution of ORC and MCM proteins in *S. cerevisiae*: high-resolution mapping of replication origins," Science **294**, 2357–2360 (2001).

[101] K. L. Friedman, B. J. Brewer, and W. L. Fangman, "Replication profile of *Saccharomyces cerevisiae* chromosome VI," Genes to Cells **2**, 667–678 (1997).

[102] M. Yamashita, Y. Hori, T. Shinomiya, C. Obuse, T. Tsurimoto, H. Yoshikawa, and K. Shirahige, "The efficiency and timing of initiation of replication of multiple replicons of *Saccharomyces cerevisiae* chromosome VI," Genes to Cells **2**, 655–665 (1997).

[103] G. V. Shivashankar, M. Feingold, O. Krichevsky, and A. Libchaber, "RecA polymerization on double-stranded DNA by using single-molecule manipulation: The role of ATP hydrolysis," Proc. Natl. Acad. Sci. USA **96**, 7916–7921 (1999).

[104] R. Berezney, D. D. Dubey, and J. A. Huberman, "Heterogeneity of eukaryotic replicons, replicon clusters, and replication foci," Chromosoma **108**, 471–484 (2000).

[105] X. Michalet, R. Ekong, F. Fougerousse, S. Rousseaux, C. Shurra, N. Hornigold, M. van Slegtenhorst, J. Wolfe, S. Povey, J. S. Beckmann, and A. Bensimon, "Dynamic molecular combing: stretching the whole human genome for high-resolution studies," Science **277**, 1518–1523 (1997).

[106] J. Herrick, X. Michalet, C. Conti, C. Shurra, and A. Bensimon, "Quantifying single gene copy number by measuring fluorescent probe lengths on combed genomic DNA," Proc. Natl. Acad. Sci. USA **97**, 222–227 (2000).

[107] J. J. Blow and R. A. Laskey, "Initiation of DNA replication in nuclei and purified DNA by a cell-free extract of *Xenopus* eggs," Cell **47**, 577–587 (1986).

[108] J. J. Blow and J. V. Watson, "Nuclei act as independent and integrated units of replication in a *Xenopus* cell-free DNA replication system," EMBO J. **6**, 1997–2002 (1987).

[109] J. R. Wu, G. Yu, and D. M. Gilbert, "Origin-specific initiation of mammalian nuclear DNA replication in a *Xenopus* cell-free system," Methods **13**, 313–324 (1997).

[110] I. Simon, T. Tenzen, B. E. Reubinoff, D. Hillman, J. R. McCarrey, and H. Cedar, "Asynchronous replication of imprinted genes is established in the gametes and maintained during development," Nature **401**, 929–932 (1999).

[111] P. Pasero and E. Schwob, "Think global, act local – how to regulate S phase from individual replication origins," Current Opinion in Genetics and Development **10**, 178–186 (2000).

[112] A. D. Mills, J. J. Blow, J. G. White, W. B. Amos, D. Wilcock, and R. A. Laskey, "Replication occurs at discrete foci spaced throughout nuclei replicating in vitro," J. Cell Sci. **94**, 471–477 (1989).

[113] H. M. Mahbubani, T. Paull, J. K. Elder, and J. J. Blow, "DNA replication initiates at multiple sites on plasmid DNA in *Xenopus* egg extracts," Nucl. Acids Res. **20**, 1457–1462 (1992).

[114] Z. H. Lu, D. B. Sittman, P. Romanowski, and G. H. Leno, "Histone H1 reduces the frequency of initiation in *Xenopus* egg extract by limiting the assembly of prereplication complexes on sperm chromatin," Mol. Biol. of the Cell **9**, 1163–1176 (1998).

[115] M. Buongiorno-Nardelli, G. Michelli, M. T. Carri, and M. Marilley, "A relationship between replicon size and supercoiled loop domains in the eukaryotic genome," Nature **298**, 100–102 (1982).

[116] R. A. Laskey, "Chromosome replication in early development of *Xenopus laevis*," J. Embryology & Experimental Morphology **89**, Suppl. 285–296 (1985).

[117] D. M. Gilbert, "Making sense of eukaryotic DNA replication origins," Science **294**, 96–100 (2001).

[118] A. Rowles, J. P. Chong, L. Brown, M. Howell, G. I. Evan, and J. J. Blow, "Interaction between the origin recognition complex and the replication licensing system in *Xenopus*," Cell **87**, 287–296 (1996).

[119] K. Marheineke and O. Hyrien, "Aphidicolin triggers a block to replication origin firing in *Xenopus* egg extracts.," J. Biol. Chem. **276**, 17092–17100 (2001).

[120] P. R. Cook, "The organization of replication and transcription," Science **284**, 1790–1795 (1999).

[121] M. Méchali, "DNA replication origins: from sequence specificity to epigenetics," Nat. Rev. Genet. **2**, 640–645 (2001).

[122] H. Yamakawa, *Helical wormlike chains in polymer solutions*. Springer, Berlin, 1997.

[123] J. Shimada and H. Yamakawa, "Ring-closure probabilities for twisted wormlike chains. Application to DNA," Macromolecules **17**, 689–698 (1984).

[124] J. Dekker, K. Rippe, M. Dekker, and N. Kleckner, "Capturing chromosome conformation," Science **295**, 1306–1311 (2002).

[125] Y. Cui and C. Bustamante, "Pulling a single chromatin fiber reveals the forces that maintain its higher-order structure," Proc. Natl. Acad. Sci. **97**, 127–132 (2000).

[126] K. Rippe, "Making contacts on a nucleic acid polymer," Trends. Biochem. Sci. **26**, 733–740 (2001).

[127] M. C. Edwards, A. V. Tutter, C. Cvetic, C. H. Gilbert, T. A. Prokhorova, J. C. Walter, "MCM2-7 complexes bind chromatin in a distributed pattern surrounding the origin recognition complex in *Xenopus* egg extracts," J. Biol. Chem. **277**, 33049–33057 (2002).

[128] K. J. Harvey and J. Newport, "CpG methylation of DNA restricts prereplication complex assembly in *Xenopus* egg extracts," Mol. Cell. Biol. **23**, 6769–6779 (2003).

[129] R. Schleif, "DNA looping," Annu. Rev. Biochem. **61**, 199–223 (1992).

[130] K. Rippe, P. H. von Hippel, J. Langowski, "Action at a distance: DNA-looping and initiation of transcription," TIBS **20**, 500–506 (1995).

[131] P. J. Horn and C. L. Peterson, "Molecular biology. Chromatin higher order folding–wrapping up transcription," Science **297**, 1824–1827 (2002).

[132] P. Heun, T. Laroche, K. Shimada, P. Furrer, S. M. Gasser, "Chromosome Dynamics in the Yeast Interphase Nucleus," Science **294**, 2181–2186 (2001).

[133] D. Thirumalai, "Time scale for the formation of the most probable tertiary contacts in proteins with applications to cytochrome *c*," J. Phys. Chem. B **103**, 608–610 (1999).

[134] Z. Guo and D. Thirumalai, "Kinetics of protein folding: Nucleation mechanism, time scales, and pathways," Biopolymers **36**, 83–102 (1995).

[135] N. L. Goddard, G. Bonnet, O. Krichevsky, and A. Libchaber, "Sequence Dependent Rigidity of Single Stranded DNA," Phys. Rev. Lett. **85**, 2400–2403 (2000).

[136] P. G. de Gennes, *Scaling Concepts in Polymer Physics*. Cornell University Press, Ithaca, 1979.

[137] M. Doi and S. F. Edwards, *The Theory of Polymer Dynamics*. Oxford Science Publications, Oxford, UK, 1986.

[138] L. D. Landau and E. M. Lifshitz, *Theory of Elasticity*. Butterworth-Heinemann Ltd, Oxford, UK, 3rd ed., 1986.

[139] R. Everaers, "Computer simulations and scaling concepts in polymer physics," Habilitation thesis, Ch. 3 (2002).

[140] D. Thirumalai D. and B. Y. Ha, *Theoretical and Mathematical Models in Polymer Research*. Edited by A. Grosberg. Academic Press, San Diego, 1998.

[141] R. G. Winkler, "Deformation of semiflexible chains," J. Chem. Phys. **118**, 2919–2928 (2003).

[142] U. Seifert, W. Wintz, and P. Nelson, "Straightening of Thermal Fluctuations in Semiflexible Polymers by Applied Tension," Phys. Rev. Lett. **77**, 5389–5392 (1996).

[143] L. Harnau, R. G. Winkler, and P. Reineker, "On the dynamics of polymer melts: Contribution of Rouse and bending modes," Europhys. Lett. **45**, 488–494 (1999).

[144] N. K. Lee and D. Thirumalai, "Pulling-speed-dependent force-extension profiles for semiflexible chains," Biophys. J. **86**, 2461–2649 (2004).

[145] A. Szabo, K. Schulten, and Z. Schulten, "First passage time approach to diffusion controlled reactions," J. Chem. Phys. **72**, 4350–4357 (1980).

[146] G. Wilemski and M. Fixman, "Diffusion-controlled intrachain reactions of polymers. I Theory," J. Chem. Phys. **60**, 866–877 (1974).

[147] G. Wilemski and M. Fixman, "Diffusion-controlled intrachain reactions of polymers. II Results for a pair of terminal reactive groups," J. Chem. Phys. **60**, 878–890 (1974).

[148] M. Doi, "Diffusion-controlled reaction of polymers," Chem. Phys. **9**, 455–466 (1975).

[149] R. W. Pastor, R. Zwanzig, and A. Szabo, "Diffusion limited first contact of the ends of a polymer: Comparison of theory with simulation," J. Chem. Phys. **105**, 3878–3882 (1996).

[150] J. J. Portman,, "Non-Gaussian dynamics from a simulation of a short peptide: Loop closure rates and effective diffusion coefficients," J. Chem. Phys. **118**, 2381–2391 (2003).

[151] H. Schiessel, J. Widom, R. F. Bruinsma, and W. M. Gelbart,, "Polymer Reptation and Nucleosome Repositioning," Phys. Rev. Lett. **86**, 4414–4417 (2001).

[152] I. M. Kulić. and H. Schiessel, "Nucleosome Repositioning via Loop Formation," Biophys. J. **84**, 3197–3211 (2003).

[153] A. A. Podtelezhnikov and A. V. Vologodskii, "Dynamics of Small Loops in DNA Molecules," Macromolecules **33**, 2767–2771 (2000).

[154] A. Dua and B. Cherayil, "The dynamics of chain closure in semiflexible polymers," J. Chem. Phys. **116**, 399–409 (2002).

[155] S. Jun, J. Bechhoefer, B.-Y. Ha, "Diffusion-limited loop formation of semiflexible polymers: Kramers theory and the intertwined time scales of chain relaxation and closing," Europhys. Lett. **64** (**3**), 420–426 (2003).

[156] J. Z. Y. Chen, H. K. Tsao, and Y.-J. Sheng, "First-passage time of cyclization dynamics of a wormlike polymer," Europhys. Lett. **65** (**3**), 407–413 (2004).

[157] H. A. Kramers,, "Brownian motion in a field of force and the diffusion model of chemical reactions," Physica (Utrecht) **7**, 284–304 (1940).

[158] P. Hänggi, P. Talkner, and M. Borkovec, "Reaction-rate theory: fifty years after Kramers," Rev. Mod. Phys. **62**, 251–341 (1990).

[159] O. Kratky and G. Porod, "Röntgenuntersuchung gelöster Fadenmoleküle," Rec. Trav. Chim. **68**, 1106–1113 (1949).

[160] N. Saito, K. Takahashi, Y. Yunoki, "The statistical mechanical theory of stiff chains," J. Phys. Soc. Jpn. **22**, 219–226 (1967).

[161] J. F. Marko and E. D. Siggia, "Statistical mechanics of supercoiled DNA," Phys. Rev. E **52**, 2912–2938 (1995).

[162] H. Yamakawa and W. H. Stockmayer, "Statistical mechanics of wormlike chains II," J. Chem. Phys. **57**, 2843–2856 (1972).

[163] L. Ringrose, S. Chabanis, P. Angrand, C. Woodroofe, A. F. Stewart, "Quantitative comparison of DNA looping in vitro and in vivo: chromatin increases effective DNA flexibility at short distances," EMBO J. **18**, 6630–6641 (1999).

[164] W. F. J. Wilhelm and E. Frey, "Radial Distribution Function of Semiflexible Polymers," Phys. Rev. Lett. **77**, 2581–2584 (1996).

[165] L. Harnau, R. G. Winkler, and P. Reineker, "Influence of stiffness on the dynamics of macromolecules in a melt," J. Chem. Phys. **106**, 2469–2476 (1997).

[166] R. Granek, "From semi-flexible polymers to membranes: anomalous diffusion and reptation," J. Phys. II France **7**, 1761–1788 (1997).

[167] J.-L. Barrat and J.-P. Hansen, *Basic Concepts for Simple and Complex Liquids*. Cambridge University Press, Cambridge, UK, 2003.

[168] H. C. Berg, *Random Walks in Biology*. Princeton University Press, Princeton, NJ, 1983.

[169] A. Balaeff, C. R. Koudella, L. Mahadevan, K. Schulten, "Modelling DNA loops using continuum and statistical mechanics," Proc. R. Soc. Lond. A *in press* (2004).

[170] P. G. de Gennes, "Kinetics of diffusion-controlled processes in dense polymer systems. I. Nonentangled regimes," J. Chem. Phys. **76**, 3316–3214 (1982).

[171] A. A. Podtelezhnikov and A. V. Vologodskii, "Simulations of Polymer Cyclization by Brownian Dynamics," Macromolecules **30**, 6668–6673 (1997).

[172] Y. J. Sheng, J. Z. Y. Chen, and H.-K. Tsao, "Open-to-Closed Transition of a Hard-Sphere Chain with Attractive Ends," Macromolecules **35**, 9624–9627 (2002).

[173] M. Wortis, Lecture notes on the Kramers escape problem, Simon Fraser University (2002).

[174] C. W. Gardiner, *Handbook of Stochastic Methods: for Physics, Chemistry, and the Natural Sciences*. Springer, Berlin, 2nd ed., 1985.

[175] C. R. Koudella, private communication.

[176] B.-Y. Ha, private communication.

[177] O. G. Berg and P. H. von Hippel, "Diffusion-controlled macromolecular interactions," Ann. Rev. Biophys. Biophys. Chem. **14**, 131–160 (1985).